

Superconducting single-photon and photon-number-resolving detectors

Citation for published version (APA):

Jahanmirinejad, S. (2012). *Superconducting single-photon and photon-number-resolving detectors*. [Phd Thesis 1 (Research TU/e / Graduation TU/e), Applied Physics and Science Education]. Technische Universiteit Eindhoven. <https://doi.org/10.6100/IR740220>

DOI:

[10.6100/IR740220](https://doi.org/10.6100/IR740220)

Document status and date:

Published: 01/01/2012

Document Version:

Publisher's PDF, also known as Version of Record (includes final page, issue and volume numbers)

Please check the document version of this publication:

- A submitted manuscript is the version of the article upon submission and before peer-review. There can be important differences between the submitted version and the official published version of record. People interested in the research are advised to contact the author for the final version of the publication, or visit the DOI to the publisher's website.
- The final author version and the galley proof are versions of the publication after peer review.
- The final published version features the final layout of the paper including the volume, issue and page numbers.

[Link to publication](#)

General rights

Copyright and moral rights for the publications made accessible in the public portal are retained by the authors and/or other copyright owners and it is a condition of accessing publications that users recognise and abide by the legal requirements associated with these rights.

- Users may download and print one copy of any publication from the public portal for the purpose of private study or research.
- You may not further distribute the material or use it for any profit-making activity or commercial gain
- You may freely distribute the URL identifying the publication in the public portal.

If the publication is distributed under the terms of Article 25fa of the Dutch Copyright Act, indicated by the "Taverne" license above, please follow below link for the End User Agreement:

www.tue.nl/taverne

Take down policy

If you believe that this document breaches copyright please contact us at:

openaccess@tue.nl

providing details and we will investigate your claim.

Superconducting Single-Photon and Photon-Number-Resolving Detectors

PROEFSCHRIFT

ter verkrijging van de graad van doctor aan de
Technische Universiteit Eindhoven, op gezag van de
rector magnificus, prof.dr.ir. C.J. van Duijn, voor een
commissie aangewezen door het College voor
Promoties in het openbaar te verdedigen
op woensdag 12 december 2012 om 16.00 uur

door

Saeedeh Jahanmirinejad

geboren te Shiraz, Iran

Dit proefschrift is goedgekeurd door de promotor:
prof.dr. A. Fiore

A catalogue record is available from the Eindhoven
University of Technology Library
Superconducting single-photon and photon-number
resolving detectors, by S. jahanmirinejad
ISBN: 978-90-386-3305-3

The work described in this thesis has been carried out in
the group of Photonics and Semiconductor Nanophysics,
at the department of Applied Physics of Eindhoven
University of Technology, The Netherlands.

Printed by Ipskamp Drukkers.

Contents

Abstract	1
1. Introduction	3
1.1. Single-Photon Avalanche Diodes (SPAD's)	3
1.2 Superconducting Single Photo Detectors	5
1.2.1 Transition Edge Sensor (TES)	5
1.2.2 Nanowire Superconducting Single Photon Detectors	7
1.3 Description of the Performance Properties of SPDs	9
1.3.1 Quantum Efficiency (QE)	9
1.3.2 Spectral response	11
1.3.3 Dark Count Rate (DCR)	12
1.3.4 Dead time	13
1.3.5 Timing resolution	14
1.3.6 Photon number resolving (PNR) capability	15
1.4 Comparison of Different SPD Technologies	16
1.5 Goal of This Thesis	17
1.6 Outline of the Thesis	18
References	18
2. Methods	23
2.1 Cryogenic Setups	23
2.1.1 Micro-manipulated probe station	23
2.1.2 Cryogenic dipstick	26
2.1.3 Closed-cycle cryocooler	27
2.2 Experimental setup	28
2.3 Electro-Thermal Model	32
2.3.1 Thermal model	33
2.3.2 Electrical model	35
2.3.3 Results	36
References	39
3. Integration of SSPDs with optical microcavities	41
3.1 Optical Absorption Limit	42
3.2 Optical Microcavity	43
3.3 SSPD Integrated with an Optical Microcavity	45
3.4 Fabrication of Microcavity Structure	46
3.5 Experimental Results	47
3.6 Conclusion	50
References	51
4. Parallel Nanowire Detectors	53
4.1. Structure and Working Principle of PNDs	54
4.2. Electro-Thermal Simulation	57

4.3. Current Redistribution Problem	58
4.4. Latching Problem	62
4.5. Solutions for the Latching Problem	63
4.6. Conclusion	64
References	64
5. Series Nanowire Detectors	67
5.1. Theory of SND.....	68
5.1.1. SND structure and operation principle	68
5.1.2. SND electro-thermal simulation	69
5.1.3. Voltage transients	71
5.1.4 Dynamic characteristics of the SND	75
5.1.5. SND response with realistic high-impedance readout	76
5.1.6. Limitations of the fidelity in an SND	77
5.1.7 Simulation of the fabricated 4-SND	79
5.2. SND Realization	79
5.2.1. Fabrication.....	80
5.2.2. Electrical characterization	81
5.2.3. Optical characterization.....	81
5.3. High Impedance Load.....	87
5.4. Conclusion	88
References.....	88
6. Conclusion	91
Reference	93
Summary	95
Acknowledgement	97
List of publications	99
Curriculum vitae	101

Abstract

Detecting light of low intensity is a key requirement in many fields of scientific endeavor, including but not limited to quantum information science, astronomy and optical spectroscopy. In the past decade the progress in the technology of superconducting film has allowed the realization of a new type of detector based on ultrathin (4–5 nm) and narrow (<100nm) superconducting nanowires. Such nanowire detectors are sensitive to the energy of single photons in a broad spectral bandwidth from the visible to the mid-infrared range, with fast response time, low noise and excellent timing resolution. A detector of this type, which is called nanowire superconducting single photon detector (SSPD), can outperform conventional semiconductor-based single-photon detection technologies in the aforementioned aspects. The detector is operated at a temperature well below the critical temperature of the superconducting nanowire and is biased with a current sufficiently close to its critical current. In this situation, absorption of a photon leads to a temporary suppression of superconductivity and formation of a resistive region across the nanowire, which produces a measurable voltage pulse. The goal of this thesis has been to improve the understanding, the performance and the functionality of nanowire SSPDs.

Having a thickness in the range of few nanometers, a SSPD is not very likely to absorb the incident light, therefore has a limited efficiency. In this thesis we introduce a technique to enhance the efficiency of SSPD by boosting the probability of light absorption. This is achieved by integrating the device with an optical microcavity designed for the telecom wavelength of 1300 nm.

The traditional detector structure and readout electronics does not allow a SSPD to distinguish between one or more photons that impinge on it at the same time. In this thesis, we explore ways to achieve photon-number-resolving (PNR) functionality with SSPDs. We utilize spatial multiplexing techniques in which the light is distributed over an array of nanowires which are electrically connected, so that the output signal is proportional to the number of photons in the input optical pulse. We first investigate the parallel connection of nanowires which was previously demonstrated, and by using an electrothermal model we evidence the limitations related to the current redistribution among the wires. In order to circumvent these restrictions, we propose a dual approach based on the series connection of nanowires, called series nanowire detector (SND). This approach is promising in terms of scalability to large elements. We theoretically simulate and experimentally demonstrate this new PNR detector.

These results show that the integration of SNDs with optical microcavities will provide efficient and fast photon number resolving detectors which will fill the existing gap between linear optical detection and single photon detection regimes, particularly in telecom wavelength ranges.

CHAPTER 1

Introduction

Optical detection involves the conversion of optical energy in the form of photons (the single quanta of electromagnetic radiation) into an electrical signal in the form of electrons to be processed by the conventional electronics. Single-photon detection provides the utmost level of sensitivity in optical measurements. Over the past years, there has been growing interest in single-photon detectors (SPDs) as the enabling technology for many applications. In many cases, these applications involve physical phenomena in which a very small number of photons—often just one—are available for detection, such as in single molecule spectroscopy [1], fluorescence analysis [2], ultra-low-light-level imaging [3], light detection and ranging (LIDAR) [4] and optical-time-domain-reflectometry (OTDR) [5]. Other emerging applications employ the quantum properties of a single photon. High-performance photon counters are indispensable constituents in the progressing field of quantum information processing and quantum communication [6], [7]. Finally, single photon detection is widely used in the astronomical research to observe the dark corners of the universe [8]. Spurred by the vast range of applications, there has been an ongoing effort and extensive research on SPDs. In the following sections, three promising approaches of optical detection with single photon sensitivity are introduced. Among these approaches, the most recently emerged nanowire superconducting single photon detector (SSPD) has shown promise of favorable development of high performance single-photon detection. The most important figure-of-merit parameters of a SPD are discussed with the emphasis on the operation of SSPDs. Finally, the state-of-the-art values regarding the different approaches are compared to reveal the motivation for this research.

1.1. Single-Photon Avalanche Diodes (SPAD's)

Avalanche photodiodes (APD's) are essentially p-i-n junctions that are reverse biased slightly below the breakdown voltage. In APDs, the incident light generates electron-hole pairs in the depletion region, which are then accelerated under the effect of the electric field and produce secondary carriers by impact ionization, resulting in carrier multiplication and increased photocurrent. In APDs, the increase of the diode current is proportional to the incident light

intensity. This is known as “linear” operation regime. APDs working in linear mode are usually the detectors of choice for many applications in optical communications systems that require high sensitivity detectors, mostly owing to their internal gain process. When the reverse voltage applied to an APD is set higher than the breakdown voltage, the first absorbed photon is capable of triggering a diverging avalanche multiplication of carriers by impact ionization, resulting in a macroscopic current with a fast rise-time pulse that can be detected. This operating method is called Geiger mode, which grants APDs the extreme sensitivity to single-photon level, as they are called single-photon avalanche diodes (SPADs). The avalanche must then be quenched by a circuit connected to the diode, which reduces the voltage bias below the breakdown voltage in order to make the detection of a subsequent photon possible. The left and right sides of Fig. 1.1 show schematically the operation principle of an APD in the linear and Geiger mode, respectively [9].

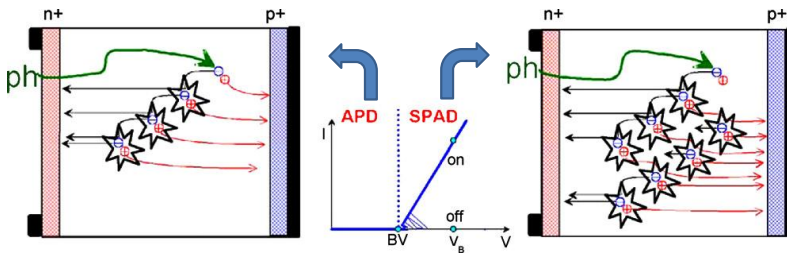


Fig. 1.1 (Left side) APDs are biased just below breakdown voltage in order to work in a non-diverging multiplication process, i.e. linear multiplication regime. (Right side) SPADs are biased well above the breakdown voltage where one photo-generated carrier can trigger a diverging avalanche multiplication process, leading to a macroscopic detectable output current. The figure is from [9].

Most SPADs do not resolve the number of photons, i.e. provide an output signal independent of the number of photons that initiated the avalanche. The number of photons which triggered the avalanche may be estimated using a technique to measure very weak avalanches at the early stage of their development. Elimination of the capacitive response of the APD with the self-differencing circuit allows the detection of unsaturated avalanches, for which the output voltage scales with the number of detected photons [10]. This technique adds more complexity to the read-out electronics, and offer limited photon-number discrimination ability to SPADs.

One issue regarding the SPADs is the “afterpulsing” problem. It arises as the gain medium typically has trap sites which must be allowed to depopulate after an avalanche has occurred and before the bias voltage can be restored [11]. If those sites are not allowed to depopulate, a second avalanche can be initiated by

carriers released from traps rather than from a new photon. This necessitates additional waiting time where the detector is turned off, after a detection event. As a result, reliable operation of SPADs is rather slow. Later in this section, the most important performance factors for the SPADs are presented (Table 1.1) and compared with the other SPD approaches.

1.2. Superconducting Single Photon Detectors

Cryogenically cooled superconducting detectors have several fundamental and practical advantages which have resulted in their increasing adoption in a wide range of applications during the past decade. Apart from the excellent low noise performance which stems from the low operating temperature, different superconducting properties provide various mechanisms for high-sensitivity detection of light down to single-photon level. For instance, the sharp dependence of resistance with temperature in the superconducting-normal transition provides a sensitive thermometer for calorimetric and bolometric applications. The detector of this type, Transition Edge Sensor (TES) [12], is classified as a thermal equilibrium detector, which exhibits excellent sensitivity to the energy of the incident photon by operating near the normal transition temperature. The other class of superconducting detectors which are operated well below the transition temperature is called pair-breaking detectors, where the essential detection mechanism is based on the creation of quasiparticles in the superconducting material. In fact a photon with an energy $h\nu \geq 2\Delta$ incident on the superconducting film can be absorbed by breaking up Cooper pairs (paired electrons that carry a current without any resistance) and creating a number of quasiparticle excitations (with resistive charge transport). The nanowire superconducting single photon detector (SSPD) [13] is a promising example of this class of detectors which are the subject of this thesis. In the following the working principles of these two types of superconducting detectors are introduced.

1.2.1. Transition edge sensor (TES)

The operating principle of TES is based on calorimetric method. It consists of an absorber for the incident energy, with heat capacity C , in thermal contact with a superconducting thermometer to measure the temperature increase resulting from the absorption of energy. The temperature rise is sensed as the resistance increase of the TES film. The calorimeter must be thermally linked through a conductance G , to a heat sink or cold bath, kept at temperature T_b , which allows cooling of the absorber to its base temperature after each detection event (Fig. 1.2(a)) [14], [15]. The sensitivity necessary for measuring the energy of a single photon requires cooling to reduce the noise of the thermal and electrical systems. For high discrimination infrared photon counting, it is required that the

detector run at temperatures below 1K, usually in the 100 mK–200 mK temperature range. Superconducting TES's with tungsten as the active device material [16] show promising performance for visible and near infrared wavelengths. In these devices, the electron subsystem in the tungsten film acts as both the absorber and the thermometer. The low thermal coupling between the electrons and phonons in tungsten film provides a weak thermal link from the electron system to the phonon system, allowing the slow cool-down of electrons to the base temperature after photon absorption. The steep change in the resistance versus temperature of the superconducting tungsten film at critical temperature $T_C \sim 100$ mK results in a very sensitive measure of temperature (Fig. 1.2(b)), enabling precise resolution of the energy of one or more absorbed photons. Ideally, two photons cause a temperature rise that is twice that of a single photon. As a result, the TES generates an output signal that is proportional to the cumulative energy in an absorption event. This proportional pulse-height enables the determination of the energy absorbed by the TES and the direct conversion of sensor pulse-height into photon number.

In a TES, a constant bias voltage is applied to the device, increasing the electron temperatures in the sensor above the temperature of the substrate. When a photon is absorbed in the film, the electron temperature rises, increasing its resistance, which in turn decreases the current flowing through the sensor and hence reduces the Joule heating of the device. The inset in Fig. 1.2(b) illustrates the dynamic behavior of temperature and current in a photon detection process. In order to sense the very small changes in the current due to the temperature change after photon energy deposition, a superconducting quantum-interference device (SQUID) array must be used. A summary of the performance of TES is compared later in this chapter (Table 1.1) with other SPD approaches.

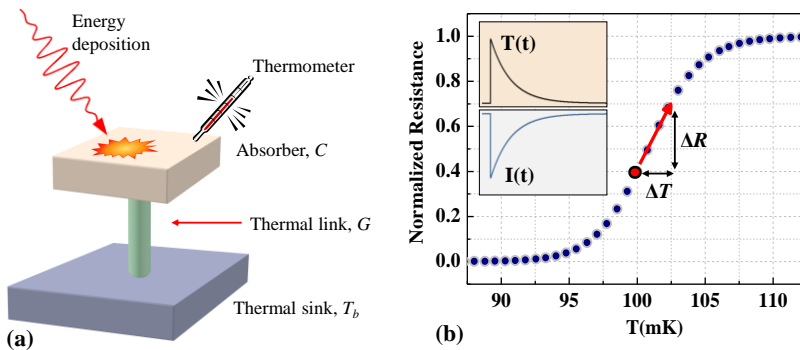


Fig. 1.2. (a) Schematic of the calorimetric operation of TESs from [14]. (b) Schematics of superconducting-normal transition [16]. Inset: Temperature and current transient behavior in a TES after photon detection.

1.2.2. Nanowire superconducting single photon detector (SSPD)

In this section, a brief introduction on the working principle of the single-photon detectors based on superconducting niobium-nitride (NbN) nanowires is provided. These nanometer-scale devices exploit the ultrafast nonequilibrium electronic photo-response in ultrathin films of the highly disordered superconductor (NbN) to produce single photon detection with unique speed and sensitivity, outperforming other existing SPDs. The detector consists of a single superconducting nanowire, with ~ 4 nm thickness and ~ 100 nm width. More details on the fabrication steps are provided in chapter 4 and 5. The wire is cooled to about 2–4 K, well below its critical temperature T_C (which for our NbN devices is around 10 K). Below T_C the wire is superconducting and has essentially zero electrical resistance, while above T_C the wire is in its normal (non-superconducting) state, in which it has a relatively high electrical resistance. The wire is biased with a direct current density sufficiently close to the critical current density J_C , above which the superconductivity breaks down. The SSPD is operated in a circuit schematically shown in Fig. 1.3. The bias-T provides the DC bias and transmits the RF signal to the load. The SSPD can be modeled as a time-varying resistor $R_n(t)$ in series with the intrinsic kinetic inductance of the nanowire L_k as is shown in Fig. 1.3.

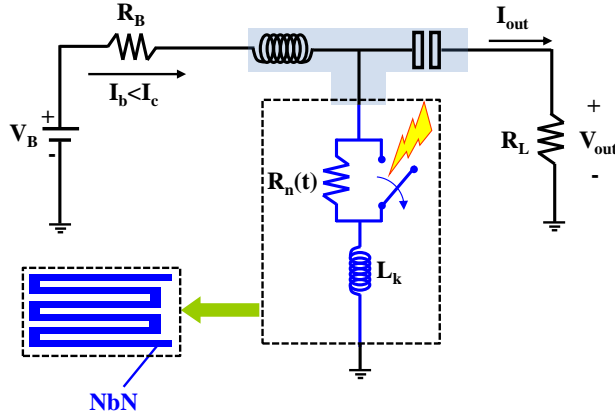


Fig. 1.3. Schematics of the electrical circuit for the operation of SSPDs.

The detection mechanism of SSPDs has been mainly explained through the hotspot model [17], [18]. Once a photon is absorbed in the superconducting strip, it breaks a Cooper pair, and, subsequently, a large number of quasiparticles are generated through the electron-electron and electron-phonon interactions. This creates a local perturbation, the so-called “hotspot”, where superconductivity is suppressed or destroyed. The hotspot is highly resistive and diverts the current around it. If the wire is sufficiently narrow, and if the bias current I_B is

sufficiently close to the critical value I_C , the formation of the hotspot can cause the current density to exceed the critical current density J_C locally as the charge carriers moving around the hotspot are forced both to accelerate and to increase in density. This can eventually result in disruption of superconductivity throughout an entire cross section of the wire, creating a resistive slab.

In the hotspot model, it is the deposited energy of the photon which acts as a seed for the formation of a normal region across the wire. The size of the seed rises as the energy of the photon increases. The supercurrent is expelled from this resistive seed and has to flow through the still superconducting portion of the wire. Since a normal domain forms over the entire cross-section of the wire when the current density in those superconducting sidewalks exceeds J_C , a spectral cut-off in the response of the SSPDs is expected when the photon energy and, consequently, the size of the normal seed are small. Also, at high bias currents, spontaneous transient resistive states are observed even in the absence of incident photons. The hotspot mechanism nicely explains the detection of photons with high enough energy, while the detection of near-infrared photons and dark counts can be explained by an assisting mechanism originated from the dissipative crossing of superconducting vortices [19], which is outlined below.

Nanowire SSPDs can be treated as a two-dimensional (2D) superconductor since the thickness of the nanowire is comparable to the superconducting coherence length ξ , whereas the width is much larger. In 2D superconductors, it is known that a phase transition called the Berezinskii-Kosterlitz-Thouless (BKT) transition can occur at the temperature T_{BKT} slightly below the critical temperature T_C [20]. Below T_{BKT} , bound vortex-antivortex pairs (VAPs) with no net flux exist, while in a temperature range between T_{BKT} and T_C , there are free vortices due to thermal unbinding of the VAPs. Even below T_{BKT} , the application of bias current in the superconducting nanowire exerts a Lorentz force that is conducted in opposite directions for the vortex and antivortex of a VAP. The bias current can finally overcome the binding energy of the VAP and break them into single vortices. Crossing of the unbound vortices in the nanowire perpendicular to the current may trigger the superconducting to normal transition. A photon makes this process much more probable by creating a hotspot i.e., quasiparticles of an elevated temperature, with lower energy barrier for vortex crossing. Also, spontaneous nucleation of a single vortex near the edge of the strip and its motion across to the opposite edge [21], [22] might release sufficient energy for the formation of a resistive belt across the wire.

Fig. 1.4 summarizes the different phenomena resulting in a creation of a normal-state belt across the wire: (a) a single photon with sufficient energy to create a resistive belt across the entire width of the strip, (b) a single photon of insufficient energy to create a resistive belt but initiating a subsequent vortex crossing, which provides the rest of the energy needed to create the resistive belt, and (c) thermally induced single-vortex crossing in the absence of photons,

which at high-bias currents provides the energy sufficient to trigger the transition to the normal state in a belt across the whole width of the wire [22].

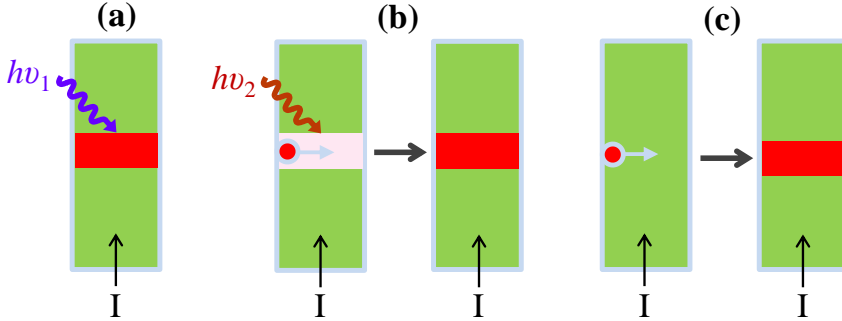


Fig. 1.4. Schematics of the formation of a normal slab across a biased superconducting nanowire which results in a detectable voltage pulse. (a) Direct photon count. (b) Vortex-assisted single-photon count. (c) Dark count [22].

After a resistive region is formed across the wire, it undergoes a further growth due to the Joule heating. At the same time, the bias current is redistributed to the load which will finally result in the cooling down and disappearance of the normal region as a result of a negative electrothermal feedback [23]. In this way, the wire resets to the superconducting state so that the succeeding single photons can be detected and counted by measuring voltage pulses. Fig. 1.3 shows a schematic of the SSPD circuit. In chapter 2, a more detailed model will be described.

With excellent high speed and high sensitivity performance, SSPDs show promise as an enabling technology in most SPD applications. In the following section the performance parameters of SPDs and particularly SSPDs are described.

1.3. Description of SPD's Performance Parameters

In the following, the performance characteristics for a single-photon detector are listed and the corresponding performance of SSPDs is discussed in detail.

1.3.1. Quantum efficiency (QE)

Quantum efficiency is an indication of how likely it is for the detector to measure a photon. The ideal SPD has efficiency of 100%, meaning that the detector does not lose any incident photon. The quality of coupling the photon flux to the active area of the detector and the probability of photon absorption in the detector material are also inherent in the quantum efficiency. To address

these parameters separately, one can define the system quantum efficiency of a detector as $SQE = \eta_c \times DQE$, where η_c is the coupling efficiency defined as the ratio of the number of photons coupled to the detector active area to the number of photons at the input of the cryostat. DQE (device quantum efficiency) is essentially the ratio of the detected photons to the number of photons coupled to the detector area. In fact, $DQE = A \times \eta_i$, where A is absorptance and η_i is the intrinsic quantum efficiency (the ratio of the detected photons to the number of photons absorbed in the detector). Note that the term quantum efficiency (QE) usually refers to the system QE.

To achieve efficient coupling of incoming photons from the 10 μm core of an optical fiber onto the narrow nanowire, the nanowire is fabricated in a meander structure [24], as illustrated in Fig. 1.5 for a detector with an active area of 5 $\mu\text{m} \times 5 \mu\text{m}$, consisting of a single 100 nm wide wire with 150 nm gaps between sections (40% fill factor) [25]. Depending on the optical setup, certain strategies can be employed to improve η_c . Recently, an etching aided alignment technique was employed to achieve very high SQE [26]. In this method the substrate of the SSPD is etched out to accommodate the optical fiber, which allows precise alignment of fiber without manual positioning.

NbN is highly resistive at optical frequencies, so it is a good optical absorber, e.g. a 4 nm-thick film has about 45% absorption at 1550 nm on a Sapphire substrate. However, it is a major technical challenge to take benefit of this high absorption in a nanowire photon counter. Indeed, the wire must be very narrow, much smaller than the wavelengths of interest. Maximizing the detection efficiency involves going beyond the limitation imposed by the absorptance of the 4 nm meander structures by increasing the absorption in the film through the integration of an optical microcavity, as will be explained in chapter 3.

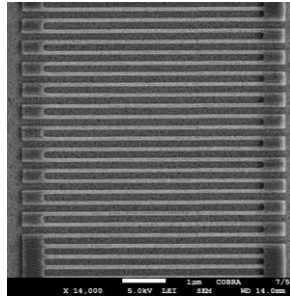


Fig. 1.5. Scanning-electron micrograph of a SSPD meander structure (by D. Sahin).

To maximize the internal efficiency of the SSPD, the quality of the film and the meander pattern must be optimized, specifically, the uniformity of the wire cross section along its length. If, for example, a small section of the wire is

narrower than the rest, it will limit the current that can be sent through the wire, since the current density will always be highest at this constriction. To have high detection efficiency, however, the current density must be very close to the critical value along the entire length of the wire. Therefore, any constriction will result directly into a low value of detection efficiency. The formation of a resistive slab after photon absorption, and hence the QE, has a strong dependence on the wavelength, temperature and the bias current. Fig. 1.6 shows a typical dependence of QE on bias current for two different temperatures. At the beginning of this PhD research, the state of the art value for SQE was 57% at 1550 nm on a NbN device on Sapphire substrate. Presently, the state of the art value has reached 93% for a WSi SSPD [26].

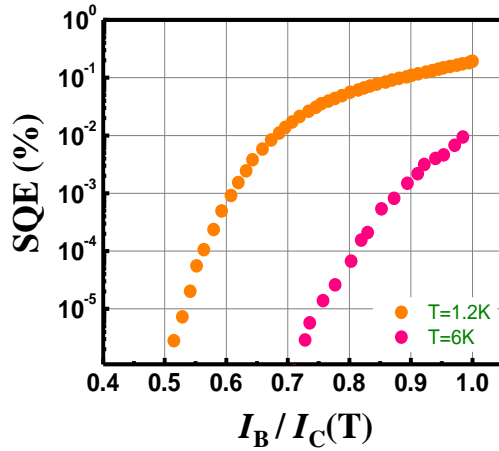


Fig. 1.6. A typical dependence of QE on bias current ratio for two different temperatures. The device is a standard $5 \times 5 \mu\text{m}^2$ NbN SSPD on GaAs with $d=4$ nm, $w=100$ nm, $f=40\%$.

1.3.2. Spectral response

Depending on the energy gap of the detector material, the energy of the absorbed photon is or is not sufficient to trigger a detection process. If the photon energy is less than the gap energy of the material, no detection event will occur. Therefore, the ability of the detector to undergo any detection mechanism is dependent on the wavelength of the incident photon.

Superconducting energy gap is orders of magnitude smaller than the semiconducting counterpart. However, detection in SSPD requires that many quasiparticles are produced leading to the creation of a resistive slab [27] across the whole width of the wire. The minimum number of quasiparticles that must be excited in the wire of a fixed width decreases with the increase of the bias current or the photon energy. Therefore, the cutoff should manifest itself as a decrease of

the detection efficiency if either the wavelength increases or the bias current decreases. Fig. 1.7 depicts the spectral sensitivity (QE versus wavelength) at different bias currents for a SSPD [28].

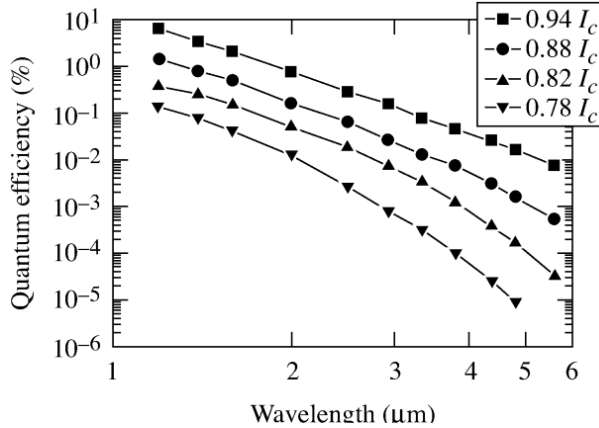


Fig. 1.7. Spectral response of NbN SSPD measured at 3 K for bias currents in the range of 0.78 to $0.94 \times I_c$, from [28].

As it was mentioned in the previous section, in order to increase the chance of optical absorption in SSPDs, integration of them with optical microcavities has been suggested [29]. This is achieved at the price of a narrower spectral response of the device. However for a large range of applications based on the use of optical fibers, which have the minimum loss and dispersion at wavelengths of $\lambda=1300$ nm and $\lambda=1550$ nm, it is greatly desirable that the detector spectral bandwidth include the telecommunication wavelength range.

1.3.3. Dark count rate (DCR)

It is not always the desired photon that triggers a detection event. In most of single photon detectors, there is a finite rate of an unwanted triggering of the detection process even in “dark” condition. Dark count can partially arise from the effect of the stray light or thermal infrared photons which can trigger detection. However, there is usually another “intrinsic” source of dark counts inherent in different SPD technologies. Depending on the material, the temperature, and the biasing condition, dark counts can be a limit in the high-performance behavior of a SPD. This can be mitigated by working in a gated mode, to have a reduced chance of dark detection in the desired timing window, at a price of added gating electronics.

SSPDs are also not excluded from the dark count. In SSPDs, the dark count rate (DCR) is suppressed as the bias current is reduced, but the quantum efficiency (QE) is also simultaneously reduced. Although shielding the device

from external radiation can suppress the dark count at lower bias current, but at high bias currents, the dark counts remain finite and are dominated by the spontaneous resistive-state formation which is a phenomenon intrinsic to thin film superconducting nanowire. The mechanism underlying the intrinsic dark count originates mostly from the vortex-antivortex-pair unbinding and single-vortex crossing under the influence of large Lorentz force at high bias currents [30]. Fig. 1.8 shows the current-dependence of dark count rate at different temperatures [30].

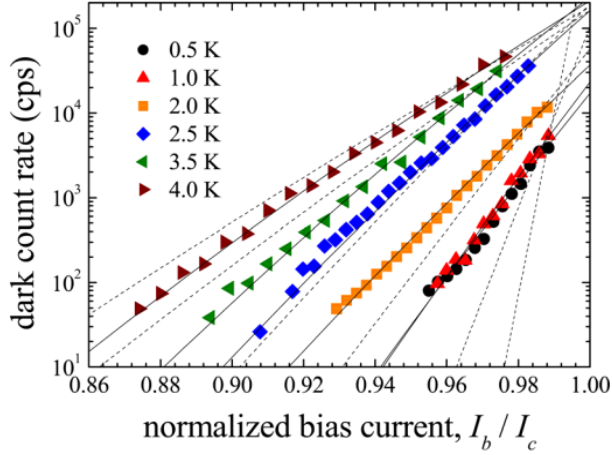


Fig. 1.8. Bias-current dependencies of the measured DCR at different temperatures together with the solid lines describing the DCR based on VAP unbinding model [30].

1.3.4. Dead time

In single photon detectors, after each photon detection event, the detector needs to be reset, gaining the ability for the next photon detection. In SSPDs this is usually done within a negative feedback loop, counterbalancing the change in the device resistance and in the Joule heating (this effect is explained in more detail in chapter 2) [31]. In SSPDs, the dead time includes two parts. The first is the interval during which superconductivity is interrupted and the detector is blind to the absorption of any other photon. This time is in the scale of few hundreds of picosecond in a standard $5 \times 5 \mu\text{m}^2$ area detector. The second part is the time interval during which the detector is superconducting and recovering its steady state current, to be able to efficiently register the arrival of the next photon. This period is governed by the inductive time constant of the circuit, which is imposed by the kinetic inductance of the NbN film due to the inertia of the Cooper pairs in the superconducting state [32]. The $1/e$ time constant of this recovery is about $\tau = 2 \text{ ns}$ in a standard $5 \times 5 \mu\text{m}^2$ detector with $L_K \sim 100 \text{ nH}$ kinetic

inductance, connected to a 50Ω load, which sets the main limit to the detector dead-time. Fig. 1.9 illustrates for example the calculated recovery time of the bias current, with the corresponding dead time (t_d) in a $5 \times 5 \mu\text{m}^2$ NbN meander SSPD in which the bias current is reduced due to the formation of the resistive region and then is recovered as a result of the negative feedback. The current recovers in $\sim 3 \times \tau$. In chapter 4 more discussions are given on the different ways to reduce the dead time in SSPDs and the limitations of it.

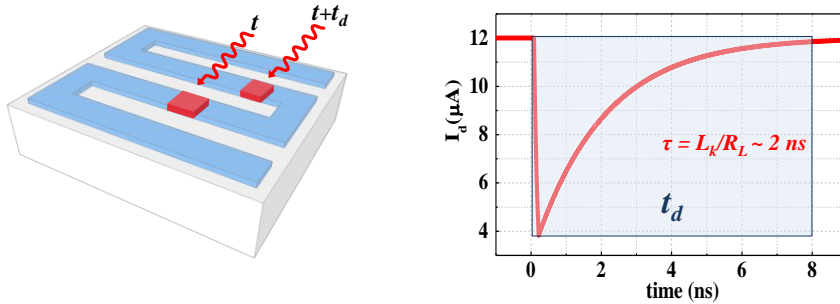


Fig. 1.9. Dead time (t_d) of SSPDs: the required time after the first photon detection event during which the bias current recovers back to its initial value. The data is a calculation based on a standard SSPD on GaAs substrate with the total of $L_k \sim 100 \text{ nH}$ and $R_L = 50 \Omega$, which allows $>100 \text{ MHz}$ count rate.

1.3.5. Timing resolution

When illuminated with narrow optical pulses, the onset of the output response of the detector may vary in time. The random variation in the time interval between the arrival of the photon and the corresponding electrical response of the detector is called the detector jitter. Fig. 1.10 illustrates the meaning of the jitter. As a random variable, the jitter has a Gaussian distribution and what is reported as jitter is the FWHM of its distribution. SSPDs have demonstrated jitters of less than 50 ps [33].

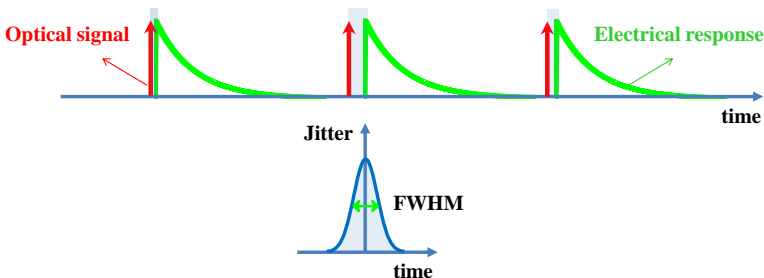


Fig. 1.10. Schematic illustration of the timing jitter.

The timing jitter may stem for example from the random position on the device where the impinging photon is absorbed or how the hotspot is formed and the thermalization of quasiparticles. Therefore, it might depend on the geometry and dimensions as well as the material of the detector. Jitter sets the temporal resolution in time-correlated single-photon counting measurements.

1.3.6. Photon-number resolving (PNR) capability

Photon-number resolution is the ability of the detector to register the number of photons that take part at the same time in a detection event. One can consider two classes of applications for which a PNR can be used. On one hand, in photonic quantum information processing, the number of photons produced in a setup (e.g. a probabilistic quantum gate) [34] must be accurately measured. This requires having a PNR detector with high QE, especially when detection of large photon states is required. Another application of the SND is to work as a very sensitive linear optical detector of classical light, determining the average number of photons in a weak coherent optical source, for example in ultra-long distance optical communication or optical time domain reflectometry.

In SPDs, the sensitivity at the single-photon level is often achieved by a very nonlinear internal gain process, which makes the detection a binary response, independent of the photon number. For instance, in SPADs the photo-excitation of a single (or more) carriers followed by carrier multiplication can result in a macroscopic current that saturates at a value which is not dependent on the number of photo-generated carriers that initiated the avalanche process [10] unless it is read-out through a self-differencing circuit. Similarly, in conventional SSPDs, the resistance of one hotspot before relaxation is much larger than the typical $50\ \Omega$ load. Therefore, the peak of the transient voltage photo-response depends mostly on the bias current and the load resistance, and not on the number of nucleated normal domains (see chapter 2). The readout of nanowire superconducting single photon detectors (SSPDs) with a high impedance load has also been proposed to add PNR functionality to these detectors, but this method produces latching of the detector in a permanent resistive state [35]. A general approach to realize a PNR detector is based on employing SPDs and multiplexing techniques. Time-multiplexing technique is based on splitting the multiphoton pulse via a cascade of beamsplitters and then delaying the signals so that they can be detected sequentially by single photon detectors [36]. But the presence of the delay loops results in a necessarily reduced count rate [37]. On the contrary, spatial multiplexing with a uniformly illuminated array of detectors preserves the maximum counting rate of the single-photon detecting elements of the array. PNR detectors based on spatially-multiplexed SSPDs have been fabricated by using an array of SSPDs either with separate readout for each element of the array [38], [39] (Fig. 1.11 (a)) or by connecting them in parallel and using a single readout [40], [41] (Fig. 1.11 (b)).

A detector geometry allowing a single readout of the photon number is particularly promising in view of simplicity of use and scalability to large photon numbers. However, the parallel nanowire detector (PND) explored so far is limited in terms of dynamic range (maximum number of photons which can be detected in a pulse), and efficiency due to the problem of current redistribution in the array after photon detection in one or more wires, as it will be discussed in chapter 4. Fig. 1.11(c) illustrates an example of PNR behavior shown previously by using parallel nanowire detectors.

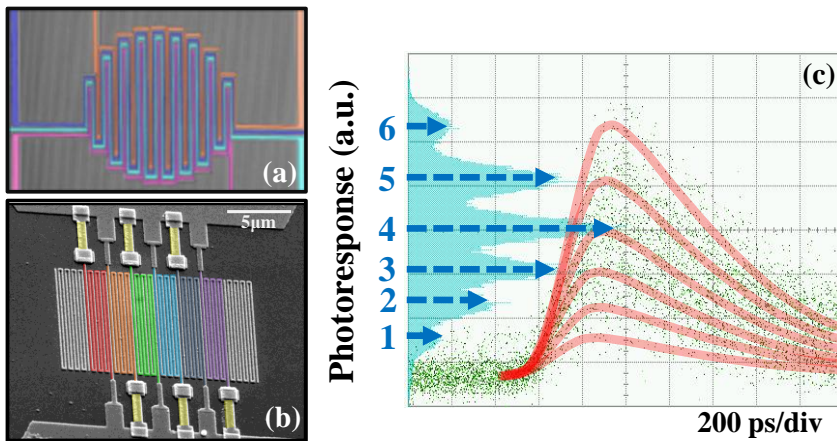


Fig. 1.11. (a), (b) Scanning electron micrographs of PNR structures based on superconducting nanowires spatially-interleaved multi-element detector [39], and parallel nanowire detector [40], respectively. (c) The oscilloscope persistence trace of the output voltage levels and the related histogram of the PND photoresponse showing the ability to count up to 6-photon detection event.

1.4. Comparison of Different SPD Technologies

Now that the most important parameters of single photon detectors are introduced, a comparison is made in between the state-of-the-art characteristics of SSPDs and other promising single photon detector technologies: SPADs and TESs through table 1.1, at the standard telecom wavelength of 1550 nm.

While Si-SPADs are good candidate of single-photon detection in the visible range, InGaAs SPADs, suitable for the telecom wavelength window, suffer from afterpulsing, low QE and high dark counts, therefore are being surpassed by superconducting detectors. TES devices have high QE, low dark count and intrinsically offer PNR detection with single photon sensitivity in a relatively large range, but they have several drawbacks which are overcome by SSPDs. For

instance, TES devices have maximum counting rate at least two orders of magnitude lower than SSPDs. Furthermore, they operate at ~ 100 mK and require complex cryogenic equipment, whereas SSPDs can work at higher temperatures even at the boiling point of liquid helium, which is easily achievable by common cooling technologies. While in SSPDs adequate signal-to-noise ratio can be achieved through room-temperature amplification, TES devices demand SQUID-based read-out, which also degrades their timing resolution because of the relatively large input inductance. These are the prices paid to make TESs the energy-resolving detectors with resolution at the phonon noise limit. Granting SSPDs with the ability to discriminate photon number while preserving all their advantageous properties will make them future devices for many applications from quantum information science to astronomical observations. At the moment the maximum dynamic range for PNRs based on superconducting nanowires are in the range of 4–6 photons range [39], [40]. In a multiplexed photon-number-resolving scheme, in order to reduce the possibility that two or more photons are absorbed in the same pixel, it is necessary to have large number of pixels. And evidently to increase the fidelity with which an n -photon state can be recorded, high QE detecting elements are greatly desirable.

Table 1.1 Comparison of the different SPD technologies at $\lambda = 1550$ nm [11]

	T(K)	SQE (%) 1550nm	DCR(Hz)	Jitter (ns)	Dead time (ns)	PNR dynamic range	Readout
InGaAs SPAD	240	10	16000	0.05	10	4*	Quenching circuit
TES	0.1–0.3	99	—	100	1000	32	SQUID
SSPD	1–2	50-90	10	0.03–0.1	1–10	4–6	50 Ω amplifier

It is also worth to mention that although all of these detectors involve in the conversion of individual photons into an electrical signal, the readout electronics are important as well. Therefore the simplicity of the readout electronics in SSPDs is a great privilege.

1.5. Goal of This Thesis

In this thesis I have investigated different approaches to PNR detection using superconducting nanowire detectors. The ideal PNR detector would measure photon numbers in a large dynamic range (e.g. 1–30 photons) and with high

* This PNR capability is achieved through the self-differencing circuit.

fidelity. This requires optimized detector configuration and electrical read-out as well as a method to boost the efficiency. For this reason, I have studied two configurations based on superconducting nanowires: the parallel nanowire detector (PND) and the series nanowire detector (SND), together with a well-known approach based on microcavity structures to increase the efficiency.

1.6. Outline of the Thesis

In chapter 2, experimental methods, including testing setup and procedures, as well as simulation methods are described. The latter are based on a one-dimensional time-dependent heat equation which is solved together with the electrical equations governing the detector, in order to investigate the dynamics of the photoresponse. In chapter 3, the design of an optical microcavity structure is introduced in order to boost the quantum efficiency of the device on GaAs substrate. This is achieved by integrating a highly reflective bottom mirror which increases the light absorption into the active thin device material in a particular wavelength range. In chapter 4, the previously fabricated PNRs based on parallel connection of SSPDs are reviewed together with the simulations that investigate the fundamental limitations of their performance. In chapter 5 a novel design for a PNR structure based on a series configuration is reported, along with the proof of principle experimental results, which show promise for the development of future large dynamic range superconducting PNR devices. Essential means of readout for these devices is a high impedance cryogenic preamplifier. A simple implementation of such amplifier based on a high electron mobility transistor is also demonstrated. Finally, chapter 6 summarizes and concludes my work.

References

- [1] L.-Q. Li and L. M. Davis, "Single photon avalanche diode for single molecule detection," *Review of Scientific Instruments*, vol. 64, no. 6, pp. 1524, 1993.
- [2] S. Felekyan et al., "Full correlation from picoseconds to seconds by time-resolved and time-correlated single photon detection," *Review of Scientific Instruments*, vol. 76, no. 8, pp. 083104, 2005.
- [3] A. P. Morrison et al., "Single photon avalanche detectors for low light level imaging," *Proc. of SPIE*, vol. 3114, pp. 30, 1997.
- [4] M. Viterbini, A. Adriani, and G. Donfrancesco, "Single photon detection and timing system for a LIDAR experiment," *Review of Scientific Instruments*, vol. 58, no. 10, pp. 1833, 1987.

- [5] J. Hu et al., "Photon-counting optical time-domain reflectometry Using a superconducting single photon detector," *Journal of Lightwave Technology*, vol. 30, no. 16, pp. 2583-2588, 2012.
- [6] R. H. Hadfield, "Single-photon detectors for optical quantum information applications," *Nature Photonics*, vol. 3, no. 12, pp. 696-705, 2009.
- [7] N. Gisin, R. Thew, and A. Physics, "Quantum communication," *Nature Photonics*, vol. 1, pp. 165-171, 2002.
- [8] A. Baryshev et al., "Progress in antenna coupled kinetic inductance detectors," *IEEE Transactions on Terahertz Science and Technology*, vol. 1, no. 1, pp. 112-123, 2011.
- [9] F. Zappa, S. Tisa, A. Tosi, and S. Cova, "Principles and features of single-photon avalanche diode arrays," *Physical Sensors and Actuators*, vol. 140, no. 1, pp. 103-112, 2007.
- [10] B. E. Kardynał, Z. L. Yuan, and A. Shields, "An avalanche photodiode-based photon-number-resolving detector," *Nature Photonics*, vol. 2, no. 7, pp. 425-428, 2008.
- [11] M. D. Eisaman, J. Fan, A. Migdall, and S. V. Polyakov, "Invited Review Article: Single-photon sources and detectors," *Review of Scientific Instruments*, vol. 071101, pp. 071101, 2011.
- [12] B. Cabrera et al., "Detection of single infrared, optical, and ultraviolet photons using superconducting transition edge sensors," *Applied Physics Letters*, vol. 73, no. 6, pp. 735, 1998.
- [13] G. N. Gol'tsman et al., "Picosecond superconducting single-photon optical detector," *Applied Physics Letters*, vol. 79, no. 6, pp. 705, 2001.
- [14] D. Rosenberg, A. E. Lita, A. J. Miller, and S. W. Nam, "Noise-free high-efficiency photon-number-resolving detectors," *Physical Review A*, vol. 71, pp. 1-4, 2005.
- [15] A. E. Lita, A. J. Miller, and S. W. Nam, "Counting near-infrared single-photons with 95% efficiency," *Optics Express*, vol. 16, no. 5, pp. 3032-3040, 2008.

- [16] A. E. Lita, B. Calkins, L. A. Pellouchoud, A. J. Miller, and S. Nam, "Superconducting transition-edge sensors optimized for high-efficiency photon-number resolving detectors," *Proc. of SPIE*, vol. 7681, pp. 1-10, 2010.
- [17] G. N. Gol'tsman et al., "Picosecond superconducting single-photon optical detector," *Applied Physics Letters*, vol. 79, no. 6, pp. 705, 2001.
- [18] A. D. Semenov, G. N. Gol'tsman, and A. A. Korneev, "Quantum detection by current carrying superconducting film," *Physica C*, vol. 351, pp. 349-356, 2001.
- [19] G. R. Berdiyrov, M. V. Milosevic, and F. M. Peeters, "Spatially dependent sensitivity of superconducting meanders as single-photon detectors," *Applied Physics Letters*, vol. 100, 262603, 2012.
- [20] A. Engel, K. Il, and M. Siegel, "Fluctuation effects in superconducting nanostrips," *Physica C*, vol. 444, pp. 12-18, 2006.
- [21] L. Bulaevskii, M. Graf, C. Batista, and V. Kogan, "Vortex-induced dissipation in narrow current-biased thin-film superconducting strips," *Physical Review B*, vol. 83, no. 14, pp. 1-9, 2011.
- [22] L. N. Bulaevskii, M. J. Graf, and V. G. Kogan, "Vortex-assisted photon counts and their magnetic field dependence in single-photon superconducting detectors," *Physical Review B*, vol. 85, no. 1, pp. 1-10, 2012.
- [23] A. Kerman, J. Yang, R. Molnar, E. Dauler, and K. Berggren, "Electrothermal feedback in superconducting nanowire single-photon detectors," *Physical Review B*, vol. 79, no. 10, pp. 1-4, 2009.
- [24] A. Verevkin et al., "Detection efficiency of large-active-area NbN single-photon superconducting detectors in the ultraviolet to near-infrared range," *Applied Physics Letters*, vol. 80, no. 25, pp. 4687, 2002.
- [25] A. Gaggero, S. Jahanmirinejad, F. Marsili, F. Mattioli, R. Leoni, and D. Bitauld, "Nanowire superconducting single-photon detectors on GaAs for integrated quantum photonic applications," *Applied Physics Letters*, vol. 97, 151108, 2010.

- [26] F. Marsili et al., “Detecting single infrared photons with 93 % system efficiency,” *arXiv:1209.5774*, 2012.
- [27] A. Semenov, A. Engel, H.-W. Hubers, K. Ilin, and M. Siegel, “Spectral cut-off in the efficiency of the resistive state formation caused by absorption of a single-photon in current-carrying superconducting nanostrips,” *The European Physical Journal B*, vol. 501, pp. 495-501, 2005.
- [28] G. Gol’tsman et al., “Middle-infrared to visible-light ultrafast superconducting single-photon detectors,” *IEEE Transactions on Applied Superconductivity*, vol. 17, no. 2, pp. 246-251, 2007.
- [29] V. Anant, A. J. Kerman, E. A. Dauler, K. W. Joel, K. M. Rosfjord, and K. K. Berggren, “Optical properties of superconducting nanowire single-photon detectors,” *Optics Express*, vol. 16, no. 14, pp. 46-52, 2008.
- [30] J. Kitaygorsky et al., “Origin of dark counts in nanostructured NbN single-photon detectors,” *IEEE Transactions on Applied Superconductivity*, vol. 15, no. 2, pp. 545-548, 2005.
- [31] A. J. Kerman, J. K. W. Yang, R. J. Molnar, E. A. Dauler, and K. K. Berggren, “Electrothermal feedback in superconducting nanowire single-photon detectors,” *Physical Review B*, vol. 79, no. 100509, 2009.
- [32] A. J. Kerman et al., “Kinetic-inductance-limited reset time of superconducting nanowire photon counters,” *Applied Physics Letters*, vol. 88, no. 11, pp. 111116, 2006.
- [33] J. Zhang et al., “Response characterization of superconducting single photon detectors,” *IEEE Transactions on Applied Superconductivity*, vol. 13, no. 2, pp. 180-183, 2003.
- [34] E. Knill, R. Laflamme, and G. J. Milburn, “A scheme for efficient quantum computation with linear optics,” *Nature*, vol. 409, no. 6816, pp. 46-52, 2001.
- [35] J. Kitaygorsky, S. Dorenbos, E. Reiger, R. Schouten, and V. Zwiller, “HEMT-based readout technique for dark- and photon-count studies in NbN superconducting single-photon detectors,” *IEEE Transactions on Applied Superconductivity*, vol. 19, no. 3, pp. 346-349, 2009.

- [36] M. Fitch, B. Jacobs, T. Pittman, and J. Franson, "Photon-number resolution using time-multiplexed single-photon detectors," *Physical Review A*, vol. 68, no. 4, pp. 1-6, 2003.
- [37] P. Eraerds, E. Pomarico, J. Zhang, B. Sanguinetti, R. Thew, and H. Zbinden, "32 bin near-infrared time-multiplexing detector with attojoule single-shot energy resolution," *The Review of scientific instruments*, vol. 81, no. 10, pp. 103105, 2010.
- [38] E. A. Dauler et al., "Multi-element superconducting nanowire single-photon detector," *IEEE Transactions on Applied Superconductivity*, vol. 17, no. 2, pp. 279-284, 2007.
- [39] E. A. Dauler et al., "Photon-number-resolution with sub-30-ps timing using multi-element superconducting nanowire single photon detectors," *Journal of Modern Optics*, vol. 56, no. 2-3, pp. 364-373, 2009.
- [40] A. Divochiy et al., "Superconducting nanowire photon-number-resolving detector at telecommunication wavelengths," *Nature Photonics*, vol. 2, no. 5, pp. 302-306, 2008.
- [41] F. Marsili et al., "Physics and application of photon number resolving detectors based on superconducting parallel nanowires," *New Journal of Physics*, vol. 11, no. 4, pp. 045022, 2009.

CHAPTER 2

Methods

In this chapter, first the experimental setup and the equipment used to perform the characterization measurements of superconducting nanowire detectors are introduced. Depending on the application, different cryogenic setups can be employed for the characterization of the SSPDs. The setups differ from each other in terms of the cooling procedure and the lowest achievable temperature, the number of devices which can be screened simultaneously, and the type of device illumination. Later in this chapter, the details about the simulation techniques for SSPDs are described. The modeling of SSPDs requires an understanding of their optical, electrical and thermal properties. In this chapter, by considering the electrical and thermal properties of the nanowire, the detection process from the instance when the photon absorption causes a normal belt-like domain across the nanowire, until a voltage pulse appears, will be modeled. This helps to understand how the device works and how its speed performance can be improved. The optical modeling of SSPDs and a design of an optical cavity to enhance the absorptance of light at the detector will be the objective of chapter 3.

2.1. Cryogenic Setups

2.1.1. *Micro-manipulated probe station*

The main setup that was used for the electro-optical characteristics of superconducting detectors during this work is the cryogenic probe station from Janis model ST-500 (initially designed and tested by Dr. David Bitauld). This continuous flow cryostat has an integrated vacuum chamber, a sample mount, and a cooled radiation shield. The sample is mounted on a removable sample holder and is surrounded by a thermal shield to minimize radiant sample heating, providing the lowest possible sample temperature. A high efficiency transfer line is used to provide sample cooling using liquid He (LHe), and includes an integrated adjustable cryogen flow control needle valve. The vacuum is provided through a Turbo-pump station including a 52 L/s turbo-molecular pump, a wide range vacuum gauge and readout, and a stainless steel flexible pumping line. Two silicon diode thermometers, installed at the control heat exchanger and at

the sample mount, together with a high wattage cartridge heater are used to regulate and monitor the sample stage temperature within the operating temperature range of ~ 3.5 K–425 K [1].

In order to achieve a good thermal contact, the type of the adhesive material which is used to stick the sample to the gold-plated sample holder is very critical. A smooth, thin layer of cryogenic thermal varnish is applied on the sample holder and the sample is immediately mounted and gently pressed into the paste to remove the air. This step should be done very fast, before the drying of the glue. During this work two types of adhesive material were used. First is the silver paste with a good thermal conductivity, which dries very fast and can be removed easily with acetone. The problem with this paste is that after a while its quality was degraded and the presence of some particles avoided having a uniform layer and a good thermal contact. Another high thermally conducting varnish that we used is Lakeshore product VGE-7031 (formerly GE-7031 Varnish). This product is excellent in making thermal contact, but care should be taken while removing a sample which has been stuck to the holder with this type of varnish. To do so, the sample is dipped into acetone for few minutes and then gently pushed with the tweezers. Apart from the varnish, two small copper clamps are usually mounted at two sides of the sample to improve the thermal link between the sample surface and the holder.

The cryostat has micro-manipulated translation stages. Independent X, Y, Z stages provide precise control over the probe motion within the range of travel. A 40 GHz microwave probe in a ground-signal-ground (GSG) configuration is used with 100 μm pitch. The probe, supported with a probe arm, is connected to a semi-rigid coaxial cable terminating with SMA connector. The probe is cooled at ~ 20 –25 K using copper braids connected to the 10 K stage of the probe station. Because of the heat flow from the microprobe to the sample, and of the radiant heating from the holes in the thermal shield in correspondence of the probe, the temperature of the devices is about $T \sim 5$ K. A schematic of the cryogenic setup is shown in Fig. 2.1.

Optical access to the sample is provided through the top window of the cryostat. In Fig. 2.1 the schematic of the optical apparatus is also shown and the optical path is indicated. A cooled radiation shield window blocks the black body radiation that would couple to the sample through the optical window. This window, which is mounted in an aluminum frame, is called cold filter, and has an optical bandwidth transparent for visible and near infrared wavelengths. Free space optics are attached to a movable mount, supported by XYZ, computer-controlled stage with 50 nm step size (Thorlabs motorized servo actuator with TDC001 motion controller). The stage is mounted on the cryostat to allow free-space optical coupling to the cold sample. A single-mode optical fiber (SMF-28) is mounted to the stage which is illuminated by a 1.3 μm -wavelength diode laser. The light is collimated and split into two arms. In one arm, a calibrated

powermeter (OPHIR) is used to measure the incident light intensity, for power normalization purposes (not shown). In the other arm, a long-working-distance (24 mm), high numerical aperture (NA=0.4) reflective objective is used to focus the 1.3 μm -wavelength light into a spot of $\sim 2 \mu\text{m}$ diameter on the device area. In order to image the device and roughly align the light spot to it, the laser is replaced with a white light source. Light reflected from the device (gold pads) is collected and sent to a CCD camera. The fine adjustment of the laser spot relative to the active surface of the device is achieved during the measurement by using the count rate of the SSPD as a feedback. In the case of SSPDs with very small active area ($\ll 1 \mu\text{m}^2$), the beam spot size can be measured by scanning the spot over the device in x and y directions [2].

The advantage of the probe station setup is that it allows screening of hundreds of devices in a chip during one cool-down at a temperature of about 5 K. Therefore, it is used as the preliminary setup for characterizing every sample batch.

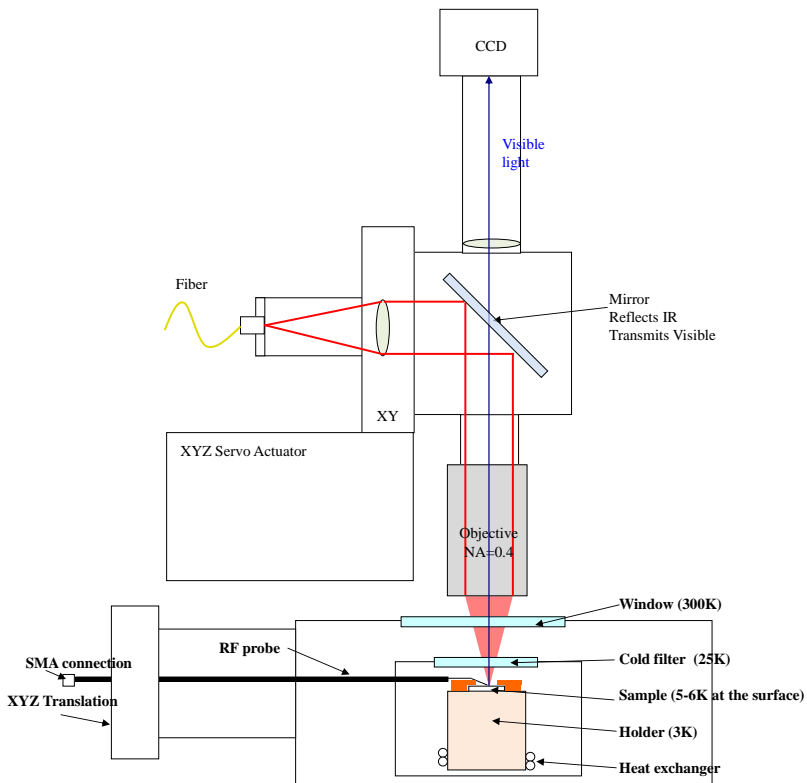


Fig. 2.1. Schematic of the probe station setup

2.1.2. Cryogenic dipstick

The most straightforward method for cooling a SSPD is to immerse it in liquid helium (He) and reach the boiling temperature of liquid helium, 4.2 K. This is done using a cryogenic dipstick setup (developed by Dr. F. Marsili). The sample is glued to the dipstick sample holder and the device signal pad is wire bonded to the heat sink pads (Lakeshore) which are thermally anchored to the sample holder through cryogenic varnish. As the sample holder shares the ground with the whole setup, the ground pad of the device can be bonded to any place on the surface of the sample holder. Then the miniature coaxial cable of the dipstick is indium soldered to the pad, as described in [3] to eventually provide the electrical connection between the device and the room-temperature SMA connector. Mounting a sample in the probe station is critical and a bad thermal contact between the sample and the holder prevents reaching the low temperatures required for measuring SSPDs. The advantage of the dipstick setup, other than its ease of use, is that it provides a constant unambiguous temperature. Therefore, it is often used to double-check a measurement done in the probe station, and to measure the devices which are not physically accessible with the probe*. In the dipstick setup, it is possible to access few devices in the same cool-down. To this aim, the beam from the fiber is focused by a lens and then allowed to diverge (see Fig. 2.2) in order to produce a $\sim 1 \text{ cm}^2$ illuminated area on the sample. A measurement of the light intensity at this point provides the normalization needed for the calculation of the device QE. However, the uniform illumination is also the reason of the poor coupling efficiency in this setup.

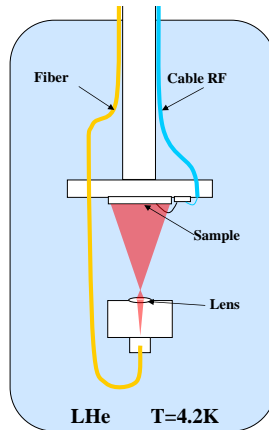


Fig. 2.2. Schematic of the dipstick setup

* On each sample chip, there are some devices for the processing test, such as wide NbN bridges which do not have the standard pads compatible with the probe.

2.1.3. Closed-cycle cryocooler

Mounting SSPDs in a cryogenic probe station or a dipstick is mostly satisfactory in a low-temperature research laboratory. However if the goal is to provide a working device for users in other scientific fields or in industrial applications, alternative cooling methods must be used. Operating SSPDs in a closed-cycle cryocooler which does not need the repeated cryogenic handling [4] is a good solution. Some of the experiments in this thesis (chapter 5) are carried out in such a system. The cryostat operates at a base temperature of about 1.5 K. It is essentially composed of two stages: A Pulse Tube Cooler (PTC) [5] integrated in a Dewar, and a small Joule-Thompson (JT) closed cycle. In principal, a “1 K-pot” stage is integrated into a standard 4 K cryostat. When PTC cools the system down to about 4 K, warm helium gas from an external tank is injected into a dedicated circuit. The helium is pre-cooled and forced through a JT stage where it experiences an irreversible adiabatic expansion with an associated temperature reduction. Thermodynamic conditions to condense helium in the pot are achieved. A part of the liquid is then evaporated via an external oil-free pump, resulting in an effective cooling of the stage to less than 1.5 K. Equilibrium is reached between the continuously evaporating helium leaving the pot and the liquefied helium coming from the JT stage. An extra pre-cooling helium circuit allows accelerating and controlling the cooling procedure from room temperature to about 4 K. Fig. 2.3 shows the cryostat with the 3 plates at 70, 4 and 1.5 K and the integrated JT refrigerator. The cryostat is mounted into a portable and rotatable cart. The main difference between cryo-coolers and flow or bath cryostats is that refrigeration is provided in a closed-loop system which eliminates the cost of continually supplying liquid helium. The system can run continuously without the need to recycle, with a good stability of temperature, thanks to the high cooling power at base temperature [6].

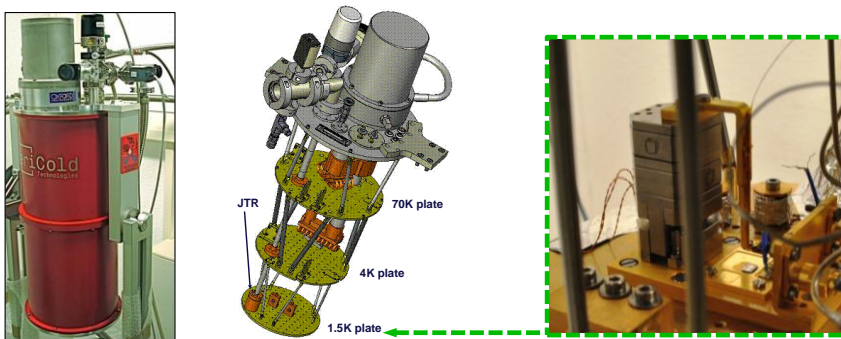


Fig. 2.3. (Left) The Veri-Cold closed cycle cryocooler setup. (Middle) Schematic of the setup with 3 plates at 70, 4 and 1.5 K, and the integrated JT refrigerator. (Right) The piezo stage aligning a fiber on top of the device.

From a practical point of view what is important for a single photon application is the system quantum efficiency including all the coupling losses. In the closed-cycle cryocooler, in order to improve the coupling of the fiber to the active area of the device, a lensed fiber is used with a $1/e^2$ spot size of $2.5 \mu\text{m}$. It is mounted on XYZ piezo-positioners to perform in situ alignment so that the coupling is close to unity when the light beam is perfectly focused at the center of the device area. The optimization is first carried out at room temperature and then at cryogenic temperature, based on measuring the back-reflected power, similar to the method in Ref. [7]. We noticed that the fiber is retracting about $100 \mu\text{m}$ during cooling down at 1.1 K pointing out the importance of the alignment at cryogenic temperatures. Finally, in-plane alignment is performed at cryogenic temperature by monitoring the detector count rate while scanning the fiber position in x and y directions. Three heat shields of the cryocooler, attached to the 70 K, 4 K and 1 K plates, provide good shielding of the detector from blackbody radiation allowing measurements with very low dark count rates. In Fig. 2.3, the piezo stage is shown with a fiber mounted on it.

2.2. Experimental Setup

The scheme for the electronic setup is shown in Fig. 2.4. The bias current is supplied through the DC port of a bias-T (mini-circuits 10 MHz–6 GHz) by a voltage source (Yokogawa 7651) in series with a 10Ω bias resistor. For the electrical characterization, the bias-T is solely used as a lowpass filter to remove the noise of the bias source, while its RF arm is terminated with a 50Ω matched load.

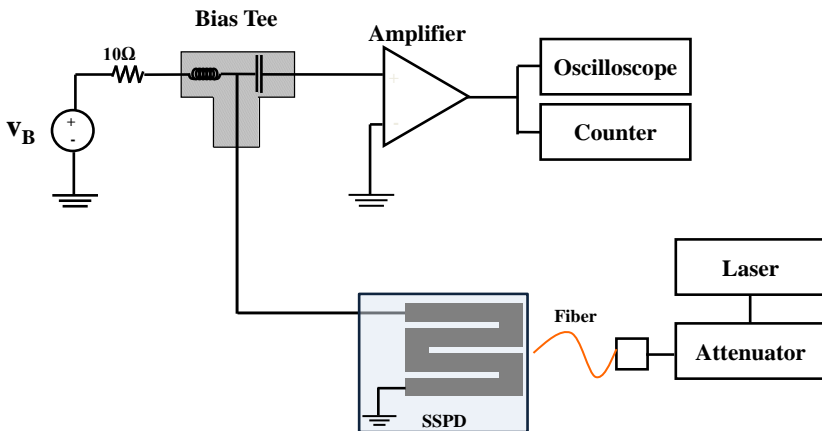


Fig. 2.4. Schematic of the experimental setup

For the optical characterization, the light produced by a fiber-pigtailed, gain-switched laser-diode at $1.3 \mu\text{m}$ wavelength, with 50 ps-long pulses at a maximum repetition rate of 26 MHz, is fed to the device. The laser pulses are attenuated through a variable fiber attenuator, to reach down to the single-photon level. The electrical response of the detector is collected through the RF arm of the bias-T. The magnitude of an un-amplified voltage pulse from a standard SSPD is usually less than 1 mV. Therefore, the pulse needs to be amplified to trigger the commercial counters. In our case this weak pulse exiting the cryostat is amplified using a chain of 50Ω matched, room-temperature amplifiers. (Mini-circuits 20 MHz–6 GHz). Then the amplified signal is directed either to a counter, a single shot oscilloscope or a sampling oscilloscope for optical characterization.

An example of current-voltage (I-V) characteristic of a SSPD measured in the probe station setup is displayed in Fig. 2.5 (dark blue line). A detailed explanation can be found in Ref. [8]. In the superconducting state, there is no voltage drop across the device and an infinite slope is expected for the I-V curve. But since in practice we measure the sum of the voltage drops across the device plus the small resistances in the line, there is a finite slope (corresponding to 18Ω resistance) which is the manifestation of the bias circuit resistance (bias resistor + bias-T and cable resistors), which can be easily corrected (light blue line). As the bias current exceeds the critical current of the most constricted wire, that wire switches to the normal state, followed by relaxation oscillations (which are not measurable with our electronics).

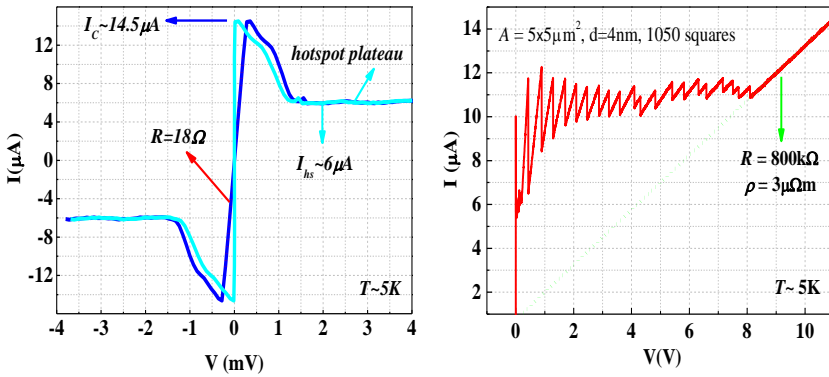


Fig. 2.5. I-V characteristics of two standard $5 \times 5 \mu\text{m}^2$ SSPDs on GaAs, with $d=4 \text{ nm}$, $w = 100 \text{ nm}$, $f=40\%$, measured in the probe station. (Left) In a low range of voltages, used to extract the hotspot current, (Right) In a large range of voltages, used to extract the normal domain resistance R , and resistivity ρ [3].

The maximum value of the bias current, over which the most constricted wire switches to the normal state, is the critical current I_C of the wire. In the device shown in Fig. 2.5 (left), $I_C=14.5 \mu\text{A}$. Also in this figure, the hotspot plateau can be seen with the hotspot current $I_{\text{hs}}=6 \mu\text{A}$. This current corresponds to the minimum current required to sustain a normal hotspot in the wire section [9]. The value of I_{hs} is used to estimate the heat transfer coefficient per unit area to the GaAs substrate [9]. In Fig. 2.5 (right), the transition of the different branches of the meander (due to cross-heating effects between them and the inhomogeneities of the meander cross section) is observed. When the total length of the meander becomes resistive, the nanowire shows ohmic behavior, from which the normal resistivity of the NbN is estimated, which is required for the electro-thermal simulation.

Fig. 2.6 shows a typical voltage response of the SSPD measured with a digital phosphor oscilloscope (Tektronix 5104). The pulse amplitude depends on the applied bias current and the pulse rise time is well below 1 ns. The impedance of the mini-coaxial cable that picks up the signal from the sample holder might differ a little from 50Ω . This causes some reflections of the signal, resulting in the features that can be seen in the pulse shape.

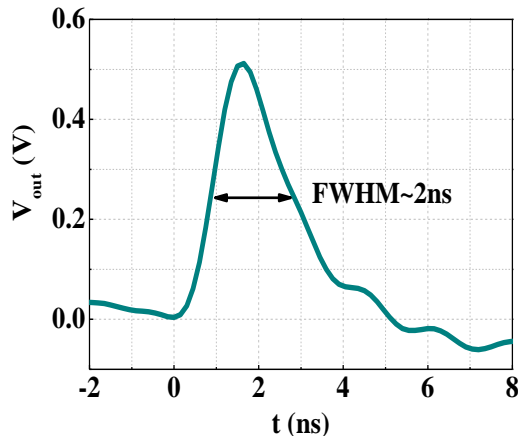


Fig. 2.6. The amplified voltage pulse shape of a standard $5 \times 5 \mu\text{m}^2$ SSPD on GaAs, with $d=4 \text{ nm}$, $w=100 \text{ nm}$, $f=40\%$, measured in the probe station.

To study the photo-count statistics of the device, the detection events are counted by a counter with a bandwidth of 200 MHz manufactured by Hameg (model 8123). The counter is equipped with an internal discriminator to set a trigger level on the counting events. The ideal setting of the discriminator level had to be estimated before each measurement by scanning through a series of discriminator levels. At low discriminator levels the counter counts all kinds of noise signals, at high discriminator levels the counter does not count at all. In

between one should observe a plateau, which means that the count rate is independent of the discriminator level. Figure 2.7 shows a measurement of the pulse-counter's count rate as a function of the discriminator level using the SSPD. The negative pulse comes from the odd (three) number of amplifiers in the chain, as each amplifier changes the phase by 180° . The blue dashed line shows the proper level of trigger chosen to remove all the electrical noise.

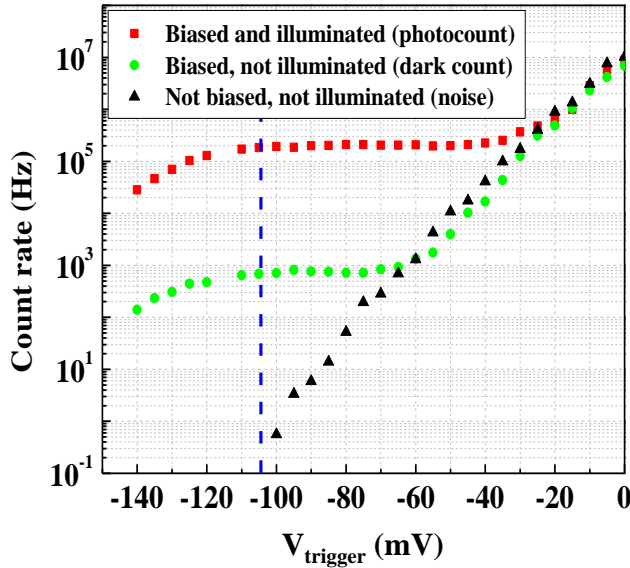


Fig. 2.7. Count rate as a function of the counter trigger level for a standard $5 \times 5 \mu\text{m}^2$ SSPD on GaAs, amplified by a chain of three amplifiers, measured at 3 different conditions.

After choosing the right discriminator level, the count rate is scanned for a range of bias currents, in order to investigate the quantum efficiency of the device (DQE). The dependence of the number of detector counts per second on the average number of photons per pulse (not shown) must be proven to be linear for the photon fluxes used in DQE measurements, proof that true single photon detection is observed. The DQE at a given bias current I_B is calculated as: $\text{DQE} = (N_c - R)/N_{\text{ph}}$, where N_c is the number of detection events registered by the counter in one second, N_{ph} is the number of photons incident on the device area and R is the dark count rate at I_B , measured with the optical input blocked (see chapter 1).

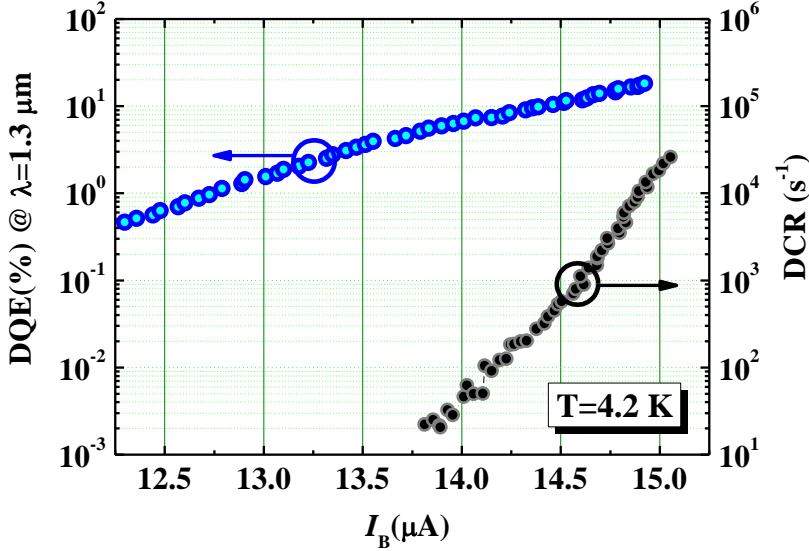


Fig. 2.8. Device quantum efficiency (left axis) and dark count rate (right axis) for a $5 \times 5 \mu\text{m}^2$ SSPD on microcavity structure (see chapter 3) measured in the dipstick setup at 4.2 K, as a function of the bias current. The incident photon wavelength is 1300 nm.

2.3. Electro-Thermal Model

In this section, the SSPD is modeled by considering the thermal and electrical responses of the nanowire coupled with each other. The thermal response pertains to the switching of the nanowire from superconducting to normal state and back during a photodetection process, whereas the electrical response involves the temporary change of the current distribution in the nanowire and the load. The mutual interaction between these two responses is combined to form a coupled electro-thermal model [10]. The electro-thermal model helps to understand the transient response of the SSPD after a belt-like normal domain has been formed across the wire due to photon absorption. It provides information about the spatial and temporal evolution of the nanowire temperature profile, the dynamics of the resistive domain in the nanowire, and the self-resetting of the nanowire into the superconducting state. In the following sections, we will describe the electro-thermal model and discuss the simulation results for some examples of SSPDs on GaAs substrate.

2.3.1. Thermal model

In the presented thermal model which follows Ref. [10], it is assumed that the electron and phonon sub-systems are in thermal equilibrium and have a single temperature. This model is a simplified version of a more general two-temperature model described in Ref. [11] to avoid complexity, but is proved to be an acceptable approximation [12]. It is also assumed that there is no temperature variation across the wire cross section and the current density is uniform in the wire. When a small segment of a current-carrying superconducting nanowire becomes resistive, the current that continues to flow through this resistor generates heat due to Joule heating and raises the temperature of the wire in the adjacent segments. As it is shown in Fig. 2.9, the heat generated by Joule heating in the resistive segment of the nanowire flow into the substrate held at bath temperature and along the wire while simultaneously changing the local temperature of the nanowire. If in an adjacent segment, the temperature exceeds the critical temperature of the superconductor, or the current exceeds the critical current at the new temperature, the segment becomes normal. In this way the resistive region grows along the wire. Otherwise, thermal relaxation occurs and the resistive segment cools by heat escaping into the substrate and along the nanowire, causing the normal domain to shrink and disappear. Therefore a temperature profile forms along the nanowire, with the temperature being highest in the middle of the resistive segment.

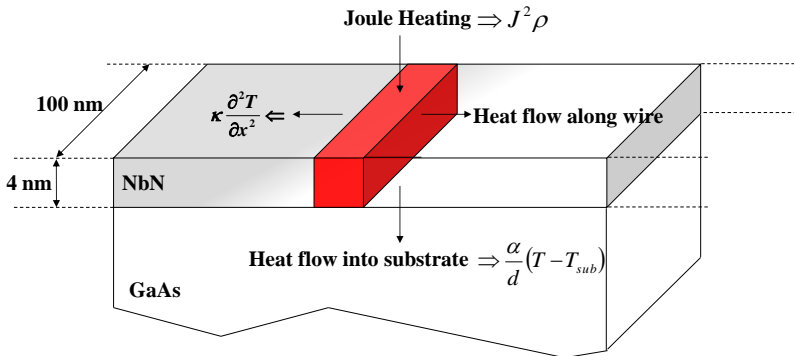


Fig. 2.9 Schematic of the thermal model used in the simulation [10].

The simulation is done using a finite difference numerical method in MATLAB. In this method, the length of the nanowire is discretized into small segments of length Δx , and solved for the temperature profile of each segment at discretized time steps Δt . The initial condition which triggers the photodetection process, is the formation of a resistive barrier which is assumed to be $L_{res} \sim 25$ nm

based on the initial hotspot size [13]. The temperature T of each Δx segment is solved using the following time-dependent one-dimensional heat equation,

$$J^2 \rho + \kappa \frac{\partial^2 T}{\partial x^2} - \frac{\alpha}{d} (T - T_{sub}) = \frac{\partial (cT)}{\partial t}. \quad (2.1)$$

In Eq. (2.1), $T(x,t)$ is the wire temperature, T_{sub} is the substrate temperature, J is the current density through the wire, ρ is the normal state resistivity of the superconducting film, κ is the thermal conductivity of the wire, α is the thermal boundary conductivity between nanowire and substrate, d is the nanowire thickness, and c is the specific heat per unit volume of the wire. The first term of Eq. (2.1), $J^2 \rho$ represents Joule heating and couples the thermal equation to the electrical equations governing the circuit. It relates the heat generation (by Joule heating) and heat dissipation (by thermal conduction along the wire and through the substrate) to the rate of change of energy density in the nanowire.

The challenge in solving the heat equation is that in a superconducting material at cryogenic temperatures, the thermal properties are highly temperature or state dependent, which result in a nonlinear differential equation that has to be solved numerically. For instance, ρ of a region along the wire at temperature T is zero when the current through that region is less than the critical current at that temperature $I_C(T)$. In this simulations, following [10], an expression is used, to calculate $I_C(T)$,

$$I_C(T) = I_C(0) \times \left(1 - \left(\frac{T}{T_C} \right)^2 \right)^2. \quad (2.2)$$

where the critical temperature is typically $T_C \sim 10.5$ K for the 4-nm-thick NbN film and $I_C(0) \sim 24$ μ A for a 100 nm-wide wire. The validity of Eq. (2.2) has been approved from a fit to experimental measurements of I_C over a wide range of temperatures.

A segment is considered resistive, if its current is higher than the critical current at the related temperature $I > I_C(T)$ or its temperature exceeds the critical temperature $T > T_C$, accordingly a constant non-zero value of electrical resistivity ρ , extracted from the I-V curve as described in section (2.2), is assigned to it. This check and assignment is done for each wire segment and at each time step. The total resistance is then calculated as the sum of the resistances of each segment and used in the next step.

Both the electron and phonon specific heat of NbN are considered in this model. The electron specific heat of NbN c_e is considered to be state and temperature dependent. The expression used to calculate the normal-state electron specific heat c_{en} of a resistive wire segment is $c_{en} = \gamma \times T$, where $\gamma = 240$ J/m³K² for thin NbN films [14]. On the other hand, the superconducting electron specific heat c_{es} is determined through the following expression

$c_{es}=Ae^{-\Delta/kT}$ where A is a proportionality constant that is calculated such that $c_{es}(T_C)=2.43 \times c_{en}(T_C)$, and $2\Delta=4.2kT_C$, is the superconducting bandgap of NbN. We calculate $A=2400 \times 2.43 \times e^{4.2/2} \approx 0.5 \times 10^5 \text{ J/m}^3\text{K}^2$. The phonon specific heat c_p is state independent and proportional to T^3 . The specific-heat value is $9800 \text{ J/m}^3\text{K}$ at 10K, obtained from Ref. [14], hence $c_p=9.8T^3$. In conclusion, $c_n=240T+9.8T^3$ in the normal state and $c_s=0.5 \times 10^5 e^{-2.1 \times T_C/T} + 9.8T^3$ in the superconducting state.

The thermal boundary conductivity α between NbN and GaAs substrate determines the rate at which heat is conducted away into the substrate. This parameter has a cubic dependence on temperature, whose value is obtained using the hotspot current following the work of Marsili [3].

The last parameter used in the thermal model is the thermal conductivity of NbN, κ , which is both state and temperature dependent. To calculate the temperature dependence of the normal state thermal conductivity, κ_n , Wiedemann-Franz law must be used ($\kappa=LT/\rho$, where $L=2.45 \times 10^{-8} \text{ W}\Omega/\text{K}^2$ is the Lorenz number and $\rho=3 \mu\Omega\text{m}$ is the electrical resistivity). The superconducting state thermal conductivity, κ_s , is calculated such that $\kappa_s/\kappa_n=T/T_C$, following Ref. [15].

2.3.2. Electrical model

Electrically, the SSPD can be modeled as an inductor in series with a resistor as shown in Fig. 2.10. The inductor L_k represents the kinetic inductance of the superconducting nanowire which is the manifestation of the dissipation-free motion of the superconducting charge carriers [16]. The resistance R_n is the total resistance formed from a number of adjacent segments that switched into the normal state. The DC arm of the bias-T is modeled as a constant-current source and the AC arm is represented by a capacitor $C_{BT}=20 \text{ nF}$. The impedance of the transmission line connecting the device to RF amplifiers is modeled as a load $R_L=50 \Omega$. We solved for the device current I_d through the nanowire using the first equation set in (2.3), as a result of mesh current analysis. It is worthwhile considering that the presence of the capacitor forces the equation set to become of the 2nd order, through a time derivative of all the components, resulting in the second equation set. As the normal resistance of the nanowire is a time-dependent variable, its derivative must not be neglected.

$$\begin{aligned}
 (1): & \begin{cases} L_k \times \frac{dI_1}{dt} + R_n \times (I_1 - I_B) + V_{C_{BT}} + R_L \times I_1 = 0 & \frac{d}{dt} \\ I_d = I_B - I_1 \end{cases} \\
 (2): & \begin{cases} L_k \times \frac{d^2 I_1}{dt^2} + R_n \times \frac{dI_1}{dt} + \frac{dR_n}{dt} \times (I_1 - I_B) + \frac{I_1}{C_{BT}} + R_L \times \frac{dI_1}{dt} = 0 \\ I_d = I_B - I_1 \end{cases}
 \end{aligned} \tag{2.3}$$

Ordinary differential equation (ODE) solver of MATLAB optimization toolbox is used in order to solve the discretized equation set (2.3). This equation is coupled to the thermal equation through R_n . In fact, the thermal model determines the length of the normal region which is proportional to R_n . Finite difference method is used to solve equations (2.1). For each time step, both temperature-and-state dependent parameters are updated and a conditional check is made to determine the new length of the resistive segment. In this check, a segment is considered resistive if I_d exceeds the critical current at the temperature of the segment.

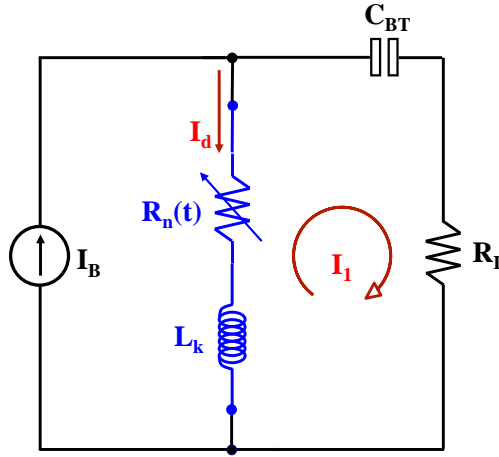


Fig. 2. 10. Schematic of the electrical model used in the simulation.

2.3.3. Results

In SSPDs, the ultrathin NbN nanowire structure, its low specific heat at cryogenic temperatures, and its high thermal boundary conductivity through the substrate, result in a sub-nanosecond heating and cooling procedure. In the rest of this chapter, we consider standard SSPD structures made of $d=4$ nm thick, $w=100$ nm wide NbN nanowires on a GaAs substrate, folded in a meander with $f=40\%$ filling factor to cover a total detection area of $5 \times 5 \mu\text{m}^2$. This corresponds to the total of 1050 squares (total length divided by the width of the wire). The nanowires has critical temperature $T_c=10$ K, and critical current $I_c=22 \mu\text{A}$ at the substrate temperature of $T_{sub}=2$ K, with the kinetic inductance $L_k=90$ pH/ \square . Based on the experimental current-voltage characteristics of a typical NbN SSPD on GaAs [17], the macroscopic thermal properties of a NbN nanowire required for solving the thermal equation are extracted. The normal region resistivity is $\rho=3 \mu\Omega\text{m}$, $\alpha=1.92 \times 10^4$ W/ Ωm at 2 K, and the initial resistive domain length is $L_{res}=25$ nm. Fig. 2.11(a) shows the temperature color-map in space and time for a

photon detection happening in the middle of the nanowire biased at $I_B=0.9 \times I_C$. The quick buildup and collapse in nanowire resistance R_n is shown in Fig. 2.11(b). As shown, the resistance increases to a maximum value of $>1 \text{ k}\Omega$ at $t=80 \text{ ps}$ after which it collapses to zero at $t=160 \text{ ps}$. In Fig. 2.11(c), the device current is shown, with an initial value of $I_B=0.9 \times I_C \approx 20 \text{ }\mu\text{A}$, which starts to sharply drop at $t=0$ with an $L/R=L_k/(R_L+R_n)$ time constant. The device then switches back into the superconducting state at $t=160 \text{ ps}$. At this point the device current is $I \approx 6 \text{ }\mu\text{A}$ when the current slowly increases with an $L/R=L_k/R_L$ time constant. Fig. 2.11(d) plots the calculated output voltage pulse. It is worth to mention about the observed overshoot (undershoot) in the current (voltage) pulses. This is attributed to the discharge of the bias-T capacitance.

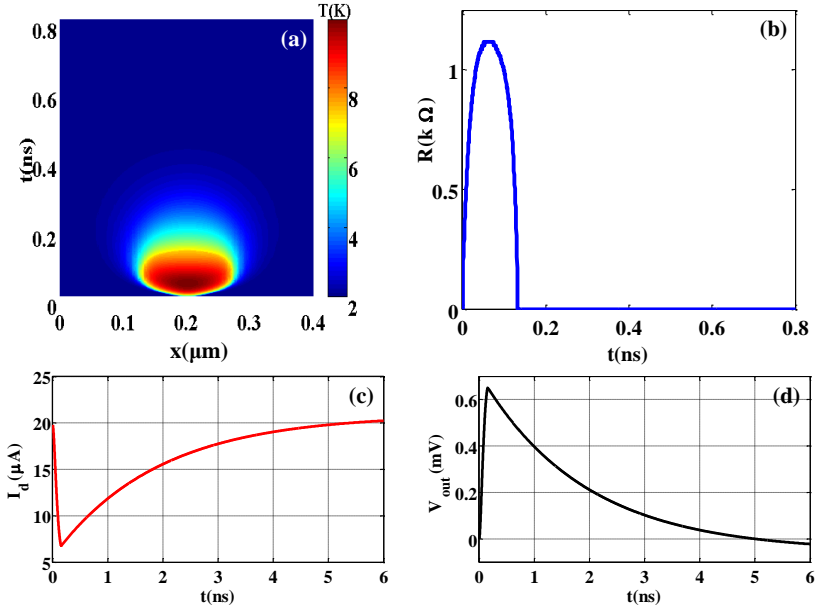


Fig. 2.11. (a) Color-map of calculated temperature at different positions along the wire and in time. (b) Plot of calculated total normal state resistance versus time. (c) Plot of calculated current through an SSPD during a detection event. (d) Plot of calculated voltage pulse. The under-shoot in voltage below 0 V is due to the discharge of the bias-T capacitance.

In fact, during each detection event, when the nanowire becomes resistive and its current is diverted into the load through the bias-T capacitor, a small amount of charge is added to this capacitor, which will be sent back into the detector when it becomes superconducting again. This results in a small, temporary rise in the current through the device, which is not desirable,

especially when the device is biased close to its critical current. The capacitor will fully discharge over $\sim\mu\text{s}$ time-scale, determined by its RC time constant [18]. To illustrate the problem, Fig. 2.12 shows the device current transients at $I_B=0.95\times I_C$. Since the bias current is close to the critical value, the added current δI due to the discharge of the capacitor, results in $I_B+\delta I \geq I_C$ (light green line), which triggers a train of after-pulses in the output voltage (green line, Fig. 2.12 (b)).

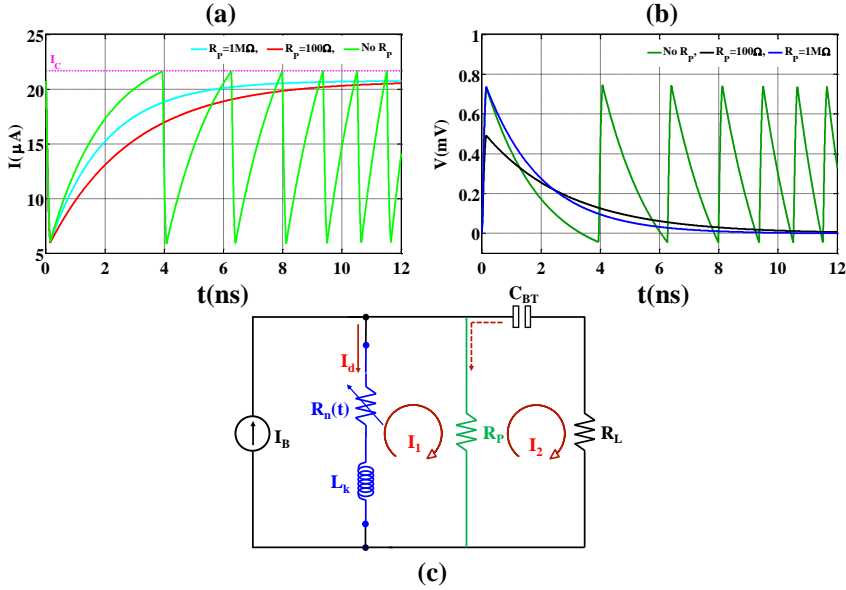


Fig. 2.12. (a), (b) The recovery of the device current and the output voltage transient of a 4 nm thick, 100 nm wide NbN nanowire on GaAs substrate having $f = 40\%$ covering a $5 \times 5 \mu\text{m}^2$ area. The device has $I_C = 22 \mu\text{A}$ at $T = 2 \text{ K}$, and is biased at $I_B = 0.95 \times I_C$. The device cannot function properly at this bias current, due to the effect of the capacitor discharge current. (c) Implementing a parallel resistor (either integrated on-chip, or wire bonded in the vicinity of the device) will avoid the false switching issue.

A possible solution for this problem is to add a route for the discharge of the capacitor. For instance, adding a resistor in parallel to the detector can provide the path for the discharge of the capacitor and ensures the correct performance of the device, without degrading the dynamics of the response. In case of a large resistance, the pulse amplitude is also enhanced. Moreover, the shunt resistor can be used to prevent the latching.

The electro-thermal model introduced in this chapter is fully applied in chapters 4 and 5 to investigate the photon number resolving detectors based on parallel and series configuration, respectively. Especially, in chapter 4, the current redistribution issue and latching are discussed in detail.

References

- [1] “Janis Research Company, Operating Instructions.”
- [2] D. Bitauld et al., “Nanoscale optical detector with single-photon and multiphoton sensitivity,” *Nano letters*, vol. 10, no. 8, pp. 2977-81, Aug. 2010.
- [3] F. Marsili, “Single-photon and photon-number-resolving detectors based on superconducting nanowires,” *PhD thesis*, 2009.
- [4] C. M. Natarajan, M. G. Tanner, and R. H. Hadfield, “Superconducting nanowire single-photon detectors: physics and applications,” *Superconductor Science and Technology*, vol. 063001, 2012.
- [5] R. Radebaugh, “Pulse tube cryocoolers for cooling infrared sensors,” in *Proceedings of SPIE*, 2000.
- [6] Oxford Instruments Nanoscience, “Veri-Cold Operation Manual.”
- [7] S. Miki, M. Takeda, M. Fujiwara, M. Sasaki, and Z. Wang, “Compactly packaged superconducting nanowire single-photon detector with an optical cavity for multichannel system,” *Optics express*, vol. 17, no. 26, pp. 23557-64, Dec. 2009.
- [8] F. Mattioli et al., “Electrical characterization of superconducting single-photon detectors,” *Journal of Applied Physics*, vol. 101, no. 5, p. 054302, 2007.
- [9] G. Dharmadurai and N. S. S. Murthy, “A simplified expression for the minimum hotspot current in long, thin-film superconductors,” *Journal of Low Temperature Physics*, vol. 37, no. 3–4, pp. 269-276, Nov. 1979.
- [10] J. K. W. Yang, A. J. Kerman, E. A. Dauler, V. Anant, K. M. Rosfjord, and K. K. Berggren, “Modeling the electrical and thermal response of

- superconducting nanowire single-photon detectors,” *IEEE Transactions on Applied Superconductivity*, vol. 17, no. 2, pp. 581-585, 2007.
- [11] A. J. Annunziata et al., “Reset dynamics and latching in niobium superconducting nanowire single-photon detectors,” *Journal of Applied Physics*, vol. 108, no. 8, p. 084507, 2010.
- [12] F. Marsili, F. Najafi, C. Herder, and K. K. Berggren, “Electro-thermal simulation of superconducting nanowire avalanche photodetectors,” *Applied Physics Letters*, vol. 98, p. 093507, 2011.
- [13] A. Verevkin et al., “Detection efficiency of large-active-area NbN single-photon superconducting detectors in the ultraviolet to near-infrared range,” *Applied Physics Letters*, vol. 80, no. 25, p. 4687, 2002.
- [14] A. D. Semenov, G. N. Gol’tsman, and A. A. Korneev, “Quantum detection by current carrying superconducting film,” *Physica C*, vol. 351, pp. 349-356, 2001.
- [15] M. Tinkham, J. Free, C. Lau, and N. Markovic, “Hysteretic I-V curves of superconducting nanowires,” *Physical Review B*, vol. 68, no. 13, pp. 1-7, Oct. 2003.
- [16] A. J. Kerman et al., “Kinetic-inductance-limited reset time of superconducting nanowire photon counters,” *Applied Physics Letters*, vol. 88, no. 11, p. 111116, 2006.
- [17] A. Gaggero, S. Jahanmirinejad, F. Marsili, F. Mattioli, R. Leoni, and D. Bitauld, “Nanowire superconducting single-photon detectors on GaAs for integrated quantum photonic applications,” *Applied Physics Letters*, vol. 97, no. 151108, 2010.
- [18] E. A. Dauler et al., “1.25-Gbit/s photon-counting optical communications using a two- element superconducting nanowire single photon detector,” *Proc. of SPIE*, vol. 6372, 2006.

CHAPTER 3

Integration of SSPDs with Optical Microcavities*

As it was introduced in chapter 1, the detection mechanism in superconducting nanowires provides a fast response, with a low dark rate and a low timing jitter, to make SSPDs excellent detectors of choice for many applications especially in the telecom wavelength ranges. For all of the applications, having high quantum efficiency (QE) is greatly desirable. However, as it was mentioned before, optical coupling and absorption are important parameters that put a limit on the QE of SSPDs. Having a ‘meander’ structure improves the coupling efficiency (η_c) from the single-mode fiber to the detector by providing a large enough active area. Further maximizing of η_c is achieved by focusing the input light on the active area of the detector for example with mechanical positioning of the fiber or even fixed alignment of the fiber with respect to the device.

The optical absorption in NbN film with a thickness of only a few nanometers is achieved due to the imaginary part of its dielectric constant. However, the ultrathin and narrow geometry of the nanowire, which makes single-photon detection achievable, puts a limit on the maximum absorbance and hence on the QE of the detector. Aside from the insufficient thickness of the film, the absorption of an incident photon from above the detector is strongly limited by the reflection of the optical signal due to the impedance-mismatch of the incident field to the detector. A promising approach to overcome this problem is to couple the detector resonantly or to a cavity that incorporates the absorbing material [1]. In this chapter, the microcavity detectors incorporating a NbN film on GaAs substrate are investigated. The SSPD is integrated with an optical (half)-cavity based on GaAs/AlAs distributed Bragg reflector (DBR). The GaAs/AlAs Bragg technology provides very high reflectivities >99% and allows the integration of SSPDs with a bottom mirror, and is therefore compatible with the top-illumination, as opposed to the gold mirror approach previously demonstrated. We describe the design procedure and present experimental results of the spectral dependence of the optical absorption and detection efficiency of a fabricated device [2].

* This chapter is published in part in *Applied Physics Letters*, vol. 97, 151108, 2010.

3.1. Optical Absorption Limit

The NbN meander can be compared to a wire-grid polarizer (WGP). WGP is simply a grid of parallel conducting wires (in this case lossy metals) with sub-wavelength spacing, as is shown in Fig. 3.1. If an un-polarized electromagnetic wave impinges on it, it exhibits a preferential absorption of the field component which is parallel to the wires since the electrons along the length of wires are free to move, collide with lattice atoms and convey energy to them. In contrast, the electrons have more restricted movements in the direction perpendicular to the wires and therefore the corresponding field component of the wave is not altered dramatically as it propagates through the grid [3], [4].

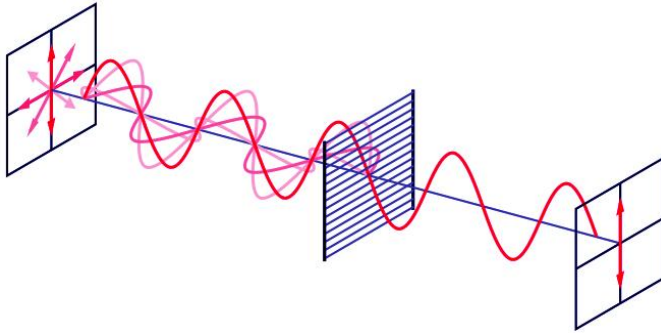


Fig. 3.1. Wire-grid polarizer (from Wikipedia). The transmission axis of the grid is perpendicular to the wires.

Since in most applications the photons impinge on the device with plane wave phase-fronts and a beam spot smaller than the device, the absorption process of photons by an SSPD can be modeled as a plane wave interacting with an infinite grating [5]. A precise estimation for the absorption along the wire can be obtained with the Fresnel equations for an electric field polarized parallel to the wires in a sub-wavelength grating. In this case an effective refractive index is used for the NbN grating $n_{eff} = \sqrt{(1-f) \times n_{air}^2 + f \times n_{NbN}^2}$ where $n_{air} = 1$, $n_{NbN} = 5.23+5.82i$, and f is the fill-factor [5]. A simple effective index model that only depends on f will not work for perpendicular polarization since in this case the absorption depends on both the filling factor and the grating pitch [5]. In our simulation we used $f=0.4$, a value corresponding to the 100nm wire width and 150nm spacing used in our experiments. This resulted in $n_{eff} = 3.35+3.64i$. Using a 1D transfer matrix method, we calculated the reflectance (R), absorptance (A), and transmittance (T) at normal incidence for a 4 nm NbN film on GaAs substrate to be R~30%, A~10%, and T~60%.

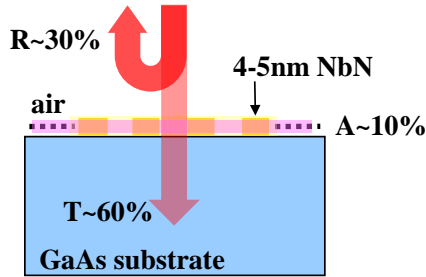


Fig. 3.2. Reflectance (R), Absorbance (A), and Transmittance (T) of a 4nm NbN grating with $f=40\%$ on a GaAs substrate.

If one uses back illumination for the structure, the absorbance reaches 30%, because of the lower reflection at the boundary between GaAs and NbN, assuming that the reflection on the backside of the sample can be eliminated with an anti-reflection coating. In our current measurement setups (Fig. 2.1–2.3) back-illumination is not feasible. Besides, a leftover of an Indium paste at the back side of the sample, remaining from the growth process, makes the device impenetrable to the light from the backside. We note that using top-illumination in the case of other common substrate materials with lower refractive indices, such as Sapphire ($n_{\text{Sapph}}=1.74$) or MgO ($n_{\text{MgO}}=1.71$), will result in an almost twice larger absorbance, but still lower from the desired value.

Here, we show that absorbance can be enhanced by over a factor of 5 by integrating the NbN film with a GaAs/AlAs bottom mirror. Note that the use of GaAs as a substrate poses significant challenges for the SSPD fabrication, which requires the sputtering of high quality ultrathin NbN films and the definition of narrow 100 nm and extremely uniform wires. The main problems are: (1) the mismatch between the substrate and NbN film lattice parameters is higher in the case of GaAs than with the other substrates used so far, (2) the best quality of NbN films is usually obtained with deposition temperatures ($>800^\circ\text{C}$) incompatible with GaAs processing, (3) the relatively high atomic density of GaAs as compared with sapphire or MgO makes high resolution electron beam lithography (EBL) challenging because of the stronger proximity effect. In Ref [2], we have shown how high quality NbN films and nanowire devices can be obtained on GaAs despite the lattice mismatch. A careful optimization of the film deposition and the lithography process, reported in Ref. [2] but not discussed in this thesis, has made the fabrication of these microcavity detectors possible.

3.2. Optical Microcavity

A straightforward solution for the low absorption problem in a thin film is to trap the light and couple it resonantly to the absorbing material. In this way, the

photons have higher chance to get absorbed in the film. Our approach is to integrate the NbN nanowires into a half-cavity structure consisting of a bottom semiconductor mirror. The total microcavity structure is shown in Fig. 3.3 (a). The optical cavity is formed by a DBR on a GaAs substrate (bottom mirror) and a weak top mirror (epitaxial GaAs/air interface). The DBR consists of a stack of alternating $\lambda/4$ -thick layers of high and low refractive index materials, GaAs with $n_{\text{GaAs}}=3.374$ and AlAs with $n_{\text{AlAs}}=2.909$. AlAs is used because of its small lattice mismatch with GaAs and the high refractive index contrast it generates. The high reflectivity at the Bragg frequency is obtained when many small reflections at each interface add up constructively with each other. The optical property of DBRs can be modeled using the transmission matrix approach for a multilayer dielectric structure [6]. The DBR is designed to be resonant at $\lambda=1309$ nm under normal-incidence illumination at 4 K. It consists of 14.5 periods of 112.5 nm AlAs /97 nm GaAs. It is capped by a 194 nm GaAs layer, acting as a $\lambda/2$ spacer between bottom and top mirrors.

Fig. 3.3(b) illustrates the calculated reflectance and transmittance of the DBR structure with the afore-mentioned properties. In this design, the reflectance dip at the Bragg wavelength of $\lambda=1309$ nm has a value of 0.85 for the field without NbN film.

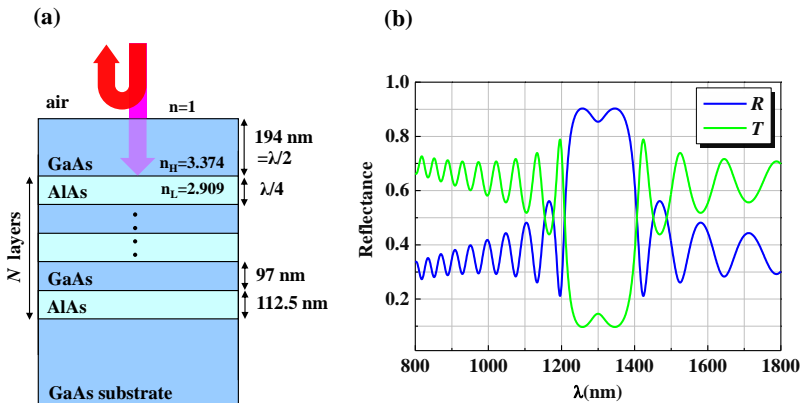


Fig. 3.3 (a) Layer structure of the microcavity with a DBR as the bottom mirror. (b) Reflectance (R) and Transmittance (T) of the designed cavity structure with $N=29$ layers.

In the above calculations, it is assumed that the illumination is at normal incidence. Oblique incidence results in a blue shift of the resonance wavelength. For instance, in an illumination with a radiation angle of $\theta=30^\circ$, the resonance is shifted from $\lambda=1309$ nm to $\lambda=1292$ nm. Since in the real experiment, the light is coupled to the SSPD through an objective lens with a numerical aperture of $\text{NA}=0.5$ ($\theta=30^\circ$), we anticipate that the resonance wavelength will occur around

$\lambda=1300$ nm, and will be spectrally broadened by the angular width of the illumination. Fig. 3.4 compares the reflectivity spectra in the case of normal incidence and illumination with $\theta=30^\circ$.

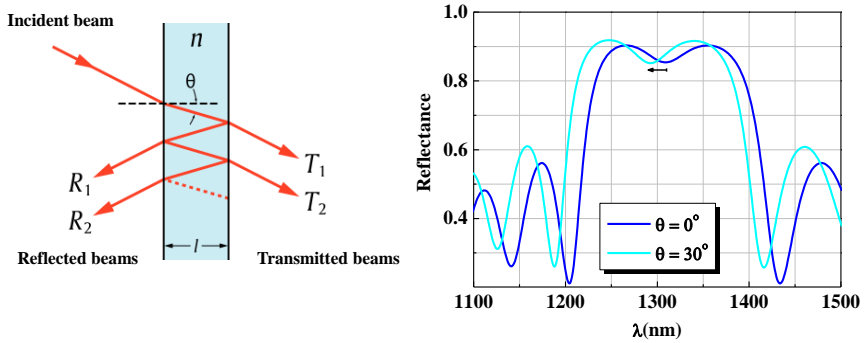


Fig. 3.4 The effect of oblique incidence.

For all of the calculations in this chapter, we neglect the effect of the illumination angle and treated the case as a normal incidence.

3.3. SSPD Integrated with an Optical Microcavity

Fig. 3.5(a) shows the whole detector structure integrated with the optical microcavity. The results of simulations using a 1D transfer matrix model for reflectance, absorptance and transmittance of the device (4 nm-thick NbN grating, with $f=40\%$) are shown in Fig. 3.5(b). A peak absorptance of 83.2% at the Bragg wavelength of $\lambda=1309$ nm is achieved with a 14.5 periods (19 layers), for the polarization parallel to the wires. As it was pointed out before, the meander is considered as a uniform medium with effective dielectric constant between air and NbN. Fig. 3.5(c) depicts the spatial dependence of the normalized modulus square of the electric field, (left axis, red) and the real part of the refractive index, (right axis, blue) of the designed detector. It is clear that the electric field is maximum at the position of the NbN layer. Therefore coupling to the absorbing NbN film is achieved.

It is worth to mention that the cavity structure provides a high absorption in the SSPD, but will limit its spectral bandwidth. However, in some applications such as fiber-based quantum-key distribution (QKD) systems [7] and photon-counting optical fiber communications [8], efficient infrared photon-counters are essential at the minimum dispersion (absorption) window for telecom fibers which occur at the wavelength of 1300 nm (1550 nm).

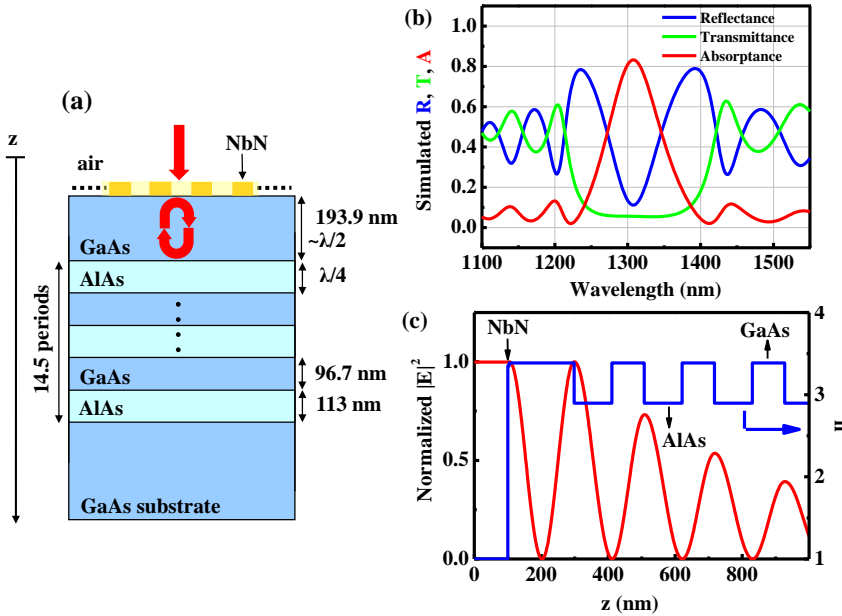


Fig. 3.5. Design of the SSPD integrated with the optical microcavity. (a) Layers structure (b) Simulated reflectance, transmittance, and absorbance, of the SSPD. The peak absorbance reaches $\sim 83\%$ at 1309 nm. (c) Spatial dependence of the normalized modulus square of the electric field, $|E|^2$ (left axis, red) and real part of the refractive index, n (right axis, blue)

3.4. Fabrication of Microcavity Structure

The common technologies to fabricate semiconductor DBR's are molecular beam epitaxy (MBE) and metal organic chemical vapor deposition (MOCVD). In this section, the experimental data concerning DBR structures made on undoped, (100)-oriented GaAs substrate with MBE method are presented. These structures were fabricated at TU/e by Prof. R. Nötzel and G. J. Hamhuis. Epitaxial semiconductor DBR's have good crystal quality and low material absorption; therefore they can reach a very high peak reflectivity. However, they suffer from rather low refractive index contrast, which translates to more pairs of DBRs needed to attain a certain peak reflectivity. In this work the number of pairs was chosen as a compromise between the reflectivity and the ease of growth. An NbN film with thickness of ~ 4 nm was deposited on the epitaxial GaAs top layer by dc reactive magnetron sputtering technique with an Nb target (99.99% pure) in nitrogen ambient. The optimized NbN ultrathin film deposition on GaAs requires lower temperature as compared to the case of sapphire, MgO or Si

substrates due to arsenide evaporation. In our case, the growth temperature is fixed at 350°C. Detailed description of the film growth and wire fabrication can be found in [2]. An SEM image of a fabricated DBR and an AFM image of an NbN meander fabricated on the GaAs substrate are shown in Fig. 3.6 (a) and (b).

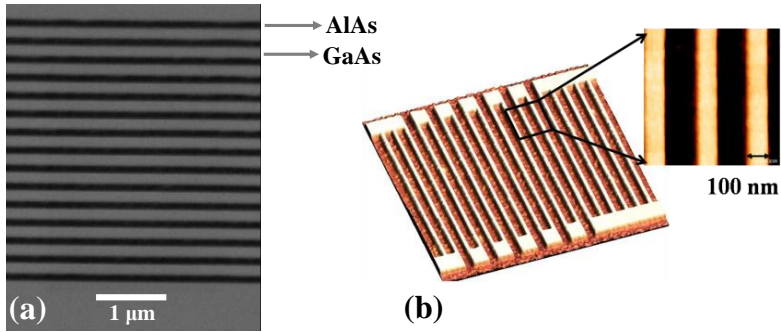


Fig. 3.6. (a) Cross-sectional SEM image of a DBR structure similar to the one used in the detectors. The AlAs and GaAs layers in the DBR are visible as dark and bright layers, respectively. In this image, the thicknesses of the layers do not match the design parameters, due to unoptimized growth rate. (b) AFM image of the NbN meander fabricated on the microcavity structure.

3.5. Experimental Results

In order to assess the performance of the SSPDs on the DBR structures, low-temperature electrical and optical characterizations of the devices were performed. The current-voltage characteristics measured at $T=4.2$ K with a dipstick in liquid helium show a typical critical current of $I_c=16.4 \mu\text{A}$ (Fig. 3.7 (a)) and the fast photoresponse shows a FWHM of ~ 2 ns (Fig. 3.7(b)).

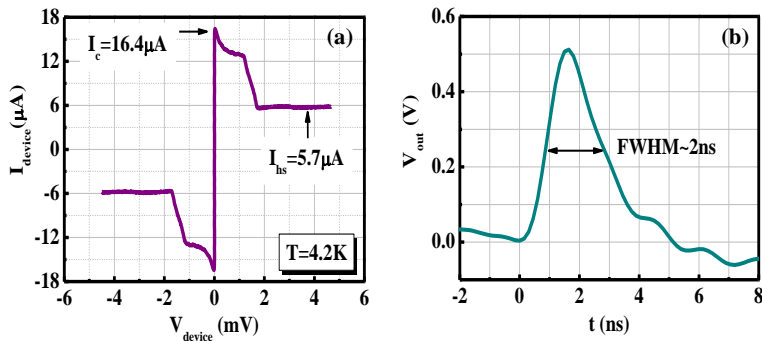


Fig. 3.7. (a) I-V characteristics of the fabricated SSPD (b) Amplified photoresponse of the SSPD recorded with 4GHz oscilloscope.

The reflection measurements were performed in a standard micro-photoluminescence (μ -PL) setup at $T=5$ K, where the polarized white light was focused on the sample with a microscope objective (numerical aperture $NA=0.5$). The reflected light was collected through the same microscope objective, then dispersed by a spectrometer and detected by a CCD (Charge Coupled Device) camera. A schematic of the setup is illustrated in Fig. 3.8. The measured spectra are normalized to the reflectivity of a gold mirror measured in the same condition to represent the reference.

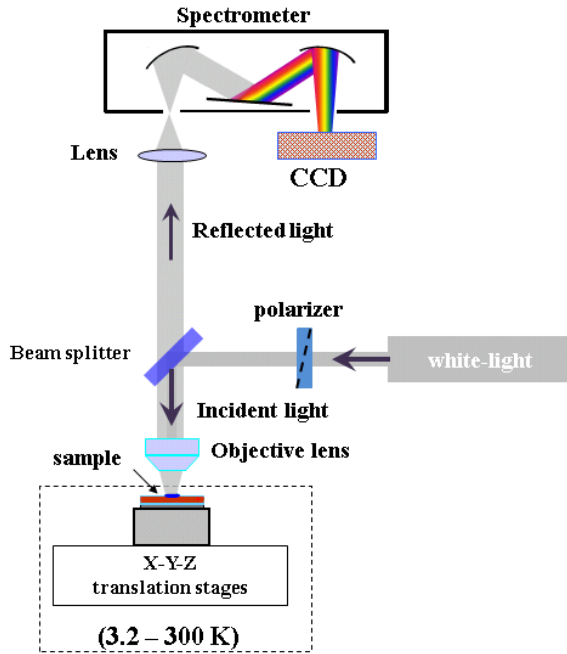


Fig. 3.8. μ -PL setup used to measure reflectivity.

Fig. 3.9 shows the measured reflection spectra of the cavity structure with and without the patterned NbN nanowire on top. The DBR reflection band extends from 1200 nm to 1370 nm, with a small dip around 1300 nm when no NbN film is present (dark blue line, left axis). Upon deposition and patterning of the NbN thin film, the dip becomes much more pronounced (dark green line, left axis) which is the evidence of the optical absorption in the NbN wires. However we observe a rather skewed shape of the measured reflection spectra with respect to what we expect from the simulations. We attribute this to the deviation in the thicknesses and/or indices of the GaAs and AlAs layers as compared to the design values. The blue (green) symbols in Fig. 3.9(a) are fits to the measured

reflectance of the DBR (SSPD) by considering 5% thicker GaAs layers and 8% thinner AlAs layer (light blue open circles, left axis). The fit matches the data in the passband very well. The experimental reflectivity spectrum over the wide range shown in Fig. 3.9 is affected by the dispersion in the refractive index, which is not taken into account in the simulation. We will use the result of the fit for the next fabrication process.

To achieve the nice fit to the measured reflection spectrum of the SSPD, the effective refractive index of NbN was required to be changed to a lower value than the value taken from Ref. [5], which had become used in the design (Fig. 3.5). This is conceivable since the refractive index depends on the device thickness, temperature, the wavelength of the incident light and probably the substrate. The measurement of NbN refractive index in [5] was made at room temperature by using spectroscopic ellipsometry on a 12 nm-thick NbN film deposited on a sapphire wafer. In Fig. 3.10, in order to get the best fit to the SSPD reflectance, (light green open squares, left axis) $n_{\text{NbN}}=3.4+4i$ at 1300 nm was assumed. As a result, based on the measured reflectance of DBR and SSPD, the absorption spectrum of the NbN is simulated (Fig. 3.9 red line, left axis) which reveals that $\sim 50\%$ absorptance can be achieved. The cavity design may be improved by adding a top dielectric DBR to further increase the absorption in the film.

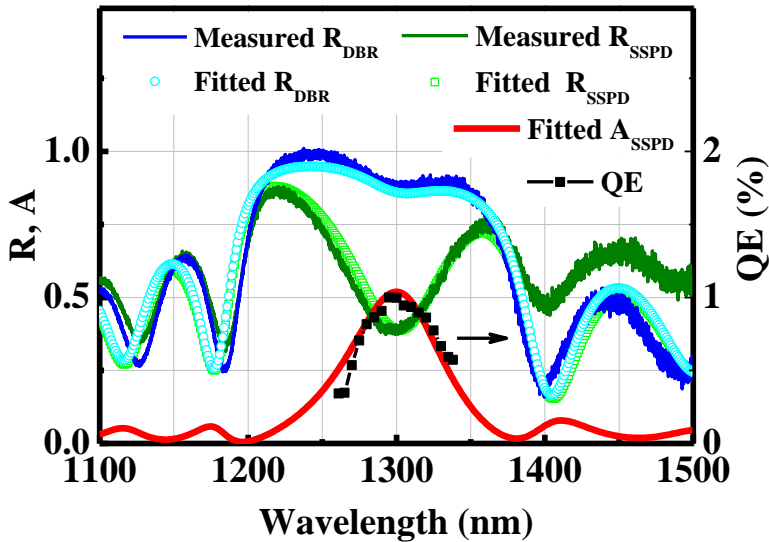


Fig. 3.9. (Left axis): measured and fitted reflectance of the DBR structure and the SSPD, together with the corresponding simulated absorption spectrum of the SSPD. (Right axis): Experimental detection efficiency vs. wavelength for an SSPD on DBR, using a tunable laser at $I_B=13 \mu\text{A}$.

The quantum efficiency of the device is shown (in arbitrary units) vs. wavelength in Fig. 3.9 (black symbols, right axis), as measured using a tunable laser in the cryogenic probe station, with a device temperature $T=5-6$ K and a bias current $I_B=13$ μ A. A clear resonance is observed in the device QE, centered at $\lambda\sim 1300$ nm, which corresponds very well to the absorption spectrum of the device. The polarization was controlled to maximize the number of detector counts, corresponding to an electric field parallel to the nanowires. Fig. 3.10 shows the device QE and dark count rate (DCR) for the same device in the dipstick at $T=4.2$ K under illumination at $\lambda=1300$ nm. The usual increase of both device QE and DCR vs. bias current is observed, with a maximum device QE=18.3 % at $I_B=0.99\times I_C$. The fact that the peak device QE is lower than the expected absorbance of 50% is attributed to the limited intrinsic efficiency of the device [9]. Lower measurement temperatures and further fine tuning of the film thickness and deposition conditions may enable reaching the absorption-limited device QE value.

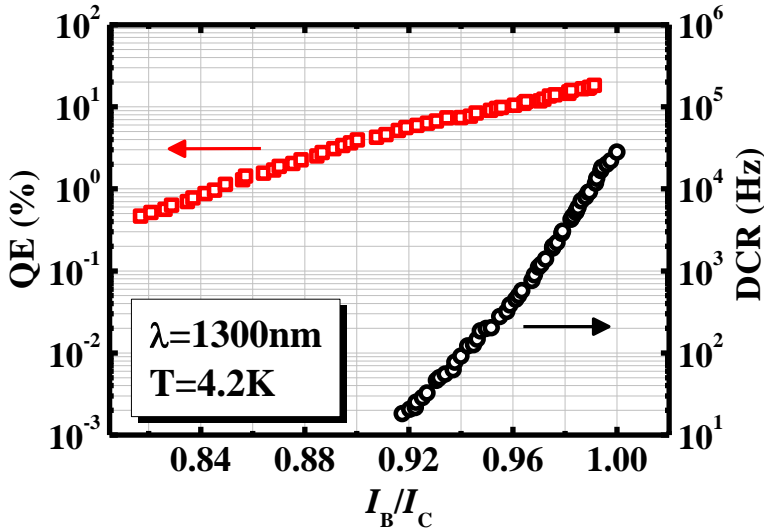


Fig. 3.10. Device quantum efficiency measured at $\lambda=1300$ nm (red squares, left axis) and dark count rate (black circles, right axis) at $T=4.2$ K as a function of the normalized bias current for the same device as in Fig. 3.9.

3.6. Conclusion

In conclusion, we presented the design, fabrication and characterization of SSPDs on microcavity structures. Microcavity SSPDs using different technologies have also been reported by other groups [10–12] in parallel with our

work, and very recently a system QE~93% has been reported [13] as an effort to employ the microcavity approach to achieve ~100% efficiency. However, in these structures the increase in QE comes at the expense of the reduced optical bandwidth. An alternative approach is represented by integration of waveguides, which was demonstrated both in our group [14] and in [15], but is not discussed in this thesis. The continuous, evanescent coupling and the confinement of the waveguide mode allow potential for extended interaction regions, providing a way to increase efficiency without limiting the detector acceptance bandwidth.

References

- [1] K. M. Rosfjord et al., “Nanowire single-photon detector with an integrated optical cavity and anti-reflection coating,” *Optics express*, vol. 14, no. 2, pp. 527-534, 2006.
- [2] A. Gaggero, S. Jahanmirinejad, F. Marsili, F. Mattioli, R. Leoni, and D. Bitauld, “Nanowire superconducting single-photon detectors on GaAs for integrated quantum photonic applications,” *Applied Physics Letters*, vol. 97, no. 151108, 2010.
- [3] E. Hecht, *Optics*, 4th ed. Addison-Wesley, 2002.
- [4] E. F. C. Driessen, F. R. Braakman, E. M. Reiger, S. N. Dorenbos, V. Zwiller, and M. J. a. de Dood, “Impedance model for the polarization-dependent optical absorption of superconducting single-photon detectors,” *The European Physical Journal Applied Physics*, vol. 47, no. 1, p. 10701, May 2009.
- [5] V. Anant, A. J. Kerman, E. A. Dauler, K. W. Joel, K. M. Rosfjord, and K. K. Berggren, “Optical properties of superconducting nanowire single-photon detectors,” *Optics express*, vol. 16, no. 14, pp. 46-52, 2008.
- [6] S. J. Orfanidis, *Electromagnetic Waves and Antennas*. 2008.
- [7] H. Takesue, S. W. Nam, Q. Zhang, R. H. Hadfield, K. T. Toshimori Honjo, and Y. Yamamoto, “Quantum key distribution over a 40-dB channel loss using superconducting single-photon detectors,” *Nature Photonics*, vol. 1, pp. 343 - 348, 2007.

- [8] B. S. Robinson et al., “781 Mbit/s photon-counting optical communications using a superconducting nanowire detector.,” *Optics Letters*, vol. 31, no. 4, pp. 444-6, Feb. 2006.
- [9] A. Semenov et al., “Intrinsic quantum efficiency and electro-thermal model of a superconducting nanowire single-photon detector,” *Journal of Modern Optics*, vol. 56, no. 2–3, pp. 345-351, Jan. 2009.
- [10] M. G. Tanner et al., “Enhanced telecom wavelength single-photon detection with NbTiN superconducting nanowires on oxidized silicon,” *Applied Physics Letters*, vol. 96, no. 22, p. 221109, 2010.
- [11] B. Baek, J. A. Stern, and S. W. Nam, “Superconducting nanowire single-photon detector in an optical cavity for front-side illumination,” *Applied Physics Letters*, vol. 95, no. 2009, p. 191110, 2011.
- [12] F. Marsili et al., “Cavity-integrated ultra-narrow superconducting nanowire single-photon detector based on a thick niobium nitride film,” *Proceedings of OSA, Quantum Electronics and Laser Science Conference*, vol. 1, pp. 12-13, 2012.
- [13] F. Marsili et al., “Detecting single infrared photons with 93 % system efficiency,” *arXiv:1209.5774*, 2012.
- [14] J. P. Sprengers et al., “Waveguide superconducting single-photon detectors for integrated quantum photonic circuits,” *Applied Physics Letters*, vol. 99, no. 18, p. 181110, 2011.
- [15] W. H. P. Pernice, C. Schuck, O. Minaeva, M. Li, G. N. Goltsman, and A. V. Sergienko, “High speed and high efficiency travelling wave single-photon detectors embedded in nanophotonic circuits,” *arXiv:1108.5299v2*, pp. 1-23, 2012.

CHAPTER 4

Parallel Nanowire Detectors

The detector structure introduced in this thesis so far, has a standard meander configuration, where the two ends of one NbN nanowire are connected to the signal and the ground conductors of a coplanar transmission line which is used both to DC bias and to transmit the RF signal of the detector. In this detector geometry, absorption of a photon generates a temporary hotspot, whose resistance typically grows to hundreds of ohm. In this case, the current division is in favor of the $50\ \Omega$ -readout circuit and most of the bias current is temporarily diverted to the load. As long as the resistance of the normal domain is much larger than the load resistance, absorption of more than one photon at the same time in the wire cannot dramatically change the amount of current directed to the load. For this reason, the SSPDs with the standard structure are not considered as “photon-number-resolving” (PNR) detectors. However, as it was discussed in chapter 1, the ability to resolve the simultaneous photons on the device is highly valuable for many applications.

Temporal or spatial multiplexing techniques are straightforward solutions to surmount this issue and provide the ability to resolve the number of photons in an optical pulse. Time-multiplexing method is reported in [1], and depicted schematically in Fig. 4.1(a). It is achieved by splitting of the incident optical pulse into N temporal modes separated by a time interval of Δt using a series of delay lines and fiber couplers, and employing two single-photon detectors to measure the number of incident photons. However, this technique has not been applied to SSPDs, as it necessarily increases the response time and introduces additional loss due to the fiber couplers.

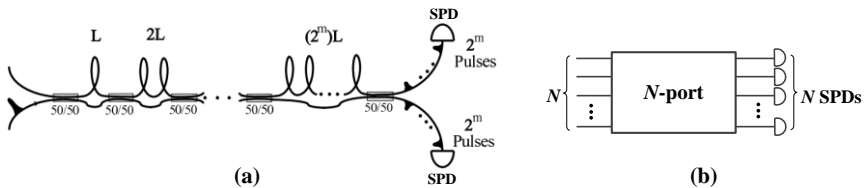


Fig. 4.1. (a) Schematics of the time-multiplexing technique from [3] with 50/50, symmetric fiber couplers. (b) Schematics of the spatial-multiplexing detection.

In the spatial-multiplexing technique as depicted in Fig. 4.1(b), an incoming beam is distributed evenly into N output modes (N -port), which are all detected with N single-photon sensitivity detectors. In this method, it is ideal to choose the number of output modes large enough, so that the probability that two photons enter the same detector becomes small. However, the required cables and amplifiers scale with the number of the detectors in the array. This brings about complexity into the read-out system in case of large N . Nevertheless, this technique has been applied to SSPDs and arrays of four-element SSPDs have been demonstrated [2].

The parallel nanowire detector (PND), which was introduced shortly before the beginning of this thesis by Divochiy *et al.* [4], is a photon number resolving (PNR) detector that uses spatial multiplexing on a sub-wavelength scale in which an electrical output signal proportional to the photon number is achieved through only one readout line, avoiding complexity of the read-out from separate detector channels. In this chapter, first a review of working principle, fabrication, and previous experimental results of the PND are presented. Then, an extensive analysis of the device dynamics is provided through the electro-thermal model to investigate the limitations of this structure.

4.1. Structure and Working Principle of PNDs

Invention of the parallel nanowire detector was a major breakthrough for photon number discriminating detectors demonstrated in 2008 [4]. The basic structure of this detector is the parallel connection of N similar superconducting nanowires, each connected in series to a resistor R_s (Fig. 4.2(a)). Each single-photon detecting element is a 4–5 nm-thick, 100 nm-wide NbN nanowire folded in a meander pattern to be sensitive to the energy of a single photon. If a superconducting nanowire is biased close to its critical current, the absorption of a photon causes the formation of a normal barrier across its cross section and the bias current is pushed to the external circuit. When n photons impinge on distinct sections of an N -PND biased at a current $N \times I_B$ simultaneously (in an interval shorter than the current recovery time), they will cause the creation of normal barriers across the entire cross section of the nanowires (ideally with the same probability)*. Because of the sudden increase in the resistance of the firing nanowires, their currents are then redistributed between the less resistive paths in the circuit, including the $R_L=50 \Omega$ input resistance of the high frequency amplifier and the other $N-n$ unfiring branches. In fact, to have a proper PNR behavior, it is desirable that the portion of the currents leaking through the unfiring sections remain much smaller than the current flowing through the load.

* In the following, we will address the branches that have absorbed photons as “firing” sections and those which did not absorb any photon as “unfiring” sections.

For this reason a series resistor has been added to each section to build a larger impedance in the section and limiting the “leakage current”. In this case, most of the current from the firing sections can sum up on the external load, finally producing an output voltage pulse proportional to the number of firing sections (Fig. 4.2(b)). In particular, when the PND consists of a large number of parallel sections, even small leakage currents from the firing sections can drive the unfiring sections normal, if they are biased very close to their I_C . This problem is visualized later in this chapter.

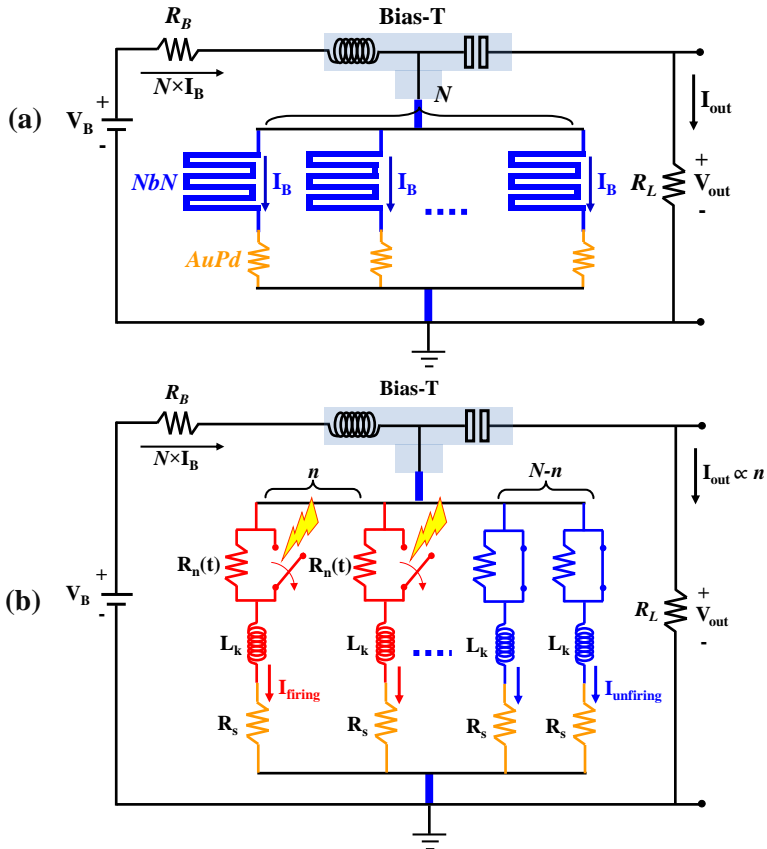


Fig. 4.2. (a) Schematics of the PND structure with N elements in parallel. (b) The n firing branches and $N-n$ unfiring branches. It is desired that the output current I_{out} be proportional to the number of firing elements, n .

To get a PND to work properly, the number of parallel sections must be large as compared to the maximum number of incident photons. This can be seen as analogous to the problem that n identical balls (photons) fall into N identical

boxes (pixels) such that there is never more than 1 ball in any given box. In this case, if $n \ll N$, two incoming photons have a negligible chance of getting absorbed in the same section.

The first PNDs were fabricated on ultrathin NbN films (4 nm) on MgO substrate using electron-beam lithography and reactive-ion etching. Detectors of $10 \times 10 \mu\text{m}^2$ area, nanowire width of 100 nm and a fill factor of 40%, with the number of parallel branches varying from 4 to 6 were fabricated [5]. Three nanolithography steps needed to fabricate the structure were carried out by using a field-emission gun electron-beam lithography system (acceleration voltage 100 kV). In the first step, pads and alignment markers (60 nm gold on 10 nm titanium) were fabricated by lift-off using a polymethyl methacrylate (PMMA) stencil mask. In the second step, a hydrogen silsesquioxane (HSQ) mask was defined to produce the meander pattern. All the material not covered by the HSQ mask and the Ti/Au film, was removed by using fluorine-based reactive-ion etching. Finally, with the third step the bias resistors (85 nm AuPd alloy) aligned with the two previous layers were fabricated by liftoff using a PMMA stencil mask. A scanning electron microscope image of a PND with six parallel wires (6-PND) and series resistors fabricated on MgO substrate is shown in Fig. 4.3(a).

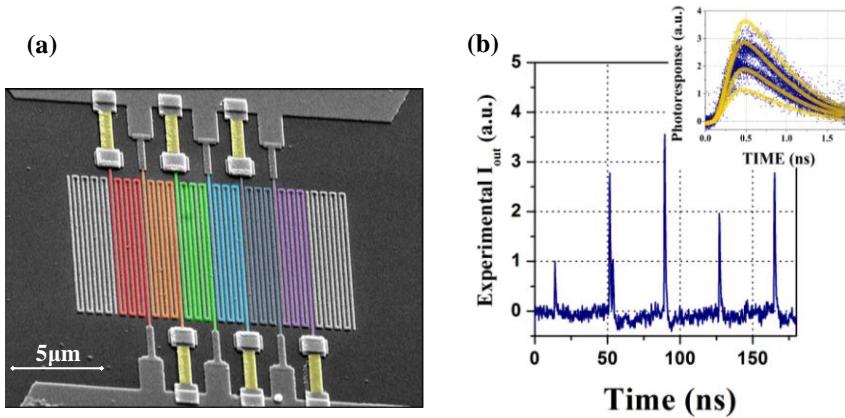


Fig. 4.3 (a) Scanning electron microscope (SEM) image of a 6-element PND fabricated on a 4 nm thick NbN film on MgO. The active nanowires (in color) of the PND are connected in series with AuPd bias resistors (in yellow). The floating meanders at the two edges of the PND-R pixel are included to correct for the proximity effect. (b) Single-shot oscilloscope trace of a 4-PND structure. Inset: Oscilloscope persistence graph taken with a 40 GHz sampling oscilloscope. The yellow solid curves are guides to the eye. The figures are taken from [4].

Fig. 4.3(b) shows the single-shot oscilloscope trace of a 4-PND probed with light at $\lambda=1.3 \mu\text{m}$ in the probe station. The signal amplitudes of four different levels correspond to the 1, 2, 3 and 4 photon detection events. The photoresponse recorded by a sampling oscilloscope is shown in the inset of Fig. 4.3(b). All four possible amplitudes can be observed. The pulses show a full-width at half-maximum of 660 ps. The PNDs showed counting performance when probed with light at repetition rate of 80 MHz, outperforming most of the existing PNR detector at telecom wavelength ranges. Indeed, PNDs have by design a reduced recovery time compared with traditional SSPDs, owing to their reduced kinetic inductance. A detailed study of the physics and application of PNDs was given in Ref. [5] at the beginning of this thesis. In the next sections of this chapter, the simulations based on the electro-thermal model are used to further understand the response behavior and to figure out the limitations of these structures.

4.2. Electro-Thermal Simulation

In this section the electro-thermal model developed for NbN PNDs on GaAs substrate is introduced. The model parameters are extracted from a typical I-V curve of an SSPD on GaAs substrate (see chapter 2). The thermal model is the same as the one used for a standard SSPD and the only difficulty is the electrical model with the number of variables scaling up with the number of parallel sectors. However, using an equivalent circuit model (Fig. 4.4) consisting of one branch for all firing and one branch for all unfiring wires, allows us without loss of generality, to reduce the unknowns in the equation systems to two.

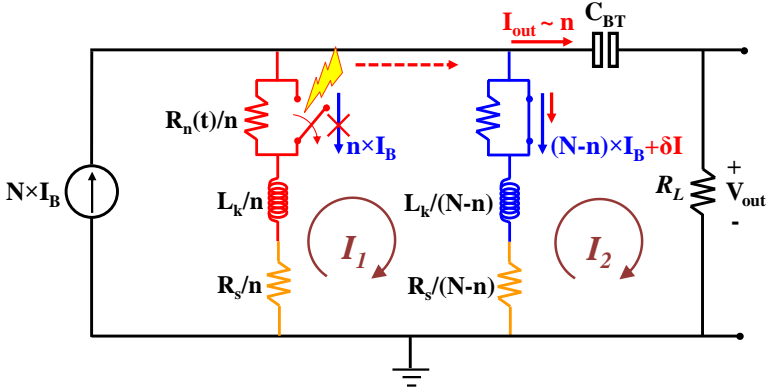


Fig. 4.4. Equivalent electrical circuit of an N -PND used to reduce the number of unknowns. The equivalent of the firing and unfiring nanowires are in red and blue, respectively. $R_L = 50 \Omega$ models the input impedance of the RF amplifier in the read-out electronics. The current-mesh analysis is. The circuit system to be solved is of the 2nd order.

The use of this equivalent circuit is justified by the fact that by symmetry, the current in all (un)firing branches must be the same. For instance, we can solve for the currents I_1 and I_2 in Fig. 4.4 (and consequently the currents in the firing and unfiring sections) using mesh-current analysis.

Using the electro-thermal model and equivalent circuit analysis, the output voltage pulses of a 4-PND out of 4 nm thin, 100 nm wide NbN nanowires of 40% fill factor covering an area of $12 \times 12 \mu\text{m}^2$ area on GaAs substrate, are simulated. The substrate temperature is supposed to be $T=2$ K. The critical current and temperature are assumed to be $I_C=18 \mu\text{A}$ (at 2K) and $T_C=10.5$ K.

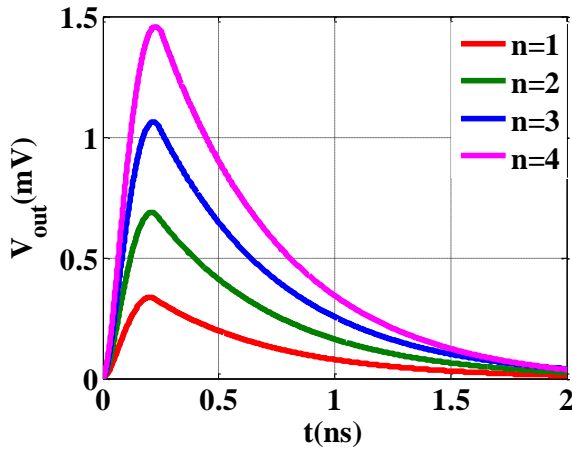


Fig. 4.5. The transient output voltage pulse for the 4-PND indicating a linear response to $n=1, 2, 3$ and 4 photon detection events.

4.3. Current Redistribution Problem

While the equivalent circuit model can be simply applied to reduce the number of equations in the electrical model, to address the “current-redistribution” problem in this section, the electrical and thermal model equations are solved separately for each section. In this way, the interaction of the sections and the possible false switching of a section without absorbing any photon can be easily observed. When the bias current is rather far from the critical value, the device shows a normal PNR behavior, where absorption of $n=1, 2, 3,$ and 4 photons in distinct sections generate pulses of proportional amplitudes. This means that after each detection event, the added leakage currents to the still superconducting wires are small, keeping the bias current of each section still below its critical current. An example of this “normal” behavior is illustrated in Fig. 4.6 (a–d) and Fig. 4.7(a, b) which concern the 4-PND with series resistance of $R_S=50 \Omega$ and bias current of $I_B=0.78 \times I_C$ in each detecting

element. Fig. 4.6(a) and (b) show the temperature and the normal region maps for one element which absorbed the photon (firing). The normal domain grows and shrinks in a fraction of nanosecond to generate a voltage pulse. Fig. 4.6 (c) and (d) show the corresponding maps for an element which did not receive any photon, and as desired, does not experience any change in its temperature and remains superconducting.

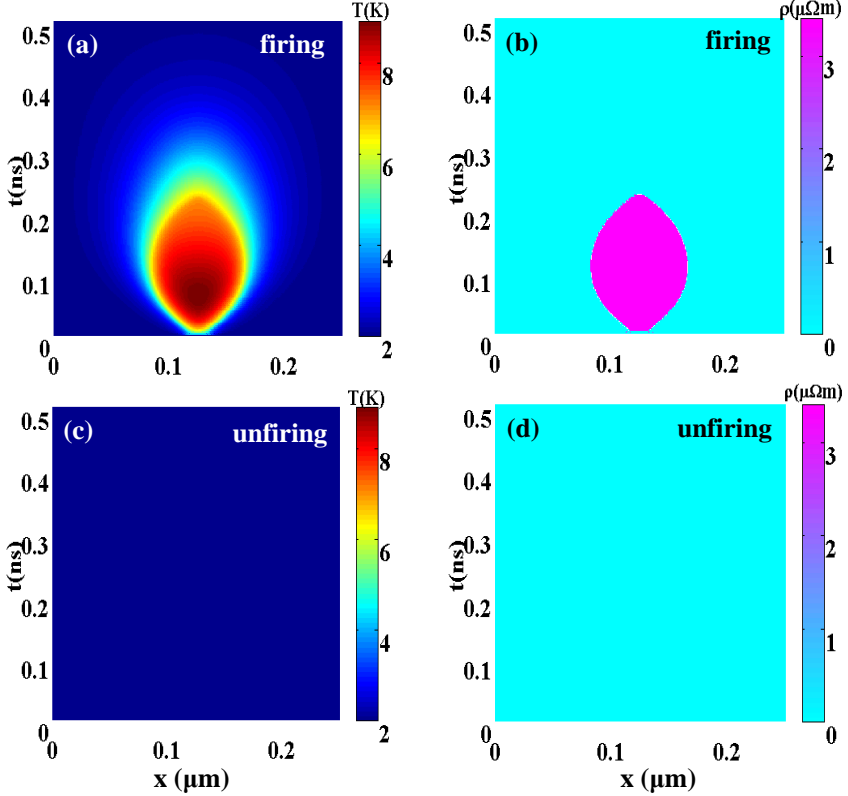


Fig. 4.6. (a),(c) Temperature map and (b),(d) normal domain map corresponding to the 1-photon absorption event in a 4-PND with $R_S=50 \Omega$, biased at $0.78 \times I_c$ in a firing and unfiring section respectively.

Fig. 4.7(a) and (b) show the temporary resistance which develops along the firing section and the corresponding current change that occurs in the circuit. Most of the current of the firing branch is diverted to the load, while the leakage currents to the unfiring sections remain small, preventing any spurious switching of them.

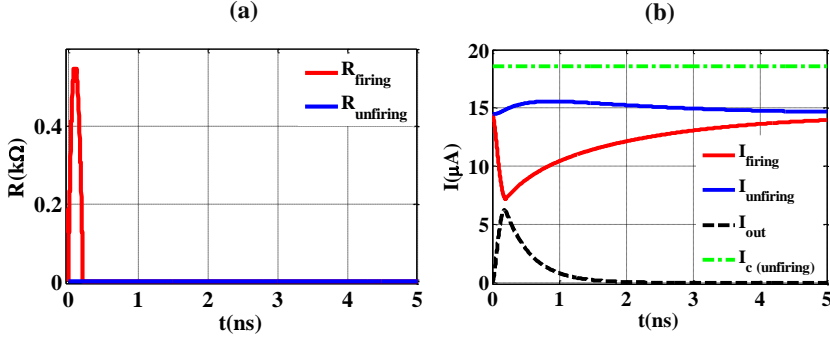


Fig. 4.7. (a) The developed resistance and (b) the current dynamics corresponding to the 1-photon detection event in a 4-PND biased at $0.78 \times I_C$ in a firing section (red), unfiring section (blue) and in the load (black). The dash-dotted line shows I_C at the base temperature of 2 K.

In the SSPDs with typical wire widths of ~ 100 nm, and at telecom wavelength range, the QE has a strong dependency on the bias current. Therefore, to achieve high efficiency, increasing the bias current is inevitable. However, according to the electro-thermal simulation, increasing the bias current of a PND above a certain value, results in large leakage currents which lead to the unwanted switching of the superconducting wires which did not receive any photon, since they exceed their I_C [6]. For instance, in the previous example, increasing the bias current to $I_B = 0.92 \times I_C$ results in having false counts. This issue is illustrated in detail in Fig. 4.8(a)–(f). First note Fig. 4.8 (a) and (b) which show the evolution of the temperature and the normal domain in time and space for a wire which is supposed to be “unfiring”, i.e. did not receive any photon. Since the time origin $t=0$ indicates the time when a photon was absorbed in a “firing” branch, it can be seen that ~ 300 ps after the photon absorption in the initiating wire, hotspots are nucleated in the other identical wires, disturbing their superconductivity, as if photons had been absorbed. Similar to the initiating wire, “secondary” hotspots also grow and shrink due to the Joule heating and thermal dissipations. While the normal regions are growing in the unfiring branches, their currents mostly flow to the 50Ω load, but there will be also leakage currents going to the initially firing wire. This leakage current makes the current of the initial section, which is recovering to its steady state value, increase over I_C , and as a result another normal region is nucleated. In Fig. 4.8(e) and (f), the red curves correspond to the normal domain and current transient in the initially firing section, while the blue curves correspond to the unfiring sections. The simulation has been stopped at $t=1$ ns, but this loop is repeatedly running and generates a train of pulses until the bias current is decreased to a lower value. In Fig. 4.9, the corresponding output voltage is shown.

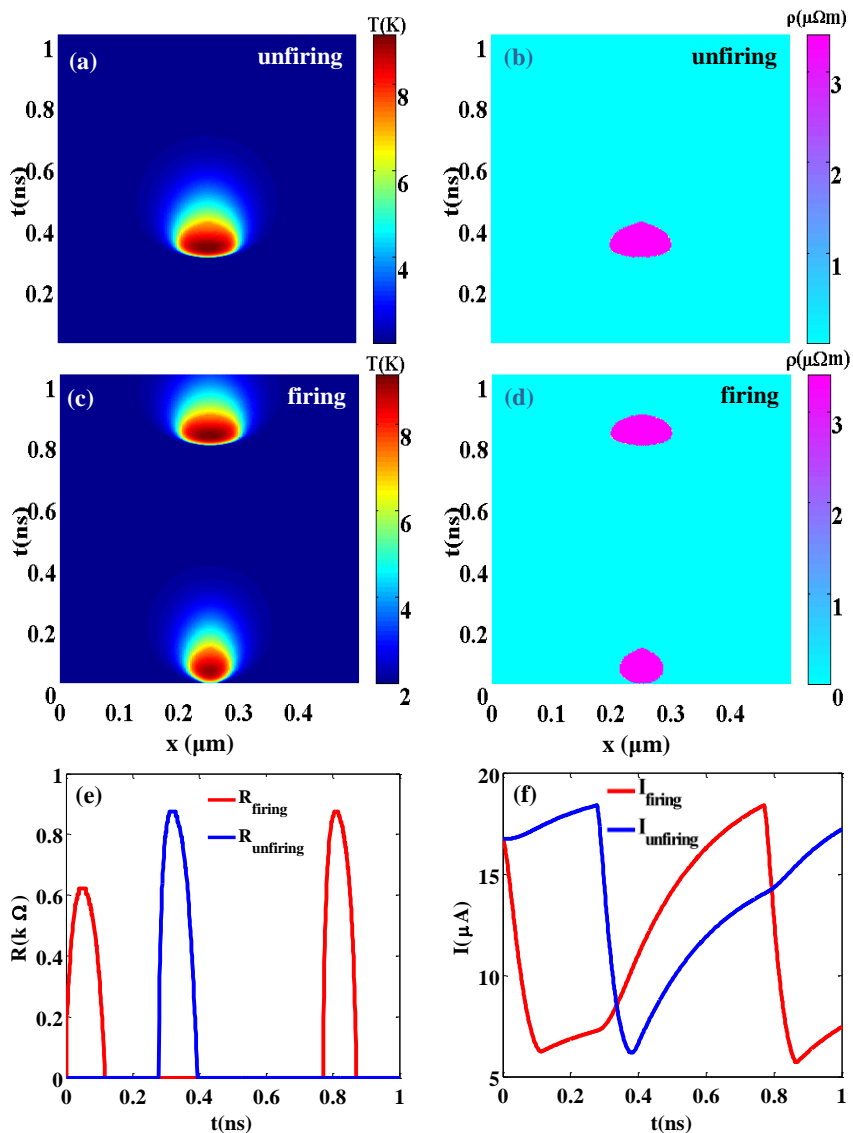


Fig. 4.8. Cascade switching of the PND sections at high bias currents due to current re-distribution problem. (a),(c) Temperature map and (b),(d) normal domain map corresponding to the 1-photon absorption event in a 4-PND, biased at $0.92 \times I_c$ in an unfiring and firing section, respectively. (e) The developed normal domain and (f) the current regarding the firing (red) and unfiring (blue) section.

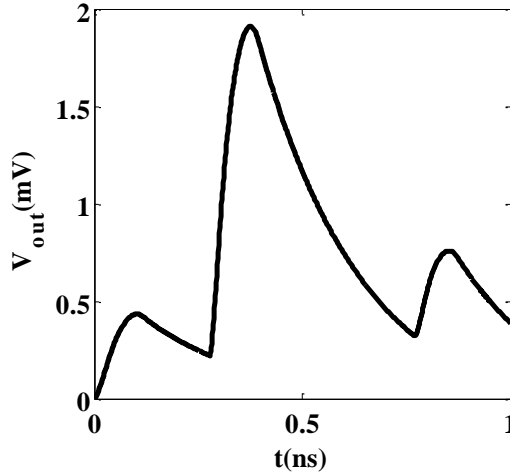


Fig. 4.9. The oscillating output voltage showing afterpulse events in a 4-PND with $R_S=50 \Omega$, biased at $0.92 \times I_C$.

When more wires fire in a PND, a smaller leakage current is needed to trigger the cascade switching [6] of the rest of superconducting wires, therefore detecting large photon numbers with a PND is more challenging. In other words, the threshold current in which the cascade switching occurs gets smaller when the number of detecting elements increases. This means that detecting n photons in an N -PND is less likely when n approaches N .

4.4. Latching Problem

As it was clear in the previous sections, increasing the bias current above a threshold value in the 4-PND structure under investigation, created a closed-loop oscillating output. To overcome this problem, we can think of further decreasing the leakage current by increasing the impedance of each element, i.e. increasing the series resistance R_S . However, this results in a smaller L/R time constant and a rather faster recovery of each element after switching to normal, even sooner than its current is depleted to the load or other branches. This generates a positive feedback and leaves the wire in a stable normal domain, a phenomenon known as latching [7], also discussed in chapter 1. Illustrated in Fig. 4.10 is the simulation for the case of $n=1$ photon detection level in the 4-PND biased at $I_B=0.95 \times I_C$ with a series resistance of $R_S=200 \Omega$ in each section. The normal region in the firing wire cannot get healed after a stable resistive region has formed in the nanowire, since the electrical response has become faster than the thermal response of the nanowires. As a result a stable normal region is also formed in all other branches

of the PND, where a stable current of $\sim 10 \mu\text{A}$ flows in each of the branches. This will continue until the bias current is decreased and the nanowires come back to the superconducting state again.

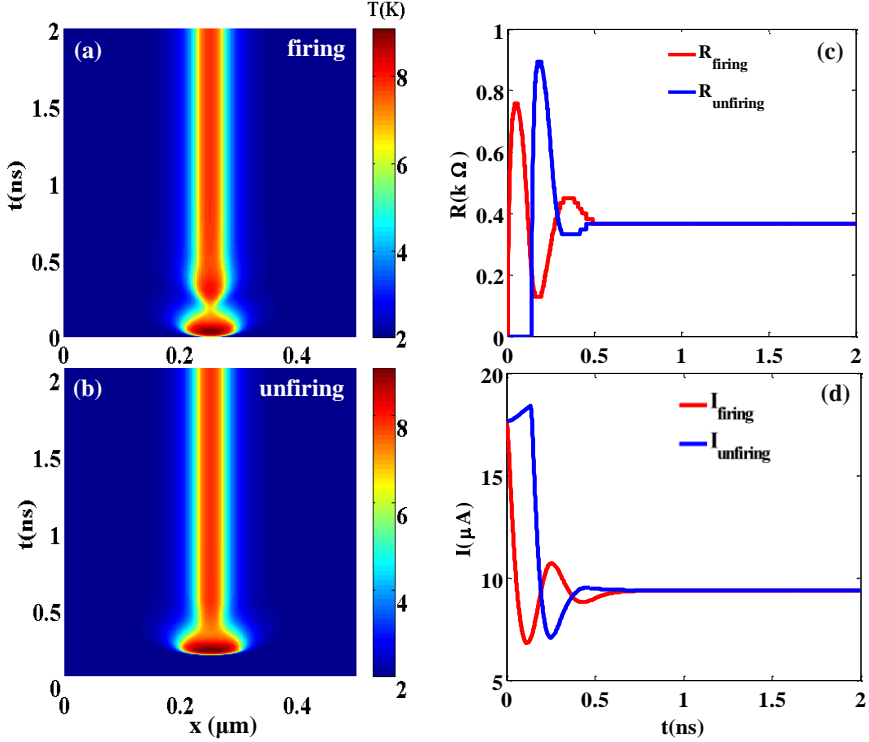


Fig. 4.10. Latching occurs when R_S is increased to 200Ω as a solution to decrease the current redistribution problem. (a),(b) the temperature map in the firing and unfiring sections, respectively. The latching causes a stable normal domain in all sections of the wire. (c) The normal domain, and (d) the currents through the firing (red) and unfiring (blue) sections after latching has occurred.

4.5. Solutions for the Latching Problem

In the previous section, we observed that in some situations, e.g. $I_B \approx I_C$, increasing of the series resistance for the purpose of decreasing the leakage current, ends up in the latching of the nanowires in a stable resistive regime. This problem arises as the currents which were depleted from the firing wires, recover too fast in the wire, introducing more source of heating in the wires which cannot be dissipated and finally stops the detector from responding to the subsequent

photons. Considering the temporal dynamics of the SSPD [8], two solutions exist to avoid latching: either increasing the kinetic inductance of the device L_k , or decreasing the load resistance R_L . In both cases the L/R time constant of the circuit becomes larger, leading to a slower response which allows the normal region to be completely away before the current recovers in the wire. However, increasing the kinetic inductance usually requires increasing the total dimension of the device, which will be finally limited to assure the wire uniformity [9]. Decreasing the load resistance allows proper operation of PNDs with smaller area, but it comes at the price of a reduced signal pulse level and therefore a reduced signal to noise ratio. Moreover, realization of a low-impedance load, i.e. a low-impedance pre-amplifier stage is not trivial. To have an idea, if the before-mentioned 4-PND, with $12 \times 12 \mu\text{m}^2$ active area ($L_K=135$ nH and $R_S=50 \Omega$ series resistance in each section) is going to properly work at $I_B=0.95 \times I_C$, it requires a $R_L=5 \Omega$ load resistance. In the next chapter a new PNR detector design is demonstrated to avoid the problems regarding the parallel configuration.

4.6. Conclusion

In the PND structures, the problem of leakage current redistribution puts a limit on the number of detecting elements that can be arranged in parallel and the maximum bias current that can be applied to the device. These limitations exclude PND as the candidate for a scalable, efficient PNR detector, unless a low-impedance pre-amplifier is implemented with the device. However, the fast response time in a PND due to its small kinetic inductance is a unique advantage to be used as an ultra-fast single photon detector. On the other hand, the cascade switching of PNDs, although is undesirable in a PNR application, but is employed in the newly-emerged superconducting avalanche photon detectors (SNAPs) [10], to achieve a high signal to noise ratio for the reliable readout of the ultra-narrow superconducting detectors sensitive up to mid-infrared wavelengths.

References

- [1] M. Fitch, B. Jacobs, T. Pittman, and J. Franson, "Photon-number resolution using time-multiplexed single-photon detectors," *Physical Review A*, vol. 68, no. 4, pp. 1-6, 2003.
- [2] E. A. Dauler et al., "Photon-number-resolution with sub-30-ps timing using multi-element superconducting nanowire single photon detectors," *Journal of Modern Optics*, vol. 56, no. 2-3, pp. 364-373, 2009.

- [3] D. Achilles, C. Silberhorn, C. Silwa, K. Banaszek, and I. A. Walmsley, "Fiber-assisted detection with photon number resolution.," *Optics letters*, vol. 28, no. 23, pp. 2387-9, 2003.
- [4] A. Divochiy et al., "Superconducting nanowire photon-number-resolving detector at telecommunication wavelengths," *Nature Photonics*, vol. 2, no. 5, pp. 302-306, 2008.
- [5] F. Marsili et al., "Physics and application of photon number resolving detectors based on superconducting parallel nanowires," *New Journal of Physics*, vol. 11, no. 4, p. 045022, 2009.
- [6] M. Ejrnaes et al., "A cascade switching superconducting single photon detector," *Applied Physics Letters*, vol. 91, no. 26, pp. 262509, 2007.
- [7] J. K. W. Yang, A. J. Kerman, E. A. Dauler, V. Anant, K. M. Rosfjord, and K. K. Berggren, "Modeling the electrical and thermal response of superconducting nanowire single-photon detectors," *IEEE Transactions on Applied Superconductivity*, vol. 17, no. 2, pp. 581-585, 2007.
- [8] A. J. Kerman et al., "Kinetic-inductance-limited reset time of superconducting nanowire photon counters," *Applied Physics Letters*, vol. 88, no. 11, pp. 111116, 2006.
- [9] F. Mattioli et al., "Large area single photon detectors based on parallel configuration NbN nanowires," *Journal of Vacuum Science & Technology B: Microelectronics and Nanometer Structures*, vol. 30, no. 3, pp. 031204, 2012.
- [10] F. Marsili et al., "Single-photon detectors based on ultranarrow superconducting nanowires.," *Nano letters*, vol. 11, no. 5, pp. 2048-53, 2011.

CHAPTER 5

Series Nanowire Detectors^{*}

In the previous chapter, a superconducting PNR detector, the Parallel Nanowire Detector (PND), was studied. Being composed of parallel superconducting nanowires, a PND significantly outperforms the other PNR detectors in terms of sensitivity and speed especially in the telecommunication wavelength range. Although the presented performance of PND already allows some applications in quantum-optics experiments such as quantum state reconstruction, increasing the efficiency is needed for the single-shot measurement of photon number, in many quantum communication and computing protocols. Furthermore, increasing the maximum achievable detected photon number to tens of photons is demanded for a PNR detector to be used as an “analog” detector with single-photon sensitivity, bridging the gap between conventional and single-photon detectors. However, PNDs are limited in terms of dynamic range (maximum number of photons which can be detected in a pulse) and efficiency, due to the problem of current redistribution in the array after photon detection in one or more wires. The current redistribution problem can result in spurious switching of the wires which did not absorb a photon, generating false counts. Avoiding this problem requires decreasing the number of elements in the array as well as limiting the bias current well below the critical current, which prevents reaching the highest efficiency in a conventional device with ~100 nm wide nanowires.

In this chapter we demonstrate a novel PNR detector based on the “series” connection of superconducting nanowires, called Series Nanowire Detector (SND). Similar to the PND, SND is also based on spatial multiplexing of superconducting nanowire detectors, hence preserves all the advantages of SSPDs in terms of simplicity, sensitivity, timing resolution and speed. As it will be shown in the following sections, SNDs solve the current redistribution problem related to PNDs, therefore enable a much larger dynamic range of up to few tens of photons at bias currents very close to the critical value. Therefore, using the series configuration can result in higher QE PNRs with the possibility to detect large photon numbers. Using the electro-thermal simulation, a design for a large dynamic range SND is presented. Finally a proof-of-principle SND

^{*} This chapter has been published in *Optics Express*, vol. 20, no. 5, 2012, and *Applied Physics Letters*, vol. 101, no. 7, 2012.

with $N=4$ series sections (4-SND) is demonstrated as the first prototype of this detector structure with the ability to register up to 4-photon detection events in the telecommunication wavelength window.

5.1. Theory of SND

5.1.1. SND structure and operation principle

The SND has an electrical structure which is dual to the one of the PND. It is made of the series connection of N superconducting nanowires, each connected in parallel to a resistor R_p . As it is shown in Fig. 5.1, each nanowire is electrically modeled as an inductor L_k , in series with a time variable resistor $R_n(t)$ with a nonzero value after absorption of a photon. The parallel resistor R_p may be monolithically integrated with the nanowire, for example as shown in Fig. 5.1, by deposition and patterning of AuPd thin films. The resistor could also be defined below or above the NbN wire, in order to maximize the filling factor.

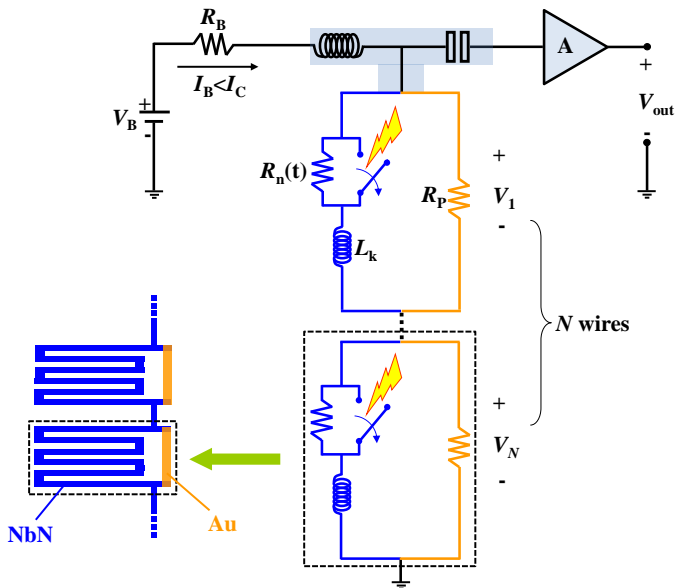


Fig. 5.1 Electrical circuit and layout schematics for the implementation of SND structures. The voltage source in series with a bias resistor provides the biasing of the detector through the DC arm of the bias-T. The RF arm is connected to the amplifier circuit. N nanowires, each with a resistor in parallel, are connected in series. The voltages produced by photon absorption in different sections are summed up in the output.

All the detecting sections are equally biased (in series) with a bias current close to the critical current which is typically the same for all branches. Absorption of a photon in one branch temporarily perturbs the superconductivity [1], forming a resistive section across the wire. If the value of R_P is smaller than the photon-induced normal resistance of the nanowire $R_n(t)$, the bias current switches to the parallel resistor and a voltage pulse is formed across the branch. If more branches fire, the voltages produced across them are summed up and the output voltage is proportional to the number of firing detectors, i.e. the number of absorbed photons, provided that all photons are absorbed in distinct branches. The parallel resistance R_P has the key role of discharging the wire after a resistive transition, thus avoiding latching.

In the case of the traditional $50\ \Omega$ readout via a coaxial cable, after one section absorbs a photon, the bias current is partially redistributed to the load, temporarily reducing the bias in the unfiring branches, and therefore introducing a dead time and decreasing the output voltage level, as it will be shown later in this chapter. This effect can be minimized by using a preamplifier with large input impedance placed in the cryostat close to the device. If the load impedance seen by the SND is large, the leakage current in the output becomes negligible, which not only provides the true measurement of the voltages generated across each element after photon detection events, but also decreases the device response time. A high input impedance cryogenic preamplifier is readily implemented using high-electron-mobility-transistor (HEMT) technologies.

We note that even with the standard $50\ \Omega$ load, this configuration is preferable to the PND structure in which photon absorption in one section results in the increase of the bias current in the other still superconducting sections (unfiring), putting a limit on the maximum bias current and hence on the QE and dynamic range as was shown in chapter 4.

5.1.2. SND electro-thermal simulation

Electro-thermal simulation is performed to model the device response following Ref [2]. Similar to PNDs, in the case of SNDs also the symmetry of the structure and the assumption of identical wires allow us, without loss of generality, to use an electrical equivalent circuit model where all firing (unfiring) sections are lumped together (Fig. 5.2), simplifying the electrical circuit. A single thermal equation can be solved for a firing branch (representing all the detecting branches), providing the resistance value $R_n(t)$ which is then used to solve the electrical circuit.

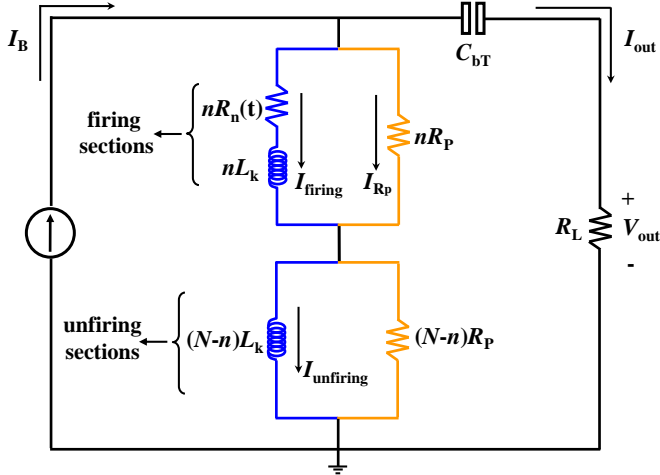


Fig. 5.2. Equivalent circuit model for the firing and unfiring sections of the SND. The DC port of the bias-T is modeled as a constant current source I_B and the AC port is modeled as a capacitor C_{bT} (20 nF).

For the simulation, SND structures are assumed to be made of $d=4.5$ nm thick, $w=100$ nm wide NbN nanowires on a GaAs substrate, folded in a meander with $f=40\%$ filling factor. Two cases with $N=10$, 4 μm -long detecting sections and $N=100$, 40 μm -long detecting sections in series are considered giving square total detection area of 4 $\mu\text{m}\times 4$ μm and 40 $\mu\text{m}\times 40$ μm , respectively. Based on the experimental current-voltage characteristics of a typical NbN SSPD on GaAs, the macroscopic thermal properties of NbN nanowire required for solving the thermal equation are extracted. All the wires are assumed identical with critical temperature $T_C=10.5$ K, and critical current $I_C=22$ μA at the base temperature of $T_{sub}=2$ K, with the kinetic inductance $L_k=90$ pH/ \square . The normal region resistivity is $\rho=3$ $\mu\Omega\text{m}$, thermal boundary conductivity $\alpha=1.92\times 10^4$ W/ Ωm at 2K, and the initial normal domain length $L_{res}=25$ nm. The value of the parallel resistor to each detection section is chosen to be $R_p=80$ Ω , avoiding any latching or unwanted oscillation [3]. Since as a proof-of-principle device, an SND with $N=4$ will be demonstrated in section 5.2, the related simulations for this device is also presented at the end of this section using the associated parameters.

Using the electro-thermal model, it is possible to simulate the temperature change and the growth of the resistive region along the wire after photon absorption. Fig. 5.3(a) shows the temporal evolution of temperature along a switching wire in an SND with $N=10$ sections with the load impedance of $R_L=50$ Ω ($R_L=1$ M Ω gives identical results for the thermal response). Photon absorption at time $t=0$ and the subsequent Joule heating lead to the growth of the initial hotspot, forming a time-variable resistor, as shown in Fig. 5.3(b). As long

as the temperature is increasing, more regions become resistive, leading to a maximum resistance of $R_n \approx 320 \Omega$. This resistive region starts to shrink as the bias current is diverted to R_p , and finally disappears in $t \sim 50$ ps. Fig. 5.3(c) and (d) show the corresponding temperature map and $R_n(t)$ for the case of an $N=100$ sections SND read-out by a $R_L=1 \text{ M}\Omega$ load, where the number of squares for each element (and consequently L_k) is 10 times larger. In this case, due to the larger kinetic inductance, the hotspot expands more before it cools down. This results in a normal state resistance of $\sim 1.1 \text{ k}\Omega$ which drops down to zero in ~ 110 ps. It should be noted that although the maximum temperature of the hotspot in both cases is still lower than T_C , the superconducting to normal transition occurs in the hot regions when the bias current exceeds the critical current, which strongly decreases as the temperature rises.

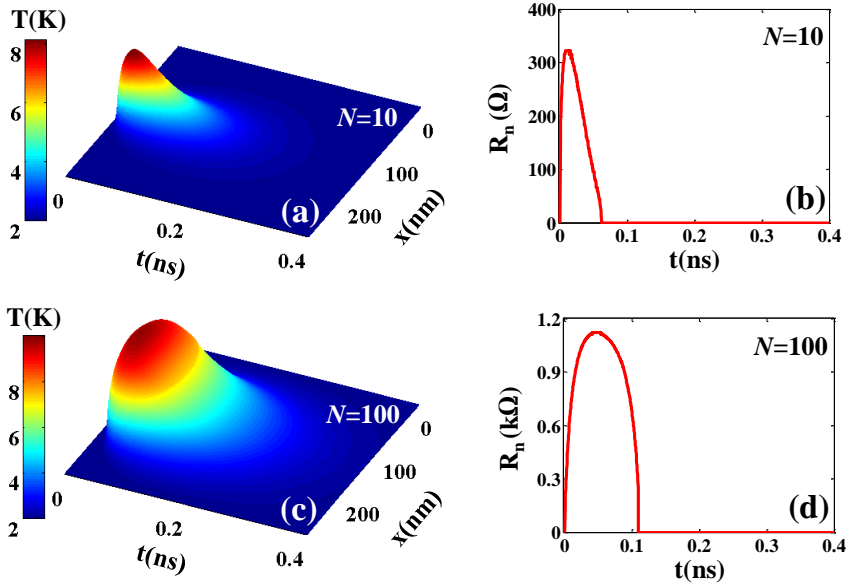


Fig. 5.3. Electro-thermal simulation for a firing section of an SND, biased with $I_B=0.99 \times I_C$. (a), (c) Temperature map vs. time along the switching wire after photon detection in a 10- and 100-SND respectively. (b), (d) Time-dependent resistance for a 10- and 100-SND respectively. ($R_L=50 \Omega$ for 10-SND and $R_L=1 \text{ M}\Omega$ for 100-SND simulation).

5.1.3. Voltage transients

The transient responses of an SND with $N=10$ detection elements, when $n=1$ to $n=10$ photons are absorbed in distinct branches are investigated in Fig. 5.4. Fig. 5.4(a), (b), and (c) illustrate the case for $R_L=50 \Omega$ readout. The transient

current flowing through a firing and an unfiring branch of the SND are illustrated in Fig. 5.4(a), and (b) respectively. Initially, all the wires are superconducting, carrying a bias current $I_B=0.99 \times I_C$ with zero voltage drop across the branches. Photon absorption in the (firing) wire depletes it temporarily from most of its bias current (Fig. 5.4(a)). The depleted current is redistributed in part to the parallel resistor and in part to the load, producing voltage pulses across them. On the other hand, a part of I_B is redistributed to the load and therefore the total bias current going through the detector decreases. This brings about two undesirable effects. Firstly, it reduces the efficiency of all the wires, including the unfiring branches, effectively producing a dead time of \sim few ns (Fig. 5.4(b)). Secondly, the kinetic inductances of the unfiring branches oppose to the change in the bias current by inducing a negative voltage. This reduces the total output voltage as compared to the ideal case.

Fig. 5.4(c) shows the related output voltage transients. The peak output voltage is nearly proportional to the number of switching wires, as it will be shown below. Due to the negative voltage produced across the unfiring branches, the voltage formed across each firing branch cannot be fully measured at the output, so the output voltage is much smaller than sum of the voltages across the firing branches. As shown in Fig. 5.4(c), the voltage step between n and $n+1$ in this case is in the order of $\sim 80\text{--}90 \mu\text{V}$, much smaller than the ideal value of $\sim 1 \text{ mV}$ which is produced by the current flowing through the parallel resistor R_p . It should be noted that the typical minimum voltage pulse that can be correctly amplified and counted using a room temperature amplifier connected to the device via coaxial cable is in the range of $30\text{--}40 \mu\text{V}$ in our setup, which means that, with $N=10$, the signal to noise ratio (SNR) is at least 2. Increasing the number of wires beyond 10 results in smaller voltage step increments and requires cryogenic readout. In the following, it is shown how implementing a high impedance readout can solve this issue.

One advantage of the series configuration over the parallel is that the current of the unfiring sections decreases, instead of increasing, due to current redistribution. Therefore, in the SND current redistribution only reduces the output voltage and produces a dead time (of the order of few ns), while in the PND it causes the bias current of the unfiring section to exceed the critical current, which results in the switching of the unfiring wire and a false detection. This problem gets worse when the number of detecting elements in the PND is increased. In contrast, an SND, even with a large number of wires and hence a high dynamic range, can be biased very close to its I_C , getting benefit from its maximum QE.

Fig. 5.4(d)–(f) show the transient responses of the same SND with a high impedance readout of $R_L=1 \text{ M}\Omega$. In this case, the current redistribution problem is not present. The current transient in the firing branches does not depend on the number of switching wires, and is entirely diverted to the parallel resistor. The

current of the unfiring section also remains unchanged, i.e. $I_{\text{unfiring}}=I_B$ (Fig. 5.4(e)). Therefore, the voltage developed across a section after each photon detection event is accurately measured across the load and the voltage of the unfiring branch remains zero.

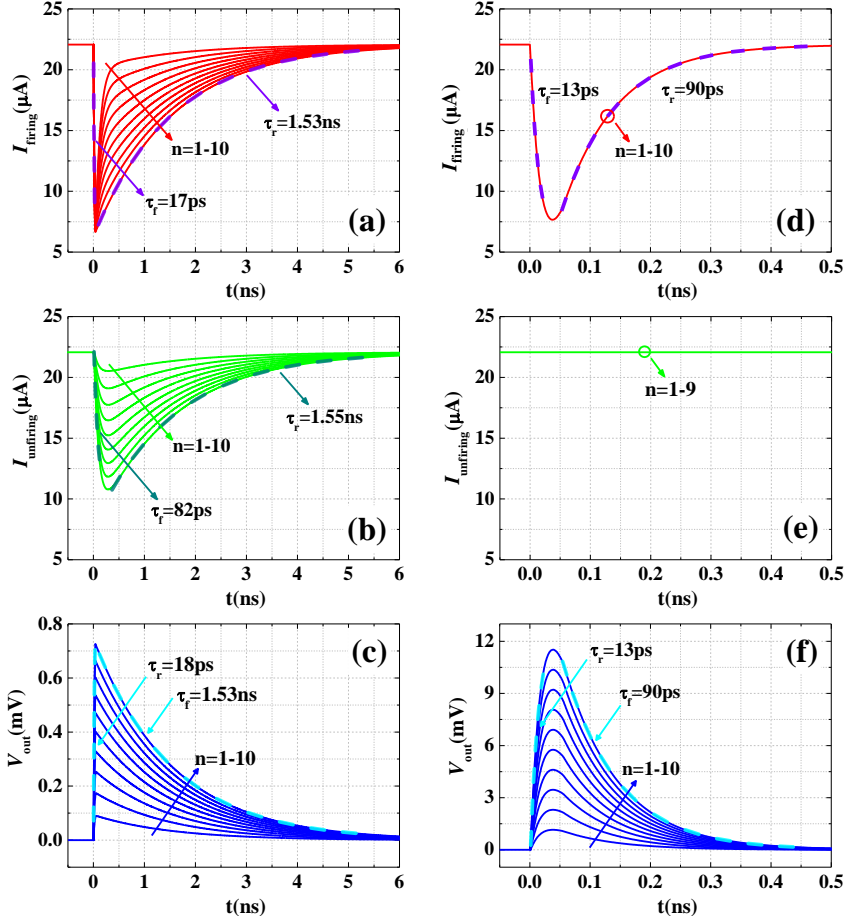


Fig. 5.4. Transient current flowing through the (a) firing, I_{firing} and (b) unfiring, I_{unfiring} sections of an SND with $N=10$, $R_L=50 \Omega$, $I_B=0.99 \times I_C$, $R_p=80 \Omega$ after absorption of $n=1-10$ photons. (c) Corresponding output voltage V_{out} . Transient current (d) I_{firing} and (e) I_{unfiring} with the ideal $1 \text{ M}\Omega$ load readout, which are independent of the number of absorbed photons. The large load impedance decouples firing and unfiring sections. (f) The related output voltage with $R_L=1 \text{ M}\Omega$. The dashed lines are exponential fits to the rise/fall times, as explained in section 6.

The decoupling of the detection sections is highly favorable for a PNR detector. Furthermore, the higher voltage levels produced at the high impedance load are substantially easier to read out (Fig. 5.4(f)). This becomes more important in discriminating n and $n+1$ states, particularly when dealing with large dynamic ranges.

As an example, to show how a high input impedance load allows scaling to much larger numbers of wires, the simulation results for the case of $N=100$ wires are presented, in an active area of $40\ \mu\text{m} \times 40\ \mu\text{m}$. Fig. 5.5(a) shows the transient current flowing through the firing branch (I_{firing}), its parallel resistor (I_{R_p}), the unfiring branch (I_{unfiring}), and the load resistor (I_{out}) after $n=1-100$ photon detection event in an SND with $N=100$, $I_B=0.99 \times I_C$, $R_p=80\ \Omega$, and assuming $R_L=1\ \text{M}\Omega$. It is clearly shown that all the current repelled from the switching wire flows only into the parallel resistor ($I_{R_p}=I_B-I_{\text{firing}}$), and no current goes through the load ($I_{\text{out}}=0$), therefore the bias current remains unchanged in the unfiring branches ($I_{\text{unfiring}}=I_B$). In Fig. 5.5(b), the related output voltage for $n=1, 2$ and 3 are shown emphasizing the relatively large voltage step size of $\sim 1.2\ \text{mV}$. Fig. 5.5(c) compares the peak output voltages versus the number of switching wires in log-log scale, in SNDs of $N=10$ and $N=100$, with $50\ \Omega$ and high impedance readout for $N=10$ and only high impedance readout for $N=100$. Although the conventional $50\ \Omega$ readout produces a response close to linear, the signal level is reduced a lot, due to the fact that not all the voltages produced across the parallel resistors are read at the $50\ \Omega$ load. For the high impedance load, however, perfect linearity as well as easy voltage readout is achieved. The slightly larger output voltage and slower response for the $N=100$ case is due to the larger wire length and kinetic inductance used for the $N=100$ design.

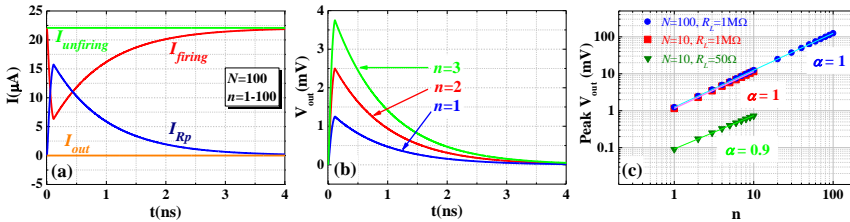


Fig. 5.5. Transient response of an SND with $N=100$, $I_B=0.99 \times I_C$, $R_p=80\ \Omega$, and $R_L=1\ \text{M}\Omega$. (a) Current flowing through the firing I_{firing} , and unfiring I_{unfiring} , sections, the parallel resistor I_{R_p} , and the load I_{out} . (b) Output voltage of the SND when $n=1, 2, 3$ photons are absorbed. (c) Peak output voltages as a function of the number of absorbed photons together with a power-law fit (solid lines) plotted in log-log scale as $V_{\text{out}}=An^\alpha$. For the case of the high impedance load ($1\ \text{M}\Omega$), $\alpha=1$ both for $N=10$ and $N=100$, (red squares and blue circles, respectively). The response is very close to linear ($\alpha=0.9$) even with the $50\ \Omega$ load (green triangles).

5.1.4. Dynamic characteristics of the SND

In order to provide further insight into the dynamics of the SND, the electrical circuit can be simplified according to the knowledge gained from the electro-thermal model. The nonlinear resistor $R_n(t)$ can be modeled as a switch, initially open to a large resistance, which drops to zero in a step-like manner. Discarding the effect of the bias-T capacitance, the two inductive elements related to the firing and unfiring branches in the equivalent circuit of Fig. 5.2 suggest that the circuit can be described by a 2nd order differential equation, therefore the transient responses include two time constants.

In Fig. 5.6 the equivalent circuits used to estimate the time constants for each inductive element of the circuit are shown. Fig. 5.6(a) and (b) show the equivalent circuits seen by the inductances of the firing and unfiring inductors, respectively, when the nanowire is in the resistive state. The time constants τ_1 and τ_2 associated to the firing and unfiring sections determine the pulse rise time, and it is easily seen that τ_1 is always smaller than τ_2 , because of the relatively large resistance of the wire in the normal state. When the nanowire switches back to the superconducting state, the inductances can be lumped together and the problem is simplified to a single R - L circuit with a time constant of τ_3 as shown in Fig. 5.6(c), which determines the pulse decay time.

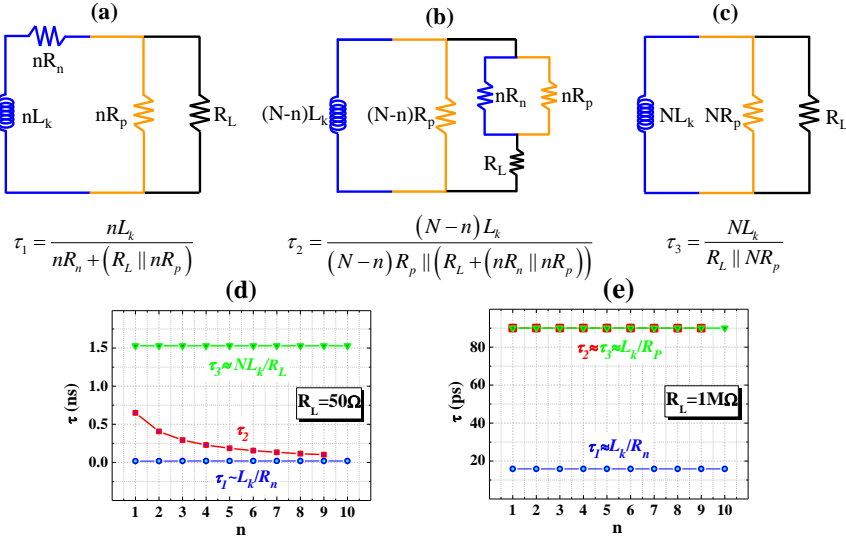


Fig. 5.6. (Color online) Equivalent circuits used to extract the time constants corresponding to the (a) inductances of the firing branches, (b) inductances of the unfiring branches, and (c) the total inductance after the wires have switched back to the superconducting state. (d), (e) The calculated time constants of the $N=10$ elements SND with $R_L=50 \Omega$ and $R_L=1 M\Omega$.

In Fig. 5.6(d) the three different time constants τ_1 – τ_3 , calculated for the SND with $N=10$ elements and $R_L=50\ \Omega$, are plotted as a function of n . It is seen that τ_1 and τ_3 are almost independent of n . For $n \times R_n > (R_L/n \times R_p)$, τ_1 tends to $\tau_1 \approx L_k/R_n$ which is in the range of 20 ps for this case while $\tau_3 \approx N \times L_k/R_L \approx 1.5$ ns. We note that our calculations do not take into account the hotspot relaxation dynamics which will become significant for rise times in the 20 ps range. It is noteworthy to mention that τ_1 is more than N times smaller than the one of a standard SSPD having the same active area ($=L_k/R_L$), while the recovery time of the SND is the same as a standard SSPD of the same size ($=N \times L_k/R_L$). In Fig. 5.6(e) the time constants related to the high impedance load of $R_L=1\ \text{M}\Omega$ are plotted. It is clear that a large value of R_L results in $\tau_1 \approx L_k/(R_n+R_p) \approx L_k/R_n$ and $\tau_2 \approx \tau_3 \approx L_k/R_p$ which means that the recovery time is improved at least by a factor of N . This implies that as far as R_p is chosen so that it avoids latching, increasing R_L has no effect on latching but favors the SND with a much faster response time. The SND can therefore also be used as a large area single-photon detector with high counting rates.

To verify the estimated transient dynamics, in Fig. 5.4 the transient responses for some special cases are fitted with exponential functions (dashed lines), which all correspond very well with the expected time constants τ_1 and τ_3 , given in the equations of Fig. 5.6. We can conclude that for the $N=10$ elements SND, the maximum repetition range can reach nearly 200 MHz with a traditional readout, while with a high impedance readout it can exceed 2 GHz.

5.1.5. SND response with realistic high-impedance readout

In the preceding sections, the advantages of using a preamplifier with high input impedance were shown. However, it is worth mentioning that the frequency response of such preamplifier, and particularly its input capacitance, might impose some limits on the performance of the detector. Therefore the SND design must be optimized taking into account the actual preamplifier characteristics. For instance, using a commercially available HEMT in the common source configuration in the cryogenic preamplifier stage with the total input capacitance of $C=180\ \text{fF}$ for reading out an SND with $N=10$ sections, requires a change in the value of the parallel and load resistors to $R_p=40\ \Omega$ and $R_L=10\ \text{k}\Omega$, respectively, to avoid latching. For an SND with $N=100$ sections with $R_p=40\ \Omega$, the load resistance can be kept as $R_L=1\ \text{M}\Omega$. The output voltages considering the added parallel capacitance at $I_B=0.99 \times I_C$ for the case of $n=1$ – 10 detected photons are shown in Fig. 5.7, with the insets showing the linearity of the output voltages versus the number of detected photons. It is seen that although lowering R_p and R_L decreases the signal amplitude, the effect on the linearity is marginal and both output amplitude and linearity are still much better than the case of $50\ \Omega$ readout.

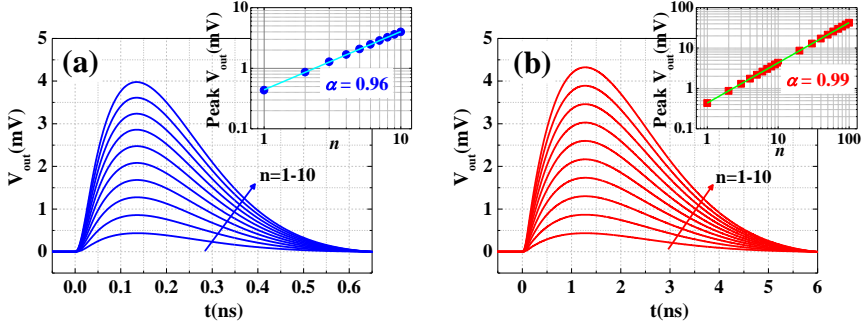


Fig. 5.7. Output voltage of an SND with N series section each connected in parallel to $R_P=40\ \Omega$ and biased at $I_B=0.99I_C$, considering the effect of $C=180\ \text{fF}$ input capacitor in parallel to the load resistor. (a) $N=10$, and $R_L=10\ \text{k}\Omega$ when $n=1, 2, \dots, 10$ photons are detected. The inset shows the linearity of the peak output voltages as a function of the number of detected photons together with a power-law fit (solid line) plotted in log-log scale as $V_{\text{out}}=An^\alpha$ where $\alpha=0.96$ (b) $N=100$, and $R_L=1\ \text{M}\Omega$. The inset shows the power-law fit of $n=1-100$ detected photons with excellent linearity of $\alpha=0.99$.

In this case, although the rise time is affected by the added RC time constant, the dynamic characteristic for the recovery time (fall time) is still dominated by the time constant related to the kinetic inductance, i.e. $\tau \approx L_k/R_p$. Note that the longer fall times in Fig. 5.7 compared to Fig. 5.4 and 5.5 stem from the fact that in the circuit with $C=180\ \text{fF}$ in parallel to R_L , a smaller R_p ($40\ \Omega$) is chosen in order to avoid latching or unwanted oscillations.

5.1.6. Limitations of the fidelity in an SND

The considerations above only pertain to the linearity of the output voltage as a function of the number of firing sections. In a spatially-multiplexed detector, such as the SND, the finite number of sections and imperfect efficiency can further limit an accurate measurement of the photon number. In order to discuss these limitations, it is useful to distinguish between two classes of applications for which a PNR can be used. On one hand, in photonic quantum information processing, the number of photons produced in a setup (e.g. a probabilistic quantum gate) must be accurately measured. In this case, the detector is best characterized through the associated positive-operator-valued-measure (POVM) matrices [4], which boil down to the probabilities $P(m|n)$ of measuring m photons when n are incident. Here, we take the probability $P(n|n)$ of correctly measuring n incident photons as a measure of fidelity. In order to maximize the probability of detecting all photons in an optical pulse, it is necessary that the number N of detection elements is much larger than n , so that the probability that two or more photons are absorbed in the same detector is small. On the other hand, each detecting element may have a non-unity QE, which imposes another limitation to the fidelity of photon state detection, resulting in an underestimation of the

number of incident photons. As shown in [8], when n photons are evenly distributed to N output modes ($n \leq N$), and at each output mode there is a detector with quantum efficiency $\text{QE}=\eta$, the probability of detecting all n photons is given by: $P_n^N(n|n) = (\eta/N)^n N!/(N-n)!$. In Fig. 5.8(a), $P_n^N(n|n)$ is plotted for $n=1-10$ photons, with a $N=100$ element-SND, assuming three cases with QE values of 1, 0.9 and 0.8 for all the detecting elements. As it was previously shown [5], having high QE is crucial, especially when detection of large photon states is required. The integration of nanowires with microcavities and waveguides has already resulted in QE values in the 80-90% range. The fidelity of SND is similar to other PNR detectors based on multiplexing techniques. While approaches based on the direct measurement of the total pulse energy, such as the TES, do not suffer from the limited number of elements, the high speed and comparatively high operating temperature make the SND a unique candidate for quantum photonics applications, especially for PNR detection in the telecom wavelength range.

Another application of the SND is to work as a very sensitive linear optical detector of classical light, determining the average number of photons in a weak coherent optical source, for example in ultra-long distance optical communication or optical time domain reflectometry. Also in this case a possible limitation is represented by the finite probability that photons are absorbed in the same nanowire, leading to an underestimation of the average number of incident photons. In contrast, the non-unity QE does not affect the SND performance, apart from a reduction in sensitivity, since a Poissonian photon distribution remains Poissonian under the influence of linear loss, and the average detected photon number scales simply as the QE.

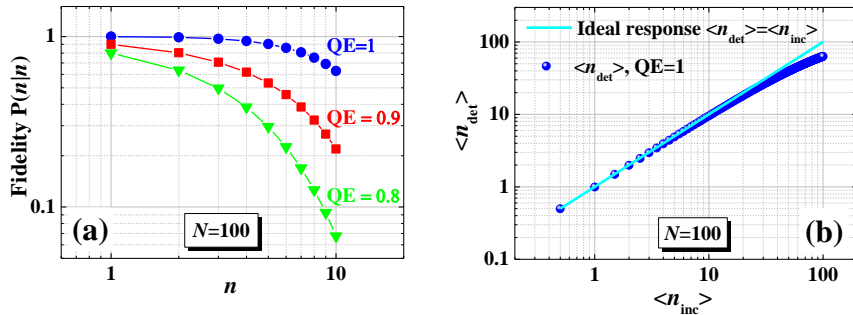


Fig. 5.8. (a) Probability of detecting $n=1-10$ photons when $n=1-10$ photons hit the SND with $N=100$ detecting elements, with different values of $\text{QE}=0.8$, 0.9, and 1. (b) Calculated average number of detected photons $\langle n_{\text{det}} \rangle$ as a function of the average number of incident photons $\langle n_{\text{inc}} \rangle$, evenly distributed to $N=100$ detecting sections of the SND with unity QE (blue circles), compared with ideal response, the light blue line with slope=1.

The symbols in Fig. 5.8(b) show the average number of detected photons $\langle n_{\text{det}} \rangle$ as a function of the average number of incident photons per pulse $\langle n_{\text{inc}} \rangle$ assuming a Poissonian source, for an SND with $N=100$ elements and $\text{QE}=1$, calculated as described in [6]. The comparison of the results with the unity-slope line (in light blue) reveals that the linearity is conserved in the limit $n \ll N$, with increasing saturation as n approaches N . However, the deviation from a linear slope is quite acceptable even for $n \sim N/2$.

5.1.7. Simulation of the fabricated 4-SND

As it was mentioned in the introduction, a proof-of-principle SND having 4 series elements (4-SND) is fabricated to confirm the PNR operation of the series structure. Before showing the fabrication and experimental results of this detector, the dynamics of the photoresponse are simulated using the electro-thermal model with the simulation parameters extracted from the I-V curves of the fabricated device. Fig. 5.9 illustrates the simulated output voltage of the fabricated 4-SND when $n=1-4$ photons are detected in distinct elements. The simulation parameters are based on the model described in chapter 2 following Ref. [2] and on the device parameters used in the experiment described below ($I_C=12.5 \mu\text{A}$, $I_B=0.99 \times I_C$, $R_p=29.5 \Omega$, $R_L=50 \Omega$, kinetic inductance $L_K=100 \text{ nH}$ for each element). The relevant (1/e) time constant of the response exponential decay $\tau_F=N \times L_K / (N \times R_p \parallel R_L)$ is calculated as $\tau_F=11.4 \text{ ns}$ in this device, which is relatively large due to the size of the device. The recovery time of the device is expected to be $\sim 3 \times \tau_F$.

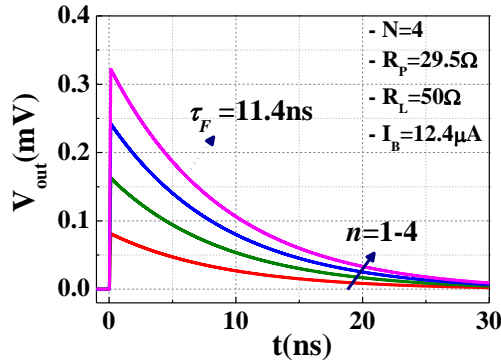


Fig. 5.9. Transient response of the 4-SND biased at $I_B=0.99 \times I_C$, simulated using the electro-thermal model [7].

5.2. SND Realization

Here, the fabrication and experimental demonstration of an SND with $N=4$ detecting elements in series (4-SND) is reported, as a proof of principle.

5.2.1. Fabrication

The fabrication of SNDs is realized at the CNR-IFN laboratory in Rome (by Dr. F. Mattioli, Dr. A. Gaggero, in the group of Dr. R. Leoni) on films grown at TU/e by D. Sahin, is similar to the one for PNDs reported in the previous chapter [8]. SNDs are fabricated from a 4.5 nm thick NbN film grown on GaAs substrate by reactive magnetron sputtering, at a nominal deposition temperature of 410° C. This particular film exhibited a superconducting transition temperature of 9.5 K and a superconducting transition width of 0.7 K. To fabricate the SND structures, four nanolithography steps are carried out using field emission gun electron beam lithography (EBL) system with acceleration voltage of 100 kV. In the first step, Ti/Au (60 nm Au, on 10 nm Ti) contact pads together with alignment markers are fabricated by lift-off using a Polymethyl Methacrylate (PMMA) stencil mask. This is followed by the second lithographic step to define the thin Ti/Au (20 nm Au, on 5 nm Ti) pads used for the electrical contact of the resistors. In the third step, hydrogen silsesquioxane (HSQ) is used as an etch mask to pattern the meanders with reactive-ion-etching (RIE). In the last step the parallel resistors (40 nm thick AuPd film) are fabricated by lift-off via a PMMA stencil mask.

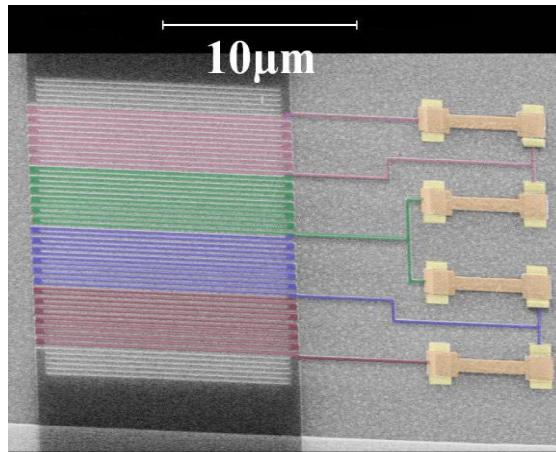


Fig. 5.10. Scanning electron microscope (SEM) image of the 4-SND. The active wires, the parallel resistors and their contact pads have been colored for clarity.

Fig. 5.10 shows a scanning electron microscope (SEM) image of the fabricated SND with $N=4$ detecting elements. The NbN nanowires are 100 nm wide, covering a total active area of $12 \times 12 \mu\text{m}^2$ with a filling factor $f=40\%$. The NbN wires which connect the meanders to the parallel resistors are 250 nm wide and their effect on the response dynamics is assumed to be negligible.

5.2.2. Electrical characterization

The electro-optical characterization of the SND was performed in the closed-cycle cryocooler (see section 2.1, with the assistance of Dr. G. Frucci) at a base temperature of $T=1.18$ K on the experimental plate and stability within $\Delta T=0.01$ K. As it is schematically depicted in Fig. 5.1, the bias current is supplied through the DC port of a bias-T by a voltage source in series with a $R_B=10$ Ω bias resistor.

The current-voltage (I-V) characteristic of the device is displayed in Fig. 5.9. In the superconducting state, the parallel resistors are short circuited by the zero resistance of the wire, having no effect on the I-V. As soon as the bias current exceeds the critical current of a nanowire, a normal domain with finite resistance is formed across it, and a part of the bias current is pushed to the parallel resistance. Due to the effect of the parallel resistance, the typical relaxation oscillation regime and the hotspot plateau are not observed. In a section, when the entire length of a nanowire becomes normal, the resistance is the parallel equivalent of the nanowire normal resistances (estimated to be $R_{\text{nanowire}}\sim 70$ k Ω , from the measured normal resistance of test SSPD devices on the same chip) and R_p , which is very close to R_p . Following the transition of all the sections to the normal state, the device has a resistance equal to the sum of all parallel resistances. The reciprocal of the slope of the linear fit indicated in Fig. 5.11 corresponds to $4\times R_p=118$ Ω , hence R_p is estimated to be 29.5 Ω . There are some test resistors defined on each sample chip which were measured to have a resistance of ~ 30 Ω at $T=4.2$ K, consistent with the value estimated from the slope of the I-V.

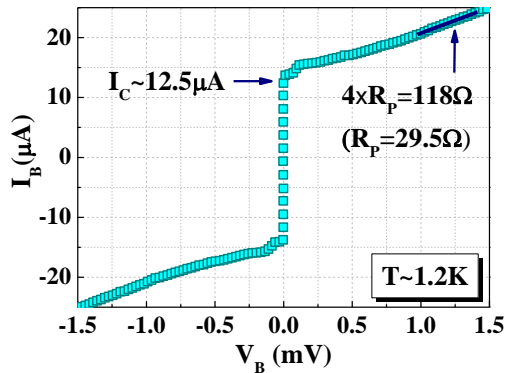


Fig. 5.11. I-V characteristics of the 4-SND.

5.2.3. Optical characterization

For the optical characterization, the light produced by a pulsed laser-diode with 50 ps pulse width, 1.3 μm wavelength, and 10 MHz repetition rate was

coupled to the device through a single-mode polarization maintaining lensed fiber with $1/e^2$ beam diameter of $5\ \mu\text{m}$ mounted on XYZ piezo stages. The fiber connector key was oriented with the fast axis, which was aligned in a direction parallel to the nanowires. The output signal of the detector was collected at room temperature through the RF arm of the bias-T, amplified using a chain of wideband amplifiers and directed either to a 40 GHz bandwidth sampling oscilloscope, or a 350 MHz counter for optical characterization.

Firstly, to investigate the photon number resolving capability of the detector, the distribution of the output voltage pulses was measured using a sampling oscilloscope triggered with the laser-diode modulation signal. In order to couple the light equally to all sections of the SND, the beam was defocused to a larger spot diameter, estimated to be $\sim 20\ \mu\text{m}$, achieving uniform illumination across the $12 \times 12\ \mu\text{m}^2$ area of the detector. Fig. 5.12(a) shows as an example the oscilloscope persistence map measured at $I_B = 8.3\ \mu\text{A}$ and for an incident power corresponding to an average of 3800 photons/pulse coupled at the input of cryostat fiber. With the light intentionally defocused, the single-photon system quantum efficiency is measured at a very low photon flux by dividing the count rate to the number of photons at the input of the cryostat, resulting in a value of 0.076% at $I_B = 8.3\ \mu\text{A}$. Therefore, out of 3800 photons in each optical pulse, $\mu \sim 2.9$ were detected on average.

Discrete voltage heights corresponding to the switching of 1 to 4 elements can be observed. The symmetric pulse shape, especially the slow rise time, as compared to the calculated response in Fig. 5.9, is ascribed to the effect of a low-pass filter (DC-80 MHz) used to remove the high frequency noise of the signal and to improve the visibility of the voltage peaks, which were discernible even without this low-pass filter [9]. The inset in Fig. 5.12(a) shows the persistence trace without using the lowpass filter for a higher photon flux so that only the 4-photon detection is observed. The simulated output voltage when all of the four detection sections of SND fire is also plotted, showing good agreement with the experimental data. The minor discrepancies in the rise/fall times originate from the effect of the amplifier bandwidth which is not considered in the simulation.

The related histogram for the recorded peak voltage levels is shown in Fig. 5.12(b), featuring a series of peaks broadened due to the presence of noise. The histogram can be fitted with a multiple-peak Gaussian distribution (solid light blue line) where each peak, corresponding to the switching of different number of elements in the SND, has a Gaussian distribution (gray dotted curves). The first peak which is entirely due to the electrical noise corresponds to the case when no photon was detected, ('0'-level). The peaks at 12.5, 24.5, 37, and 50 mV correspond to the switching of 1, 2, 3, and 4 elements, respectively. The evenly-spaced, clearly resolved peaks in the histogram show the photon-number-resolving functionality of the SND structure and confirm that conventional $50\ \Omega$

amplification is sufficient for the 4-SND to distinguish up to four detected photons per pulse.

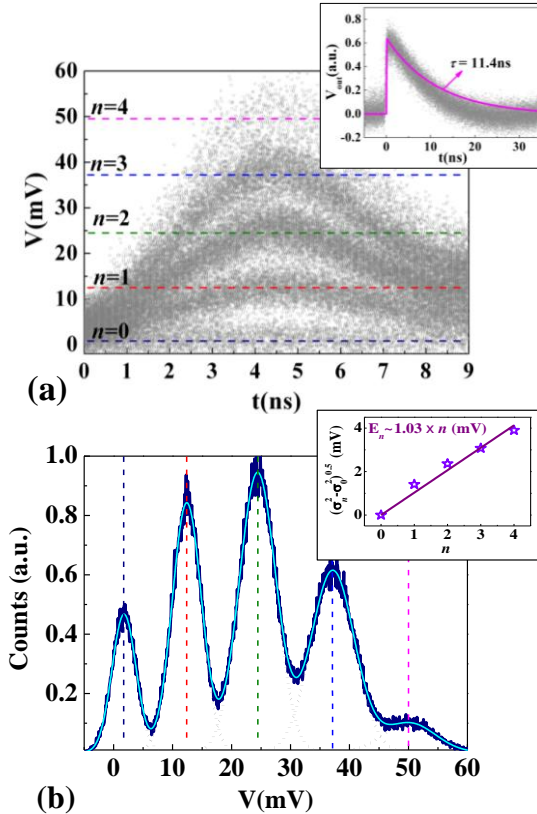


Fig. 5.12. (a) An oscilloscope persistence map with an average of 2.9 photons detected in each pulse. Inset: A persistence trace at a very high photon flux where in each pulse all the 4 elements fire, together with the simulated output pulse. (b) Measured (dark blue) and fitted (light blue) pulse height distribution at $\mu \approx 2.9$, corresponding to the detection of up to 4 photons, along with the Gaussian fits (gray dotted line). The inset plots the excess noise of the SND, E_n , as a function of n .

We observe an increase in the widths of the Gaussian peaks when the photon number is increased, which is an indication of an excess noise. Indeed, when distinct elements of the SND detect photons simultaneously, the output voltage amplitude changes accordingly, with a linear dependence on the number of switching nanowires (i.e., number of detected photons). However, the presence of the electrical noise causes some fluctuation in the output voltage pulse.

Correspondingly, the histogram of the peak output voltages consists of a series of Gaussian peaks, rather than a series of Dirac delta functions. The width of each Gaussian peak corresponds to the electrical noise of the related photon detection event. In the histogram of Fig. 5.12(b), we can observe an increase in the widths of the Gaussian peaks when the photon number is increased. This is an evidence of an “excess noise” with increasing the photon number n , which may be attributed to two major sources. The first is the accumulation of the intrinsic noise of each detection event, related to the variation in the resistance of the normal region [10] in each photon detection event. This noise, whose root mean square (rms) value is expected to scale as $n^{0.5}$, can be reduced by having more uniform nanowires. The second source of excess noise is the variation of the amplifier noise due to the varying detector impedance, which is the source impedance seen by the amplifier. In particular, the rms noise produced by the equivalent noise current generator of the amplifier is expected to scale proportionally to the detector impedance, therefore to n , for small n (i.e., as long as the detector impedance is smaller than the amplifier input impedance), and to saturate as n becomes larger. As the amplifiers used in this measurement have large noise figures (3.3 dB) and large noise current due to the bipolar transistor technology, they have a large contribution to the total noise which increases with the device resistance. Therefore, we believe that the noise performance is not the best we could achieve with this device. The other possible noise sources, such as the thermal noise of the parallel resistors, are calculated to be negligible as compared to the observed noise. Indeed, in the bandwidth of 20 MHz–80 MHz, the rms noise voltage of a resistance $R_p=29.5 \Omega$ is estimated to be only a fraction of microvolt, while the generated signal across the resistance is in the order of tens of microvolt. The inset in Fig. 5.12(b) plots the measured excess noise, defined as $E_n = (\sigma_n^2 - \sigma_0^2)^{0.5}$, where σ_n and σ_0 are the standard deviations of the histogram peaks corresponding to n and 0 firing sections, respectively, as a function of n . The data shows an approximately linear behavior ($E_n \propto n$), with some saturation for large n . As both sources of excess noise would give rise to a sub-linear dependence it is not possible to reliably discriminate between the two with the data in Fig. 5.12(b). We note that, with the presented readout circuit, the excess noise would limit the photon number discrimination ability to $N \sim 4$. However, using a cryogenic low-noise preamplifier and/or a preamplifier circuit designed to optimize the signal-to-noise ratio should result in a much increased dynamic range.

Subsequently, the count rate statistics were studied by analyzing the response of the device with a counter. In a spatially-multiplexed detector such as a SND having N single photon detecting elements with quantum efficiency of η , the probability of detecting m photons, in a coherent laser pulse is [5]:

$$P_{\eta}^N(m|\mu) = \sum_{n=m}^{\infty} \frac{N!}{m!(N-m)!} \frac{\mu^n e^{-\mu}}{n!} \times \sum_{j=0}^m \frac{(-1)^j m!}{j!(m-j)!} \left(1 - \eta + \frac{(m-j)\eta}{N} \right)^n \quad (5.1)$$

where μ is the mean number of photons per pulse (mean number of incident photons multiplied by quantum efficiency). Under uniform illumination with a weak Poissonian source, the probability of detecting at least m photons is almost the same as detecting exactly m photons [11], and is proportional to μ^m . Fig. 5.13 (left) shows the measured count rate per pulse as a function of the threshold level of the counter V_{th} for many different photon fluxes at a fixed bias current of $I_b=10 \mu\text{A}$ (corresponding to $\eta=0.45\%$). The observed shoulders in the count rate pertain to the different detection levels. To prove the PNR capability of the device, count rates at the threshold levels indicated by vertical lines in Fig. 5.13 (left) corresponding to the detection of at least m photons for $m=1$ (red), 2 (green), 3 (blue) and 4 (pink) are plotted in Fig. 5.13 (right) as a function of μ in log-log scale. The solid lines in Fig. 5.13 (right) present the predicted probability of detecting at least m photons in a 4-element SND calculated using Eq. (5.1). As it can be seen from Fig. 5.13 (right), the experimental data are in good agreement with the model. The slopes of the solid lines at low photon fluxes are 1, 2, 3, and 4, which prove that the device can discriminate between 1–4 absorbed photons.

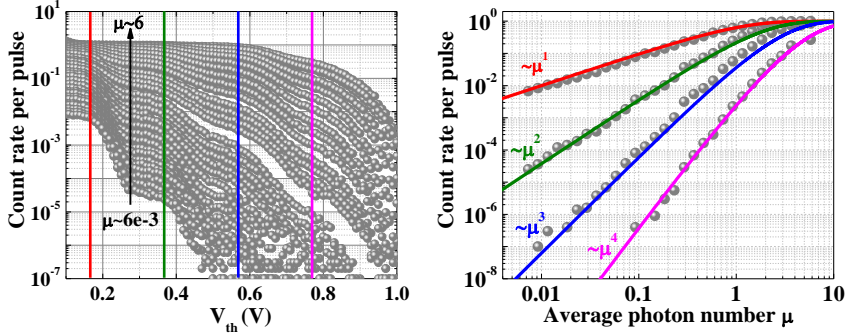


Fig. 5.13. (Left) Count rate per pulse as a function of counter threshold level V_{th} measured with the device under uniform illumination with $0.006 < \mu < 6$. (Right) Probability of photon counts per pulse as a function of μ for four threshold levels, where pulses containing at least 1, 2, 3 and 4 photons are counted. Very good agreement between experimental data and the model is obtained.

Finally, to characterize the SND in terms of efficiency, the single-photon system quantum efficiency (SQE) was measured under weak, well-focused central illumination such that only 1-photon detection event was observed. The value of SQE was obtained by dividing the number of photocounts (corrected for dark counts) by the average number of photons at the input of the cryostat. The

result is plotted in Fig. 5.14(a) (left axis) as a function of bias current. The SQE attains its highest value of 2.6% at a bias current of $I_B=12.4 \mu\text{A}$ ($0.99 \times I_C$) with the light polarized parallel to the wires. It was discussed in chapter 3 that the calculated optical absorptance in a 4.5 nm thick NbN grating with 40% filling factor on GaAs substrate, does not exceed 9% under top illumination at $\lambda=1.3 \mu\text{m}$. Therefore, assuming a negligible fiber loss inside the cryostat, an intrinsic quantum efficiency (the ratio of detected to absorbed photons) of about 30% is derived for the device. The efficiency can be enhanced by improving the superconducting properties of the thin film, making narrower nanowires [12] and applying advanced optical structures, such as optical cavities [13–15] or waveguides [16].

On the right axis of Fig. 5.14, the dark count rate (DCR) is presented as a function of the bias current, as measured by blocking the optical input to the cryostat and moving the fiber away from the device to suppress any spurious light input. A low background level of 1 Hz, due to electrical noise, is measured at low bias currents, with a sharp increase for $I_B > 10 \mu\text{A}$. At $I_B=10 \mu\text{A}$, a SQE of 1% and DCR of around 5 Hz are obtained. It is worth to mention that the dark count measured with the fiber on top of the device was higher at low bias currents due to the effect of the thermal radiation carried by the fiber. This effect can be improved by filtering out the unwanted radiation.

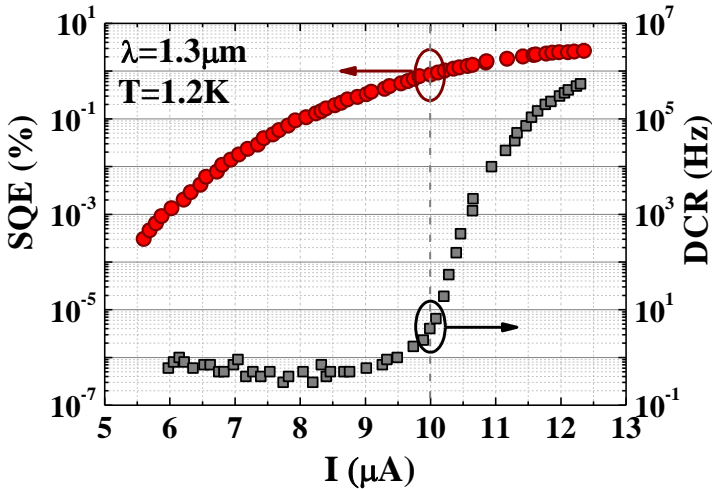


Fig. 5.14 Single-photon system quantum efficiency (SQE) of the 4-SND measured at $\lambda=1.3 \mu\text{m}$ and dark count rate, as a function of the bias current.

The fact that the device could be operated at 99% of the I_C indicates the correct functionality of the shunted wire configuration, as predicted by our model and therefore the possibility of reaching very high QEs. Furthermore, the timing

jitter was measured at the leading edge of the voltage pulse, without lowpass filtering, using the sampling oscilloscope. After quadratically subtracting the jitter from the laser jitter, the measured jitter of the detector, including the amplifying circuit, was 80 ps.

5.3. High Impedance Load

Earlier in this chapter, the need for a high impedance load was explained, in particular for a large dynamic range SND. The typical coax cables connecting the SND to the room-temperature amplification circuits are all $50\ \Omega$ -matched. Therefore, it is important to design a customized high impedance pre-amplifier stage and place it in the cryogenic temperature in the vicinity of the sample, so that the impedance seen by the device is high load impedance. A natural choice to achieve this would be implementation of HEMTs, since they intrinsically have high input impedance and large bandwidth, and can work in the cryogenic temperatures with low noise [17]. A basic amplifier circuit in the common-source configuration was designed using Agilent ATF34143 transistor [18] with a self-bias circuit. The operation point of the amplifier was chosen according to the device typical I-V curves from the transistor datasheet. Also in the datasheet, the high frequency model of the device is provided which is used to simulate the RF behavior of the amplifier using Multisim software. The amplifier is designed to provide $\sim 10\ \text{k}\Omega$ input resistance in the required frequency range and $\sim 50\ \Omega$ output resistance to be matched with the rest of the cables and room temperature electronics. Finally, a printed circuit board (PCB) was designed for the amplifier circuit and the required chip elements were mounted on it. As it was planned to perform the experiments in the dipstick, the size of the PCB was limited to $1 \times 1\ \text{cm}^2$ to fit on the dipstick holder next to the sample chip. Fig. 5.15 shows the schematic of the circuit and the realized amplifier board.

In the period when the amplifier was designed and tested, there was no working SND device available. Therefore, in order to test the amplifier performance, a standard SSPD was employed. In order to avoid latching of the detector, a $50\ \Omega$ resistor was mounted at the input of the amplifier. The signal pad of the SSPD was wire-bonded separately to two different pads. One pad was used to feed the SSPD with DC bias through an inductor connected to the bias line at room temperature. The other pad of the SSPD was wire-bonded to the gate of the cryogenic amplifier, where a coupling capacitor passes the SSPD RF signal to the amplifier. Then a coax cable was employed to transmit the output response of the amplifier to the room temperature and connect it to a chain of room-temperature $50\ \Omega$ amplifiers and finally to the oscilloscope. This amplification stage was needed, since the pre-amplifier stage was not designed to generate high gains and the signal was small to be readout in the oscilloscope. The HEMT needed to be supplied with a 3 V DC bias source at the desired

operation point. The transistor operation point must be chosen carefully to avoid heating of the device. The oscilloscope traces in Fig. 5.15 shows the response of the SSPD confirming the expected operation of the amplifier.

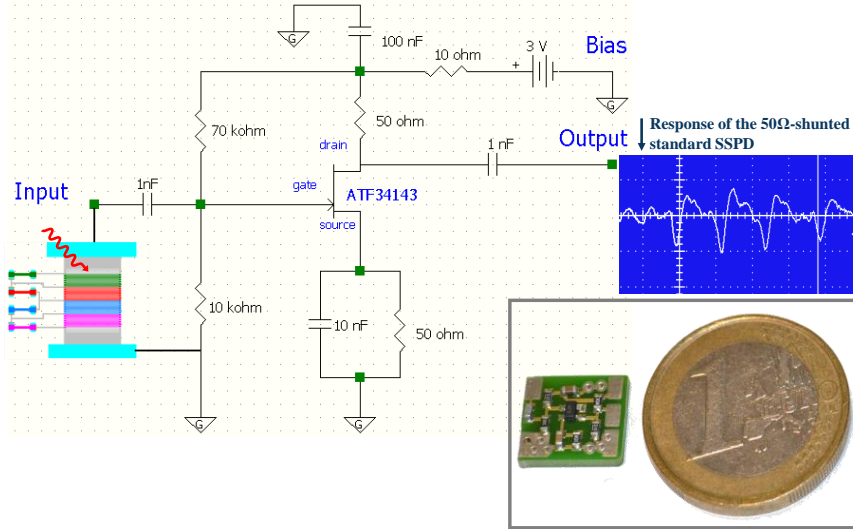


Fig. 5.15. The high input impedance pre-amplifier circuit

5.4. Conclusion

In conclusion, we have implemented a design for PNR detectors based on the series connection of N superconducting nanowires, each shunted with a resistance. The detection of $n=1-4$ photons in the telecom wavelength range was demonstrated in a 4-element SND with maximum system quantum efficiency of 2.6% and recovery time constant in the 10 ns range. Scaling to large number of wires and integration of cavity or waveguide structures should enable efficient PNRs for linear detection in the few to few tens of photons range. Furthermore, we have designed and realized and tested a simple high input impedance amplifier circuit to be integrated with SNDs which have a large number of detecting elements.

References

- [1] G. N. Gol'tsman et al., "Picosecond superconducting single-photon optical detector," *Applied Physics Letters*, vol. 79, no. 6, p. 705, 2001.

- [2] J. K. W. Yang, A. J. Kerman, E. A. Dauler, V. Anant, K. M. Rosfjord, and K. K. Berggren, "Modeling the electrical and thermal response of superconducting nanowire single-photon detectors," *IEEE Transactions on Applied Superconductivity*, vol. 17, no. 2, pp. 581-585, 2007.
- [3] A. J. Kerman, J. K. W. Yang, R. J. Molnar, E. A. Dauler, and K. K. Berggren, "Electrothermal feedback in superconducting nanowire single-photon detectors," *Physical Review B*, vol. 79, no. 100509, 2009.
- [4] J. S. Lundeen et al., "Tomography of quantum detectors," *Nature Physics*, vol. 5, no. 1, pp. 27-30, 2008.
- [5] E. A. Dauler et al., "Photon-number-resolution with sub-30-ps timing using multi-element superconducting nanowire single photon detectors," *Journal of Modern Optics*, vol. 56, no. 2-3, pp. 364-373, Jan. 2009.
- [6] M. Fitch, B. Jacobs, T. Pittman, and J. Franson, "Photon-number resolution using time-multiplexed single-photon detectors," *Physical Review A*, vol. 68, no. 4, pp. 1-6, Oct. 2003.
- [7] S. Jahanmirinejad and A. Fiore, "Proposal for a superconducting photon number resolving detector with large dynamic range," *Optics Express*, vol. 20, no. 5, pp. 5017-28, Feb. 2012.
- [8] A. Divochiy et al., "Superconducting nanowire photon- number-resolving detector at telecommunication wavelengths," *Nature Photonics*, vol. 2, no. 5, pp. 302-306, 2008.
- [9] S. Jahanmirinejad et al., "Photon-number resolving detector based on a series array of superconducting nanowires," *Applied Physics Letters*, vol. 101, no. 072602, 2012.
- [10] J. Kitaygorsky, S. Dorenbos, E. Reiger, R. Schouten, and V. Zwiller, "HEMT-based readout technique for dark- and photon-count studies in NbN superconducting single-photon detectors," *IEEE Transactions on Applied Superconductivity*, vol. 19, no. 3, pp. 346-349, 2009.
- [11] B. E. Kardynal, S. S. Hees, A. J. Shields, C. Nicoll, I. Farrer, and D. A. Ritchie, "Photon number resolving detector based on a quantum dot field

- effect transistor,” *Applied Physics Letters*, vol. 90, no. 18, pp. 181114, 2007.
- [12] F. Marsili et al., “Single-photon detectors based on ultranarrow superconducting nanowires,” *Nano letters*, vol. 11, no. 5, pp. 2048-53, May 2011.
- [13] K. M. Rosfjord et al., “Nanowire single-photon detector with an integrated optical cavity and anti-reflection coating,” *Optics Express*, vol. 14, no. 2, pp. 527-534, 2006.
- [14] B. Baek, J. A. Stern, and S. W. Nam, “Superconducting nanowire single-photon detector in an optical cavity for front-side illumination,” *Applied Physics Letters*, vol. 95, no. 2009, pp. 191110, 2011.
- [15] A. Gaggero, S. Jahanmirinejad, F. Marsili, F. Mattioli, R. Leoni, and D. Bitauld, “Nanowire superconducting single-photon detectors on GaAs for integrated quantum photonic applications,” *Applied Physics Letters*, vol. 97, no. 151108, 2010.
- [16] J. P. Sprengers et al., “Waveguide superconducting single-photon detectors for integrated quantum photonic circuits,” *Applied Physics Letters*, vol. 99, no. 18, pp. 181110, 2011.
- [17] M. S. Reid and M. K. Simon, *Low-noise systems in the deep space network*. John Wiley & Sons, 2008.
- [18] Agilent ATF-34143 datasheet.

CHAPTER 6

Conclusion

At the outset of this PhD project, widespread research had already been conducted on different aspects of SSPDs in order to make them practical devices for many applications in experimental physics and high-speed communication. Within the course of these four years, remarkable progress has been made to improve the functionality of these detectors and show that SSPDs can be applied in more practical applications, owing to the development of technology and better understanding of the detection process. This project aimed at increasing the functionality of SSPDs especially as efficient, photon number resolving detectors for the telecom wavelength range. In summary, the following results were achieved:

- The electrical and thermal dynamics involved in the detection process were modeled using a 1-D, time-dependent numerical analysis for different detector configurations to gain a better understanding of the transient response of SSPDs. Most of the parameters needed for the simulations were extracted from the DC characteristics of the structure under test.
- The simulations performed on the previously-fabricated parallel nanowire detectors (PNDs) revealed the limitations in the efficient, reliable operation of these detectors, due to the current-redistribution problem. Indeed, after detection of a photon in one detector element, its resistance spikes and the current diverts into the external resistance load and into the other detector elements. If a significant number of photons simultaneously trigger multiple elements the current increase in the other pixels may become larger than the critical current, which would cause them to erroneously detect photons. A solution to this problem is increasing the impedance of each element by integrating a series resistance to each detector. But at high values of the series resistors, needed to avoid false counting at high bias currents, the device recovers too fast, and ends up in latching.
- A new device concept, named series nanowire detector (SND) and based on the series connection of shunted superconducting nanowires was proposed. In this configuration, the current redistribution problem does not produce false counting or latching, but just produces a decrease

of the current in the detectors that did not receive photons, resulting in a finite dead time. Both the amount of the current reduction and the dead time can be decreased by increasing the load resistance. This configuration will then be suitable for high dynamic range PNR detectors.

- A high impedance preamplifier has been designed and realized based on low-noise high electron mobility transistors.
- A first prototype of SND structures with 4 series elements has been fabricated in a collaborating group at CNR-IFN institute at Rome, based on the design developed in this thesis. Low-temperature characterization of these devices has been performed in a closed-cycle cryocooler and the expected capability of the detector to register up to 4-photon detection event has been experimentally observed. This result is very significant as it opens the way to high fidelity and high efficiency photon-number detection in the telecom wavelength range.
- In order to improve the efficiency of the SSPDs, a microcavity based on a semiconductor Bragg mirror has been monolithically integrated with a nanowire detector. In these structures a quantum efficiency of 18% at 1300nm was demonstrated, showing a strong resonant enhancement due to the cavity effect, as compared to the ~9% optical absorbance in the NbN meander on bare GaAs substrate. Additionally, an optical modeling of the structure was performed to fit the measured data and understand the cause of the discrepancy between the expected and measured results, to be considered for the future designs.

The presented 4-SND, especially if integrated with optical microcavities to have a higher QE, can be applied to photon number statistics measurements. However, in order to be able to count more simultaneous photons, more detecting elements need to be present in the array. Indeed, the purpose of this project was to enhance the multi-photon response of the SSPDs with regard to the previously demonstrated PNDs and the initial designs were made for $N=12, 24$ and 48 series detecting elements. Unexpected fabrication problems forced us to present the principle of the structure with $N=4$ detectors. Nevertheless, the fabrication of up to 12-pixel SND is currently under way. In future, the following developments in this field can be envisaged:

- The SNDs with high dynamic range are going to be optically tested. It is expected that for the correct measurement of these devices, the cryogenic amplifier be used.
- The current amplifier is realized on a PCB which is not optimum for the low noise behavior at high frequencies. The material and the thickness of the PCB layers of the amplifier need to be optimized to

enhance the high frequency performance of the device through reduction of the parasitic effects.

- The SND structure must be integrated with optical cavity to have high QE.
- The ideal arrangement of different detection elements in a SND is such that a uniform illumination of all pixels is achieved. In the SND with active area larger than the spot size, this is not fulfilled. Achieving uniform illumination within large pixels is difficult and new geometries need to be found.
- The proposed 3-D multilayer structure in Ref [1] gives an idea of a detector array of a compact size, using a two dimensional grid in analogy with a standard CCD camera, to be efficiently coupled to single mode fibers. In addition, it helps to increase the device speed. Also, one can imagine a way of integrating the detector with the resistances through the doped substrate or metal films deposited on top of NbN film.

Reference

- [1] A. M. Smith, "A Multi-Layer Three Dimensional Superconducting Nanowire Photon Detector," *arxiv:1202.1518v1*, 2012.

Summary

Superconducting Single-Photon and Photon-Number-Resolving Detectors

In the course of this PhD thesis, I investigated the electro-optical properties of nanowire superconducting single-photon detectors (SSPDs). These detectors offer great opportunities for single-photon detection especially in the near-infrared wavelength range. In the first chapter of this thesis, three promising single-photon detection technologies are briefly introduced and a comparison is made of their characteristics to reveal the importance of performing research on these detectors. The working principle of SSPDs and its detection mechanism are also summarized and the goal of the thesis is presented.

In the second chapter, the experimental setup and the equipment used to characterize the superconducting nanowire detectors during this research are introduced. In addition, the simulation technique used to model the response of SSPDs is described. It is based on the numerical solution of a 1D heat equation coupled to the electrical equation governing the device, using iterative methods in Matlab. The required coefficients involved in the model are either acquired from the literature or extracted from the DC characteristics of the fabricated devices. This model provides a useful insight into the high-frequency dynamics of the device response after each photon detection event.

While the detection mechanism in SSPDs provides a high speed, low noise response, the small optical absorption in NbN meander with a thickness of only a few nanometers puts a limit on the maximum quantum efficiency (QE) achievable with the detector. A possible approach to overcome this problem is to couple the detector resonantly to a cavity to enhance the optical absorption in the wires. In chapter 3, the integration of the SSPDs with an optical (half)-cavity based on GaAs/AlAs Bragg mirror is demonstrated with an enhancement in the efficiency of more than a factor of two in the fabricated device.

The standard SSPD structure, like most other single-photon detectors, has a digital response incapable of determining the number of photons involved in the detection process. The ability to resolve the simultaneous number of photons that impinge on the detector in an optical pulse is highly valuable for diverse

applications. The parallel nanowire detector (PND), a previously-demonstrated configuration which provides photon-number resolving (PNR) ability to SSPDs is studied in chapter 4. It uses spatial multiplexing on a sub-wavelength scale and provides a fast response proportional to the number of detected photons..An analysis of the device dynamics is provided through the electrothermal model to investigate the limitations of this structure. These are mainly related to the current redistribution in the wires after photon detection, which limits the bias current in a PND especially with large number of parallel elements.

In chapter 5, a dual detector structure based on the series connection of superconducting nanowires, called Series Nanowire Detector (SND) is demonstrated. In SNDs the current redistribution does not cause spurious switching of a wire or false counts. This allows reliable detection of many photons at the same time, at a high bias current. The simulations presented in this chapter show that especially in combination with a large bandwidth, large input impedance load, the series structure can provide short response time with a high signal to noise ratio and promises fast PNRs with large dynamic range and high QE. Later in this chapter a proof-of-principle SND with four series sections is demonstrated as the first prototype of this detector structure with the ability to register up to 4-photon detection events in the telecommunication wavelength window.

Finally in chapter 6 the results achieved within this PhD thesis and an outline of the future work are summarized.

Acknowledgements

The completion of this research project would not have been possible without the contributions of many people to whom I am very grateful. I specifically wish to acknowledge the followings:

First and foremost, I wish to thank my promoter and daily supervisor, Prof. Andrea Fiore, for his trust in me, his keen insight and consistent guidance in this study. I greatly appreciate his availability and constructive comments during the writing of the thesis and the related research articles.

I would like to express my gratitude to the committee members: Prof. Gregory Goltsman, Prof. Harm Dorren, Prof. Jaime Gomez-Rivas, Dr. Martin van Exter and Dr. Rob van der Heijden, for kindly accepting to evaluate my thesis and providing valuable feedback.

I also appreciate the academic staff of the PSN group for their inspiration: Prof. Paul Koenraad, Prof. Erik Bakkers, Dr. Andrei Silov, and especially Dr. Jos Haverkort for providing us the opportunity to use the Ti-Sapphire laser and Prof. Richard Nötzel for the growth of the DBR structures.

I would like to thank my first mentors, Dr. David Bitauld and Dr. Francesco Marsili, for sharing their extensive knowledge and experience with me within the first few months of my PhD project and for all their support afterwards. I am also very much grateful to our collaborators at CNR institute of Rome, Dr. Roberto Leoni, Dr. Francesco Mattioli and Dr. Alessandro Gaggero for their dedicated efforts in fabricating the devices throughout this project.

I would like to thank the helpful technicians of PSN: Jos van Ruijven, Martine van Vlokhoven, Rian Hamhuis, Rene van Veldhoven, Frank van Otten and especially Peter Nouwens for his help and advice with the wire-bonding machine. I am also thankful to Jos Bremmers and Nando Harmsen for providing the liquid Helium.

I greatly appreciate the former PSN secretaries, Margriet van Doorne and Annebee Langenhuizen, for their caring attitude towards PSNers and organizing all the fun activities, especially the presence of “PSN Girls United” in the department jubilee soccer tournament in 2010! I thank them, as well as the new PSN secretaries Therese-Anne and Simone, for all their administrative assistance.

I have enjoyed the pleasant atmosphere in the PSN group owing to its nice (past and present) members: Laurent, Nicolas, Nut, Junji, Ekber, Cem, Murat, Mehmet, Matthias, Salman, Bowen, Alex, Ineke, Joris, Adam, Steven, Erwin, Samuel, Tilman, Joost, Juanita, Thuy, Yingchao, Jia, Simone, Diana, Ikaros, Anthony, Sebastian, Ilaria, Milo and many more. I enjoyed the time with my colleagues in the single-photon source sub-group: Thang, Leonardo, Francesco, Tian, Sartoon, Robert, Chaoyuan and YongJin. I specifically thank Thang for his help with the reflectivity measurements and Leonardo for his help with Mathematica. And I am very thankful to my supportive colleagues in the single-photon detector sub-group with whom I shared the passion for SSPDs: Döndü, Arjan, Giulia, Zili, and Rosalinda. I wish them all success and best of luck for the rest of their projects and careers. I specially thank Döndü for NbN film growth and Giulia for her help with the cryocooler operation.

During the last 4 years, living abroad became an easier experience thanks to the company of many nice Iranian friends. I am very appreciative to them for all their care and support.

I find no words to thank my family for their love and support. Especially my parents and my husband Saeed to whom I carry a great debt forever. I dedicate this thesis to them.

List of publications

Journal publications:

S. Jahanmirinejad, G. Frucci, F. Mattioli, D. Sahin, A. Gaggero, R. Leoni, and A. Fiore, “Photon-number resolving detector based on a series array of superconducting nanowires,” *Applied Physics Letters*, vol. 101, 072602, 2012.

S. Jahanmirinejad, and A. Fiore, “Proposal for a superconducting photon number resolving detector with large dynamic range,” *Optics Express*, vol. 20, 5, 2012.

J. P. Sprengers, A. Gaggero, D. Sahin, S. Jahanmirinejad, G. Frucci, F. Mattioli, R. Leoni, J. Beetz, M. Lermer, M. Kamp, S. Hofling, R. Sanjines and A. Fiore, “Waveguide superconducting single-photon detectors for integrated quantum photonic circuits,” *Applied Physics Letters*, 99, 181110, 2011.

A. Gaggero, S. Jahanmirinejad, F. Marsili, F. Mattioli, R. Leoni, D. Bitauld, D. Sahin, G. J. Hamhuis, R. Nötzel, R. Sanjines, and A. Fiore, “Nanowire superconducting single-photon detectors on GaAs for integrated quantum photonic applications,” *Applied Physics Letters*, 97, 151108, 2010.

D. Bitauld, F. Marsili, A. Gaggero, F. Mattioli, R. Leoni, S. Jahanmirinejad, F. Levy and A. Fiore, “Nanoscale optical detector with single-photon and multiphoton sensitivity,” *Nano Letters*, 10 (8), 2977–2981, 2010.

F. Marsili, D. Bitauld, A. Gaggero, S. Jahanmirinejad, R. Leoni, F. Mattioli, A. Fiore. “Physics and application of photon number resolving detectors based on superconducting parallel nanowires,” *New Journal of Physics*, 11, 045022, 2009.

Major conference contributions:

S. Jahanmirinejad, and A. Fiore, “Towards linear optical detection with single photon sensitivity at telecom wavelengths,” Best student paper award, in *Proceedings of SPIE*, 84400N, 2012.

S. Jahanmirinejad, G. Frucci, F. Mattioli, D. Sahin, A. Gaggero, R. Leoni, and A. Fiore, “Telecom-wavelength photon number resolving detectors based on the series array of superconducting nanowires,” in *Proceedings of CLEO Postdeadline Session*, 2012.

S. Jahanmirinejad, A. Gaggero, D. Bitauld, F. Marsili, D. Sahin, F. Mattioli, R. Leoni, G. H. Hamhuis, R. Nötzel, R. Sanjines, and A. Fiore, “Cavity-enhanced superconducting single-photon detectors on GaAs substrate,” in *Proceedings of Annual Symposium of the IEEE Photonics Benelux Chapter*, pp. 29–32, 2010.

Curriculum vitae

Saeedeh Jahanmirinejad was born in Shiraz, Iran on May 19th, 1983. In 2001, she finished Farzanegan high school, a branch of national organization for developing exceptional talents in Shiraz, Iran. She completed her BSc studies in Electrical Engineering at Shiraz University, Shiraz, Iran, in 2005, where she was awarded the scholarship to pursue her studies towards the MSc degree. She received her Msc degree in 2007 and her MSc thesis was on the theoretical investigation of avalanche photodiodes considering the effect of dead space. From 2008 to 2012 she has been working towards the PhD degree in the Photonics and Semiconductor Nanophysics (PSN) group in the department of Applied Physics at Eindhoven University of Technology, Eindhoven, The Netherlands. She was involved in the research on superconducting single-photon and photon-number resolving detectors, the results of which are presented in this dissertation. In 2012, she got a certificate of excellence for the best student paper award in the quantum optics field of SPIE Photonics Europe conference for her contribution entitled "Towards linear optical detection with single photon sensitivity at telecom wavelengths".

